# THEORETICAL AND NUMERICAL METHODS FOR PREDICTING SHIP-WAVE IMPACT GENERATED SEA SPRAY

by

**© Md. Shafiul Azam Mintu, M.Eng., P.Eng.**

A dissertation submitted to the School of Graduate Studies

in partial fulfillment of the requirements for the degree of

**Doctor of Philosophy**

Department of Ocean and Naval Architectural Engineering

Faculty of Engineering & Applied Science

Memorial University of Newfoundland

St. John's, NL, Canada

**May 2021**

# Abstract

Spray generated by ships traveling in cold oceans often leads to topside ice accretion, which can be dangerous to vessels. To develop a full methodology of goal based design for ice accretion there are two critical knowledge gaps, both of which are complex to close, and require new methods and techniques. One is a comparison of ice accretion rates for different structures in the same icing conditions. The second knowledge gap is validation data that compares predicted ice growth rates for all types of ship and offshore structures against observed values.

Estimation of the spray flux is a first step in predicting icing accumulation. The amount of spray water, the duration of exposure to the spray, and the frequency at which the spray is generated are all important parameters in estimating the spray flux. Most existing spray flux formulae are based on field observations from small fishing vessels. They consider meteorological and oceanographic parameters but neglect the vessel behavior. Ship heave and pitch motions, together with ship speed and heading relative to the waves, determine the frequency of spray events. Thus the existing formulae are not generally applicable to different sizes and types of vessels. The current study develops simple methods to quantify spray properties in terms that can be applied to vessels of any size or type, which consequently addresses the first knowledge gap. Formulae to estimate water content and spray duration are derived based on principles of energy conservation and dimensional analysis.

To estimate spray frequency considering ship motions, a theoretical model is proposed. The model inputs are restricted to ship's principal particulars, operating conditions, and environmental conditions. Wave-induced motions are estimated using semi-empirical analytical

expressions. A novel spray threshold is developed to separate deck wetness frequency from spray frequency. Spray flux estimates are validated against full-scale field measurements available in the open literature and reasonable agreement was obtained.

The complex interaction between the structure and a multi-phase fluid, including spray are not fully understood. Limitations of field measurements and model experiments encourage the use of numerical simulation to understand the formation of such spray. In this study, full-scale simulation models of wave-generated sea spray are also developed by implementing a smooth particle hydrodynamics (SPH) method. A three-dimensional (3D) numerical wave tank equipped with a flap-type wave maker and a wave absorber is created to produce regular waves of various heights and steepness. A full-scale medium-size fishing vessel (MFV) is modeled to impact waves in head sea conditions at various forward speeds. Moving ship dynamics with three degree-of-freedom (3-DOF) in waves are resolved instead of mimicking a relative ship speed. The resultant spray water amount is measured using a numerical collection box and compared against field measurements and the theoretical model, where a reasonable agreement is found. The model is able to distinguish between green water and spray water. A multi-phase two-dimensional (2D) simulation is also performed that demonstrates the role of wind in the fragmentation of water sheets into droplets and their distributions over the deck. The simulation results indicate energy released from a surging ship significantly contributes to the generation of spray.

An investigation was also performed to explore means to speed up the computationally intensive SPH simulations. A comparison with a traditional CPU (central processing unit) clusters with GPU (graphics processing unit) was performed where GPUs demonstrated faster executions. All the SPH simulations were run on GPUs.

The main contributions of this study are as follows:

- The study proposes a novel theoretical model to estimate spray water amount, spray frequency, and duration of spray events due to a ship impacting waves.
- The study develops a foundation for the SPH simulation of ship-wave collision-generated sea spray.
- The multi-phase simulation of droplet distributions enables new ways to improve theoretical models for spray droplet trajectories.

## General Summary

Shipping in cold climates is subject to ice accretion on decks and railings which can capsize the vessel in extreme conditions. Capsize in a remote area has a large financial and regulatory impact as well as subsequent environmental damage to the ice-prone areas. Accurate estimation of loads due to ice accretion is thus necessary. Most of the ice accretions occur due to the ship-wave impact generated spray that freezes in cold climates. The study proposes a scalable theoretical model to estimate the amount of spray water that can be applied to different sizes and types of vessels. Computer simulations based on mathematical solutions are also developed to reproduce the spray generated by a real size fishing boat colliding with various incoming waves in three dimensions. Both the theoretical and computer simulations are validated against the available field measurements and a reasonable agreement is found.

# Acknowledgments

Everything in life happens for a reason. My pursuit of a Ph.D. was unanticipated. I am indebted to my Ph.D. supervisor Dr. David Molyneux for not only guiding me throughout this journey but also offering me the opportunity when I needed it most. My deepest gratitude to him for allowing me to change my research area a couple of times until I discovered the current topic. I am very grateful to my co-supervisor Dr. Bruce Colbourne for his valuable advice and recommendations, and for generously giving me time even after his retirement.

The DualSPHysics (DSPH) user community was amazingly helpful during the early stage of my study. Email conversations with the DSPH code developers, Dr. Benedict Rogers, Dr. Athanasios Mokos, and especially Dr. Alejandro Crespo helped me a lot in understanding the SPH method and debugging the DSPH code.

A very special thanks to Dr. Vandad Talimi for arranging office space and GPU access for me at the C-Core building. It made my transition from professional life to graduate life comfortable. My cubicle next to a giant glass window with a clear sky view inspired me to think about so many creative (!) ideas. The works in this thesis and my startup Zol Dynamics Inc. are the proof! Sincere thanks to my fellow graduate students and researchers at C-Core for their numerous interesting conversations and exchange of ideas.

I would like to greatly acknowledge the support from the funding agencies. The project was mostly funded by ABS Harsh Environment Technology Center and MITACS (#IT13641) and partly by MITACS and Zol Dynamics Inc. (#IT10421).

While I enjoyed every bit of this adventurous journey, the final stage of my Ph.D. suddenly turned into turmoil. Failing to secure projects for my startup in a pandemic and social isolation in the lockdown made it harder to focus on the research. My two little daughters, Niha and Zoha, appeared as an angel of healing. Spending time with them was very relaxing. I am indebted to my caring mom and visionary dad for their patience and understandings throughout my studies. I turned out to be the first Ph.D. in our fourteen generations!

# Table of Contents

# List of Figures

# List of Tables

## List of Publications

**Published papers:**

1. Mintu, S., Molyneux, D., Oldford, D. (2016). "A State-of-the-art Review of Research on Ice Accretion Measurements and Modelling." Arctic Technology Conference. St. John's, NL, Canada. https://doi.org/doi:10.4043/27422-MS
2. Mintu, S. A, & Molyneux, D. (2018) "Application of GPGPU to Accelerate CFD Simulation." Proceedings of the ASME 2018 37th International Conference on Ocean, Offshore and Arctic Engineering. Volume 2: CFD and FSI. Madrid, Spain. June 17–22, 2018. V002T08A001. ASME. https://doi-org.qe2a-proxy.mun.ca/10.1115/OMAE2018-77649
3. Mintu, S. A, Molyneux, D, & Colbourne, B. (2019) "Multi-Phase Simulation of Droplet Trajectories of Wave-Impact Sea Spray Over a Vessel." Proceedings of the ASME 2019 38th International Conference on Ocean, Offshore and Arctic Engineering. Volume 2: CFD and FSI. Glasgow, Scotland, UK. June 9–14, 2019. V002T08A012. ASME. https://doi-org.qe2a-proxy.mun.ca/10.1115/OMAE2019-95799
4. Mintu, S. A, Molyneux, D, & Colbourne, B. (2020) "Ship-Wave Impact Generated Sea Spray: Part 1 — Formulating Liquid Water Content and Spray Cloud Duration." Proceedings of the ASME 2020 39th International Conference on Ocean, Offshore and Arctic Engineering. Volume 6A: Ocean Engineering. Virtual, Online. August 3–7, 2020. V06AT06A008. ASME. https://doi-org.qe2a-proxy.mun.ca/10.1115/OMAE2020-18223
5. Mintu, S. A, Molyneux, D, & Colbourne, B. (2020) "Ship-Wave Impact Generated Sea Spray: Part 2 — Formulating Spray Frequency." Proceedings of the ASME 2020 39th International Conference on Ocean, Offshore and Arctic Engineering. Volume 6A: Ocean Engineering.

Virtual, Online. August 3–7, 2020. V06AT06A009. ASME. https://doi-org.qe2a-proxy.mun.ca/10.1115/OMAE2020-18224

6. Mintu, S., Molyneux, D., and Colbourne, B. (2021). "A Theoretical Model for Ship–Wave Impact Generated Sea Spray." ASME Journal of Offshore Mechanics and Arctic Engineering, August 2021; 143(4): 041201. https://doi.org/10.1115/1.4049122

**Papers under review:**

7. Mintu, S., Molyneux, D., and Colbourne, B. (2021). "Full-Scale SPH Simulations of Ship-Wave Impact Generated Sea Spray." Submitted to Journal of Ocean Engineering.
8. Mintu, S., Molyneux, D., and Colbourne, B. (2021). "Multi-Phase Simulation of Sea Spray Droplet Distributions Over A Vessel." Submitted to Journal of Ship Technology Research.
9. Mintu, S. and Molyneux, D. (2021). " Ice Accretion for Ships and Offshore Structures. Part 1 - State of the art Review." Submitted to Journal of Ocean Engineering.
10. Mintu, S. and Molyneux, D. (2021). "Ice Accretion for Ships and Offshore Structures. Part 2 – Compilation of Data." Submitted to Journal of Ocean Engineering.

# List of Symbols and Abbreviations

## Abbreviations

| | |
|---|---|
| 2D | Two-dimensional |
| 3D | Three-dimensional |
| AMR | Adaptive mesh refinement |
| BC | Boundary condition |
| CFD | Computational fluid dynamics |
| CFL | Courant–Friedrichs–Lewy condition |
| CPU | Central processing unit |
| DBC | Dynamic boundary condition |
| DEM | Discrete element method |
| DNS | Direct numerical simulation |
| DOF | Degree-of-freedom |
| DPM | Discrete phase model |
| GPGPU | General Purpose Computing on Graphical Processing Units |
| HPC | High-performance computing |
| IACS | International Association of Classification Societies |
| IMO | International maritime organization |
| ISO | International Organization for Standardization |
| ITTC | International towing tank conference |
| LES | Large eddy simulation |
| LWC | Liquid water content |
| MFV | Medium-size fishing vessel |

| | |
|---|---|
| ML | Machine learning |
| NL | Neighbor list creation |
| PI | Particle interaction |
| RANS | Reynolds-averaged Navier Stokes |
| RMRS | Russian Maritime Register of Shipping |
| SPH | Smooth particle hydrodynamic |
| SU | System update |
| VOF | Volume of fluid |

**Symbols**

| | |
|---|---|
| $B$ | Beam of the vessel (m) |
| $B_e$ | Effective beam of the vessel (m) |
| $C_b$ | Block coefficient of ship hull (-) |
| $C_f$ | Bow flare coefficient (-) |
| $C_s$ | Spray constant ($s^2m^{-5}$) |
| $D$ | Water depth (m) |
| $dp$ | Particle resolution (m) |
| $E$ | Collection or collision efficiency of the droplets (-) |
| $E_T$ | Total energy released during ship-wave collision (kg $m^2/s^2$) |
| $E_\xi$ | Total wave energy (kg $m^2/s^2$) |
| $F_b$ | Freeboard at the still water line (m) |
| $F_{br}$ | Relative freeboard (m) |
| $Fr$ | Froude number (-) |
| $H_S$ | Significant wave height (m) |

| | |
|---|---|
| $k$ | Wave number ($m^{-1}$) |
| $k_e$ | Effective wavenumber ($m^{-1}$) |
| $L$ | Length of the vessel (m) |
| $L_{BP}$ | Ship's length between perpendiculars (m) |
| $l_{wc}$ | Liquid water content of the spray ($kg/m^3$) |
| $m$ | Mass of the ship (kg) |
| $m_a$ | Added mass of the ship (kg) |
| $m_{0s}$ | Response spectrum of relative motion ($m^2$) |
| $m_{2s}$ | Response spectrum of relative velocity ($m^2/s^2$) |
| $N_s$ | Spray frequency ($s^{-1}$) |
| $P_{spray}$ | Probability of spray (-) |
| $S_c$ | Smith correction factor (-) |
| $S_{spray}$ | Standard deviation of the combined velocity (m/s) |
| $T$ | Draft of the vessel (m) |
| $T_{sw}$ | Period between successive ship-wave encounters (s) |
| $t_{dur}$ | Duration of the spray event (s) |
| $V_a$ | Wind speed (m/s) |
| $V_d$ | Droplet velocity (m/s) |
| $V_{jet}$ | Ejection velocity of the jet due to wave impact (m/s) |
| $V_{rw}$ | Relative vertical bow velocity (m/s) |
| $V_s$ | Ship speed (m/s) |
| $V_{spray}$ | Threshold velocity for the spray (m/s) |
| $V_{sw}$ | Ship speed relative to the incoming wave celerity (m/s) |
| $V_w$ | Wave velocity (m/s) |

| | |
|---|---|
| $V_{wr}$ | Wind speed relative to the ship speed (m/s) |
| $\alpha, \gamma$ | Stem angle of ship hull (deg) |
| $\beta$ | Ship's heading angle relative to wave (deg) |
| $\rho$ | Density of water (kg/m$^3$) |
| $g$ | Gravitational constant (m/s$^2$) |
| $\lambda$ | Wavelength (m) |
| $\Delta$ | Mass of the vessel (kg) |
| $\omega$ | Wave frequency (rad/s) |
| $\overline{\omega}$ | Frequency of encounter (rad/s) |
| $\xi$ | Amplitude of the wave (m) |
| $\nu_0$ | Kinematic viscosity of water (m$^2$s) |
| $\sigma$ | Surface tension of the water (N/m) |

# Declarations of Authorship

This thesis is based on works previously published/submitted in three journal papers with first author Shafiul A. Mintu and co-authored by the supervisory committee members. The lists of corresponding papers are as follows:

1. Mintu, S., Molyneux, D., Colbourne, B. (2021). "A Theoretical Model for Ship–Wave Impact Generated Sea Spray". Journal of Offshore Mechanics and Arctic Engineering. 143. https://doi.org/10.1115/1.4049122

2. Mintu, S., Molyneux, D., and Colbourne, B. (2021). "Full-Scale SPH Simulations of Ship-Wave Impact Generated Sea Spray." Submitted to Journal of Ocean Engineering.
3. Mintu, S., Molyneux, D., and Colbourne, B. (2021). "Multi-Phase Simulation of Sea Spray Droplet Distributions Over A Vessel." Submitted to Journal of Ship Technology Research.

The work contained in the three papers was entirely developed by Shafiul A. Mintu including the development of the theoretical method and the numerical model.

The published and submitted manuscripts were prepared as drafts by Shafiul A. Mintu and editorial and technical commentary were provided by the members of the supervisory committee.

In this thesis, the text has been combined and edited for reader's convenience and to eliminate duplications in common elements of the submitted and published papers.

# Chapter 1 :

# Introduction

## 1.1 Introduction

Vessels and offshore structures operating in cold climates are subject to ice accretion on the superstructure. The accumulation of ice on the deck, the deck house tops, and other places of the ship can result in raising the center of gravity of the vessel which increases the rolling moment (Ryerson, 2013) and thus compromises the stability. The ice distribution is usually asymmetric which can cause the ship to trim and list significantly and become statically unstable (Chung 1995) (see Figure 1-1). In extreme cases, this creates the potential to capsize the vessel (Kubat, Timco 2005). The catastrophic capsize of smaller vessels is still taking place (Sumwalt et al., 2018), with the subsequent loss of life (Arctic Operations Handbook, 2013). The superstructure icing can also lead to operational hazards by creating slippery decks, ladders, and handrails. Icing can also occur on helicopter decks, deck cargo, winches, and other equipment. Ice on antennas can cut communications and distort radar signals for navigation (Arctic Operations Handbook 2013). Figure 1-2 shows an example of the severity of such marine icing.

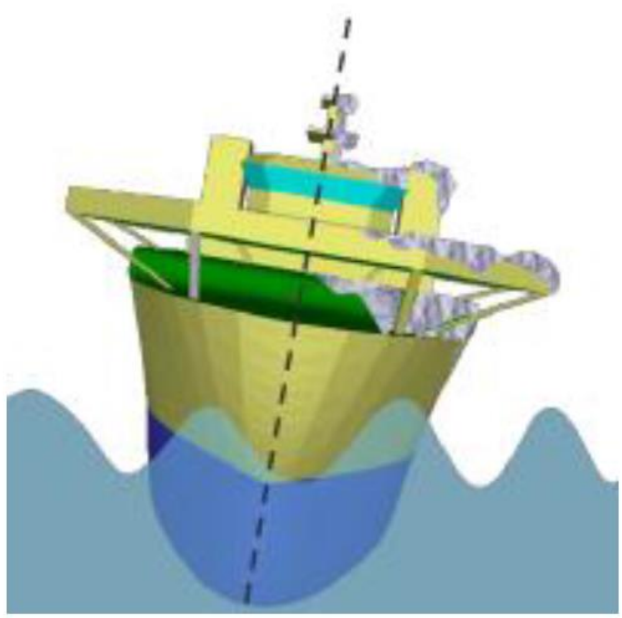

**FIGURE 1-1: SHIP STABILITY IN ICING EVENT (ARCTIC OPERATIONS HANDBOOK 2013)**

**FIGURE 1-2: ICE ACCRETION ON THE CANADIAN COAST GUARD SHIP "SIR WILLIAM ALEXANDER" (KUBAT, TIMCO 2005)**

To ensure safe marine operations, international codes and standards require ice-going ships to have adequate intact stability, by considering a prescribed level of icing on exposed areas of the topside structures. In most cases, regulatory bodies use empirical formulae, based on statistical analysis to estimate the amount of icing. Also, the empirical formulae cannot be applied to any sizes and types of vessels (Lebiedzlnski and Thomas, 1993; Ryerson, 2013; Thomas, 1991) and, there is little agreement among the codes provided by the regulatory bodies.

In order to ensure the safe operation of ships in cold climates, a better understanding of the icing phenomenon is required. The prediction of marine icing is a very complex subject and it depends on a plethora of variables: the wind, its direction with reference to the ship, air temperature, and the sea temperature. The ship's form also plays an important part (Sapone 1990). The amount of spray, its density, duration, and frequency depend on the ship design features, speed, and heading with respect to the waves (Shipilova et al. 2012).

The study of icing can be traced back to the 18th century. Despite many years of observations, and the development of empirical and analytical models, marine icing remains a serious operational issue for small and large vessels (Arctic Operations Handbook 2013). To improve the safe operation of ships in cold climates, a better understanding of the icing phenomenon is required. In this work, we seek to fill this gap.

## 1.2 Research Objectives

The following objectives have been identified based on the literature review:

1. To develop a scalable model for ship-wave impact generated sea spray that can be used to estimate ice accretion on ships of any size operating in cold climates.
2. To develop a numerical model for spray generation to overcome the limitations of model scale experiments and field measurements in understanding spray generation physics.

## 1.3 Thesis Outline

The thesis has six chapters. Chapter 1 (this chapter) introduces readers to the topic in simple words and outlines the objectives of the research. Chapter 2 explains the physics of ice accretion. Chapter 2 gives a thorough review of the literature and identifies knowledge gaps. Chapter 4 describes the development of the theoretical model and Chapter 5 presents the development of numerical spray production. The final section of the thesis describes the summary of the findings and concludes with some recommendations for future work in Chapter 6.

# Chapter 2 :

# Physics of Ice Accretion

## 2.1 Introduction

There are two main sources of ice accretion on ships and offshore structures, sea spray and atmospheric precipitation. Wave-impact spray is the dominant source of marine icing (Zakrzewski, 1986a; Zakrzewski et al., 1988) and contributes to between 50% and 90% of the icing on ships (Lozowski, 2017). The remaining amount comes from natural sources (atmospheric sources), depending on the geographic locations (Arctic Operations Handbook, 2013). Different stages of the formation of ice accretion are discussed in this chapter.

## 2.2 Formation of Sea Spray

### 2.2.1 Natural Sea Spray

Natural sea spray or wind-generated spray is a relatively small source of marine icing, but it is a constant water flux that is created within the airflow in windy conditions (Dehghani et al., 2016a). When the wind blows over a calm sea surface for a certain period, it creates disturbances on the water surface and generates waves. Sea spray droplets are generally produced due to phenomena related to sea surface wave breaking (Veron, 2015). When waves break, a significant amount of air can entrain in the form of bubbles. The bursting of these bubbles produces two different types of droplets. One is "film droplets" generated by the shattering of the surface film of the bubble, and the other is "jet droplets" generated by the bubble cavity collapse resulting in a jet of droplets (Veron, 2015).

Wind-generated waves breaking at wind speeds higher than 4 m/s produce sea-spray droplets with sizes from ≤1 μm to ≥25 μm (Fuentes et al., 2010). However, according to Horjen and Vefsnmo (1985), and Andreas (1990), the lift of water droplets into the air occurs when the wind speed exceeds 9 m/s. Jones and Andreas (2012) estimate that spray begins to form at wind speeds of about 37 knots (19 m/s), and the drops created at lower wind speeds contribute little to the icing of stationary offshore structures, such as oil drilling platforms. They also found that the larger spume drops contributed to higher icing rates on stationary platforms (Ryerson, 2013).

At the crests of breaking waves, elongated globule/filaments eject and elongate by wind action (Veron et al., 2012). These are called liquid sheets (Veron, 2015). These water sheets subsequently fractionate rapidly into numerous daughter droplets under the continued action of the wind leading to the third type of droplets generated, called "spume droplets" (Veron, 2015; Zakrzewski, 1986a). A minimum wind speed of 7 to 11 m/s is required to create spume droplets (Andreas, 1990; Horjen and Vefsnmo, 1985). Another form of droplets, called "splash droplets", can be generated by a plunging wave impinging on the sea surface. Since they have a different formation mechanism, they are distinguished from spume droplets although they have the same characteristic size as spume droplets (Veron, 2015). These types of spray generation processes can be called "natural spray" since they are forming independently of any other process. The range of natural spray droplet size spans at least six orders of magnitude, from radii of a few nanometers to several millimeters. Table 2-1 summarizes the property of these droplets. In a recent study, it is shown that bag-breakup (breakup of the droplet into a bag-shaped liquid) is the dominant mechanism of natural spray generation (Troitskaya et al., 2017).

Film droplets can suspend in the atmosphere (also called atmospheric droplets) for days to weeks because of their extremely light weight. They contribute to the global aerosol and act as nucleation sites for clouds and fog and are responsible for precipitation (cloud, fog, etc.) which causes atmospheric icing (Veron, 2015). They have the highest ejection velocity of 30 m/s (Veron, 2015). In the Arctic, 50% of icing occurs due to this atmospheric source (Arctic Operations Handbook, 2013).

TABLE 2-1: TYPES OF SPRAY DROPLETS

| | **Film Droplet** | **Jet Droplet** | **Spume Droplet** |
|---|---|---|---|
| **Radius** | 0.01 to 1 µm. | 1 to 50 µm | O(40) µm to 6 mm |
| **Suspension time** | Days to weeks | Seconds to several minutes | Few seconds |
| **Max ejection height** | Eject to the atmosphere | 10–20 cm | A couple of meters (W. P. Zakrzewski, 1989) |
| **Formation mechanism** | Bubble bursting | Aftermath of the bubble bursting.<br><br>Impact of the raindrops on the sea surface | Not fully understood. Generally by tearing off of wave crest by winds. |
| **Ejection velocity** | 20 to 30 m/s | 0.3 to 8 m/s | Assumed to be equivalent to wind speed at the wave crest. |

Jet, spume, and splash droplets do not contribute to marine icing since their ejection height is less than a typical freeboard of marine structures (Zakrzewski, 1986a). Such spray may affect only small ships with low freeboard and low bows in strong winds (Zakrzewski, 1986a). Film and jet droplets are well studied by meteorologists mainly due to their importance in forecasts of tropical cyclones, storms, and hurricanes. The formation process of spume droplets is, however, poorly understood (Veron, 2015), and therefore their sizes and velocity distributions are not well explained.

### 2.2.2 Wave-Impact-Generated Sea Spray

When waves impact or collide with structures such as ships, offshore platforms, or coastal structures, droplets are generated under certain conditions. The mechanism of wave-impact sea spray is not fully understood (Horjen, 2013; Kulyakhtin and Tsarau, 2014a; Lozowski et al., 2000; Shipilova et al., 2012; Zakrzewski et al., 1988). At present we can only postulate (Bodaghkhani et al., 2016) and there are two possible mechanisms identified in the literature:

1. Spray forms directly at the time of impact by splashing resulting from the ship's interaction with the wave crest due to pitch heave/motion (Jones and Andreas, 2012; Zakrzewski, 1986b).

2. Spray forms in multiple steps. First, a jet or sheet of water rises above the ocean surface along the hull of the ship as the moving bow encounters a wave. Sheet breakup then follows and can occur in two ways:

    I. The water sheet tears off under wind action, similar to the production of spume droplets (Ryerson, 2013; Zakrzewski et al., 1988).

    II. The water sheet breaks into ligaments, and ligaments further break to form droplets according to nozzle atomization physics (Dehghani et al., 2017).

Ships of different sizes and types interact with sea states differently. Smaller vessels generate spray frequently because of their greater pitch angle and pitch frequency and spray clouds often cover the entire ship. Large vessels generally spray less frequently and spray is less likely to cover the entire ship (Ryerson, 1995). It should be noted that spray of water is different from deck wetness (sometimes referred to as green water), which is the foredeck wash or submergence of the deck edge (Lewis, 1988).

The amount of spray, its liquid droplet concentration, the spray duration, and frequency depend on the ship's hull, speed, and heading with respect to the wind and waves (Arctic Operations Handbook, 2013), and the motion of the vessel. The previous studies consider only the surge motion in the spray generation models (Dehghani et al., 2018; Lozowski et al., 2000; Zakrzewski et al., 1988). A vessel on waves can have a vertical motion at the bow from combined heave and pitch motion of 1-2 times of the wave amplitude (Lewis, 1988). This relative motion will contribute to the quality of the spray cloud and also affect the elevation of the droplets. The first mechanism assumes the spray is generated by the bottom and flare entry slamming of the bow onto the incoming wave crest.

### 2.2.3 Water Sheet Breakup

The second mechanism splits the spray generation process into multiple processes. When a high-energy wave strikes a vessel, it can create a layer of water sheet as shown in Figure 2-1. The local impact velocity of the water particles, air entrapment, surrounding wind velocities, and other factors determine the ejection velocity and the thickness of this water sheet. This high-velocity water sheet cannot remain unbroken (Ryerson, 2013). How, when, and where at the ship bow the sheet breakup occurs is not yet well predicted. Two possible ways a sheet of water can break: 1) the water sheet can eject past the tip of the bow which can then shears off by the wind as shown in Figure 2-1 or 2) the water sheet goes through a few breakup processes.

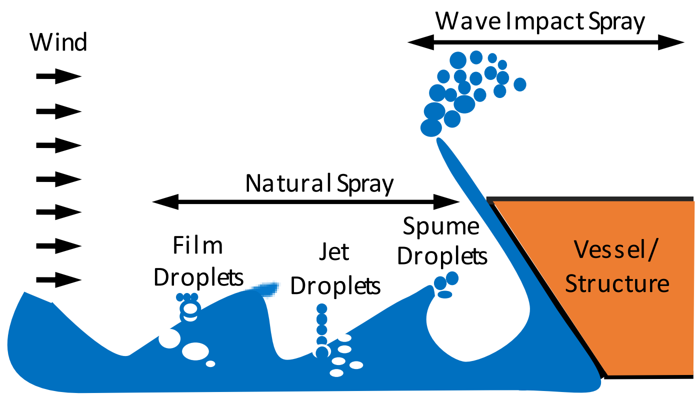


**FIGURE 2-1: SCHEMATIC OF SPRAY GENERATION PROCESS**

The later mechanism is described by Dehghani et al. (2016b, 2017). They explained ship-generated spray using the theory of nozzle atomization physics for sheet breakup, where the sheet breaks into ligaments (primary breakup) when the effects of entrained air, gravity, and the local wind field overcome the water surface tension. These ligaments go through a secondary breakup and create a droplet cloud of sea spray. In their models, they assumed the droplets originate from the tip of the vessel bow (Dehghani et al., 2018, 2017, 2016a). This and other atomization theories are based on thin sheet thickness in millimeter-scale (Clanet and Villermaux, 2002; Ren and Marshall, 2014; Yang et al., 2012; Zhao et al., 2015), where it is assumed that viscous effects are not significant in the breakup characteristics (Ren and Marshall, 2014). The threshold criteria are generally determined based on experimental data. Application of these experimentally derived criteria should be limited to the intended cases, and may not be applied in general. A ship-wave collision can produce a sheet thickness of 8.5 cm (Dehghani et al., 2017). The application of the nozzle atomization process to explain thick sheet breakup in marine spray needs careful consideration.

### 2.2.4 Droplet Generation

Unlike natural spray production, there is very little study on the initial size, concentration, and ejection velocity of droplets produced by wave-impact sea spray. The droplet diameter arising from ship-wave impact can vary from very fine, at 14 µm, to very large, at 7.7 mm (Ryerson, 1995), similar in characteristic size to jet and spume droplets according to Table 2-1. This indicates that droplets generated by wave impact may have different production mechanisms from those seen in natural spray production. These differing production mechanisms will determine the various sizes and corresponding velocities of the droplets. However, production mechanisms and corresponding droplet characteristics are yet to be discovered and classified. Table 2-1 shows smaller size droplets have larger ejection velocity and vice versa. This size-velocity dependency of droplets is also identified by Dehghani et al. (2016b). Figure 2-1 depicts the droplet generation process for both natural and wave-impact sea spray. In general, the droplets generated by both natural spray and wave-impact spray can be classified as shown in Table 2-2 and Figure 2-2.

**TABLE 2-2: CLASSIFICATION OF DROPLET SIZE**

| | **Small** | **Medium** | **Large** |
|---|---|---|---|
| **Size (radius)** | < 1 µm | 1 - 25 µm | O(40) µm to several mm |
| **Suspension time** | Days to weeks | Minutes to hours | Few seconds |
| **Maximum Velocity** | 30 m/s | 8 m/s | Unknown |
| **Spray Type** | Natural spray | | |
| | | Wave-impact spray | |

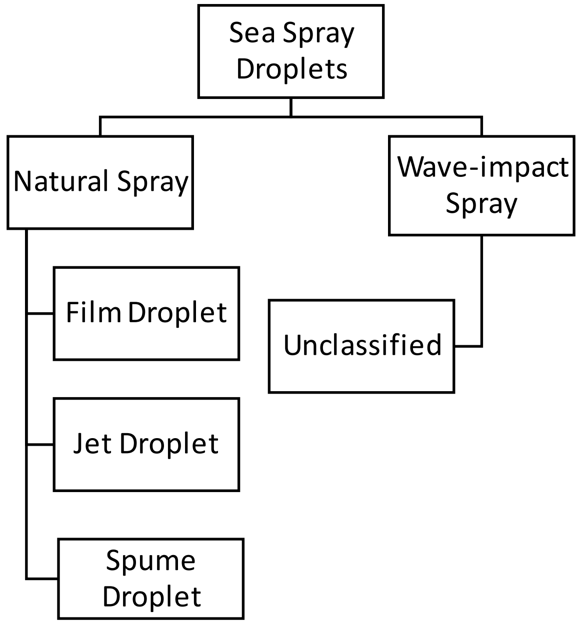


**FIGURE 2-2: TYPES OF SEA SPRAY DROPLETS**

Our understandings of the large droplet formation process, both for natural spray and wave-impact spray, is very limited (Bodaghkhani et al., 2016; Veron, 2015). The exact outcome of the droplet generation process is dependent on the surface tension, viscosity, density, and diameter of the strips (if any) undergoing breakup (Sazhin, 2014). Breaking waves dissipate up to 40% of their energy and up to 50% of the energy loss is expended in entraining air in the water bulk and creating a dense plume of bubbles (Rapp and Melville, 1990). The air layer plays an important role when a body with a very small deadrise angle (less than 3–4 degrees) is slamming into the water. The compressibility of entrapped air needs to be considered (Yang and Qiu, 2012). Sometimes a sheet of water is formed, but the breakup described above does not occur. This implies that there are more criteria involved in the breakup phenomenon (Ahmed et al., 2009).

There is no data reported on the initial ejection velocity of wave-impact spray, which is necessary to determine the trajectories of droplets (Dehghani et al., 2016a). Initial velocities of droplets are assumed to be equal to the wind velocity in past studies, irrespective of their sizes (Horjen, 2013, 2015; Kulyakhtin and Tsarau, 2014a; Shipilova et al., 2012; Zakrzewski, 1986a). (Lozowski et al., 2000) combined deepwater linear wave theory with a wave run-up condition to estimate the initial vertical and horizontal velocities of the droplets in their RIGICE code. The estimated velocities were independent of the droplet size. Uniform droplet size and mono-velocity of sea spray are simplifying assumptions and therefore are not completely accurate for predicting ice accretion (Dehghani et al., 2016a).

## 2.3 Spray Distribution

Once a water droplet is ejected from the sea water, it will interact with the airflow, exchange momentum, heat, and moisture with the surrounding air (Veron, 2015). Bigger droplets can further break up to form smaller droplets through the droplet breakup phenomenon (Dehghani et al., 2017; Veron, 2015). Droplet trajectories from the injection spots toward the marine vessel determine the rate of water droplets received on the vessel (Zakrzewski et al., 1988).

The trajectory depends on the gravity force, wind velocity, initial size and velocity of droplets, and many other parameters. Among them, droplet size distribution, droplet velocity distribution, and droplet concentration are the crucial input for droplet trajectory analysis (Dehghani et al., 2016a; Zhuang et al., 1993). Using Newton's law, the equation of motion of a single spherical droplet can be established, as described by Lozowski et al. (2000) and Zakrzewski et al. (1988). However, these analytical models cannot take into account Faxen effects (effects of flow curvature), Saffman lift (lift effects from velocity gradients in the air), and Magnus effect (effects from the rotation of the drop). Among the listed factors, droplet concentration is generally ignored in past studies by assuming the spray cloud is dilute and droplets travel over the vessel individually without affecting each other (Dehghani et al., 2016a, 2016b, 2018; Kulyakhtin and Tsarau, 2014a). Accurate spray concentration estimates would provide more reliable projections of the total spray cloud (Veron et al., 2012).

## 2.4 Freezing of Spray Water

The final stage of the icing process is the freezing of droplets on the impacted surface. Ice accretion from sea spray occurs when the air temperature is below the freezing point of sea water which is approximately -2$^0$ C (IMO, 2011) and -1.8$^0$ C for Polar Regions due to reduced salinity (Ryerson, 2013). The sea spray freezes due to four main heat fluxes at the air-water interface, which are: convection, Qc; evaporation, Qe; heat capacity of the impinging spray, Qd; and radiant heat flux, Qr (Kulyakhtin & Tsarau, 2014). Horjen (2013) considered an additional term – heating due to adiabatic compression of the air and viscous work in the air boundary layer. During the flight, the drop is cooling via evaporation, convection, and radiation, and is decreasing in size by evaporation or aerodynamic breakup unless it coalesces with another drop. When the drop strikes the structure, it splashes and runs off the surface as a film, losing heat via conductive, convective, and radiative losses (Ryerson, 2013). The heat transfer coefficient is independent of the temperature in the case of forced convection (Kays et al., 2005) but varies with the wind speed. When the airflow is obtained for certain wind conditions, the distribution of heat transfer coefficients on the structure surface can be calculated from the energy balance equation (Kulyakhtin and Tsarau, 2014b). The rate of spray freezing and subsequent ice growth is a function of water delivery rates at every location on the ship, and the rates of latent and sensible heat removal from these locations (Ryerson, 1995). The shape of the accreted ice depends on the atmospheric conditions (Szilder and Lozowski, 1995). The icing of structures often occurs under conditions where the flux of water droplets to the surface of the structure is sufficiently high that not all the water freezes and the excess water run off the surface (Makkonen, 1985).

## 2.5 Atmospheric Icing

Another source of icing is atmospheric precipitation, which includes hoar frost, freezing rain, super-cooled fog, and pellets of wet snow or ice (Lozowski, 2017). Atmospheric icing is traditionally classified according to two different formation processes, precipitation icing and in-cloud icing (Arctic Operations Handbook, 2013). Some authors (Dehghani et al., 2016b; Kulyakhtin and Tsarau, 2014a) report that atmospheric icing is not significant, which is not the case. It depends on the geographic location where the vessel or offshore structure is operating. In the Arctic, 50% of the icing occurs due to atmospheric sources (Arctic Operations Handbook, 2013). Atmospheric icing is beyond the scope of this thesis and is not discussed further. Interested readers can check Ryerson (2013), where a detailed review is presented.

# Chapter 3 :

# Literature Review

## 3.1 Introduction

This chapter presents a state-of-the-art review of existing literature related to ice accretion on vessels and offshore structures. A brief review of the international codes and standards is summarised. Existing reports for field measurements of spray and icing as well as model scale experiments to simulate the spray and ice accretion are reviewed. Various theoretical and numerical methods for spray prediction are critically reviewed. Finally, the chapter concludes by discussing some aspects of improved ice accretion prediction models that may be particularly relevant for larger vessels and offshore structures.

## 3.2 International Codes for Levels of Ice Accretion

There are some international codes and standards available that require the ice-going ships to have adequate intact stability, taking into consideration a prescribed level of icing on exposed weather decks, gangways, and projected lateral areas of the superstructure. This section reviews the up-to-date requirements for the icing allowance.

According to the IMO polar code (IMO MEPC 68/6/2, 2015), ships shall have sufficient stability in intact conditions when subject to ice accretion. An icing allowance has to be considered in the stability analysis prescribed for ships operating in areas and during periods where ice accretion is likely to occur. The allowance is 30 kg/m$^2$ on exposed weather decks and gangways and 7.5 kg/m$^2$ for the projected lateral area of each side of the ship above the water plane. These requirements are the same as those within the IMO Intact Stability Code. Tracing back through the IMO documents for the origin of these requirements, it was found that they came from SLF 54/16/1, which gives early concepts behind the rule based on requirements for fishing vessels.

The Polar Code also states that ships operating in areas prone to icing have to be designed to minimize the accretion of ice, but no guidance is given as to how this may be done.

There is a new amendment proposed for the IMO Intact Stability code (2015). The newly adopted IMO Resolution MSC. 398(95) "Amendments to Part B of the International Code on Intact Stability, 2008 (2008 IS Code)" gives a new formula for ice accretion allowance. The ice accretion weight per square meter may be calculated as per the formula, in kg/m$^2$,

$$w = 30.\frac{2.3(15.2L - 351.8)}{l_{FB}}.f_{tl}\cdot\frac{l_{bow}}{0.16L} \quad (1)$$

where $f_{tl}$ is timber and lashing factor = 1.2, L is the length of the ship in m, $l_{FB}$ is freeboard height in mm, and $l_{bow}$ is the length of bow flare region in m, to be taken as the distance from the longitudinal position at which the maximum breadth occurs on a water line located 0.5 meters below the freeboard deck at the side to the foremost point of the bow at that waterline. The ice accretion weight, w (kg/m$^2$), over the timber deck region should be applied to each of the load cases as illustrated in Figure 3-1.

A review of IMO documents revealed that the formula above was put forward in SLF 55/3/8. The formulation was intended to be guidance for ice accretion on ships carrying timber deck cargoes. SLF 55/3/8 is a submission from the United States which makes amendments to an IACS proposal SLF 55/3/1/Add.1 which includes an appendix with an early version of the ice accretion formulation.

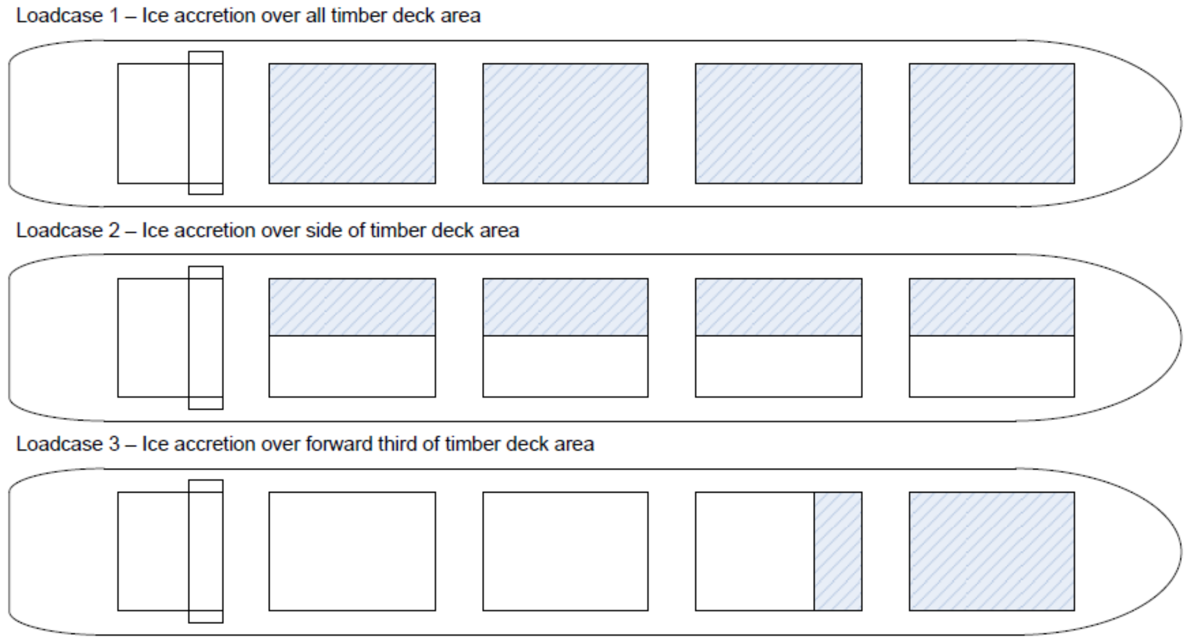


**FIGURE 3-1: ICE ACCRETION LOAD CASES FOR TIMBER DECK CARGOES (IMO RESOLUTION MSC. 398(95))**

The recent Russian Maritime Register of Shipping (RMRS) rules (RMRS, 2016) have included the new IMO Resolution MSC.398(95) for sea-going ships, and this replaces the previous version using the fixed amount of accumulated ice. RMRS Rules for MODUs and FOPs (RMRS, 2014), assume rates of ice and snow accretion are specified by the geographic location of the operation. Values range from 13.5 kg/m$^2$ to 150 kg/m$^2$. If the decks are located at a height up to 10 m above the water line, the specified mass of ice per square meter (of the total area of the horizontal projection of exposed decks) shall be assumed to be 30 kg, or 15 kg if the height is from 10 m up to 30 m. If the height of the deck is above 30 m the mass of ice may be neglected. The rules also contain guidelines for the snow load that says the mass of snow per square meter shall be 100 kg for unmanned units and 10 kg for manned units. Special facilities to reduce ice and snow mass shall be considered in the design of units, but no guidelines are given as to how it should be done.

ISO 19906 for Arctic Offshore Structures, Section A.6.3.5 (ISO, 2010) discusses various aspects of marine icing for fixed offshore structures including atmospheric and sea spray generated icing. The standard states that sea spray icing begins to occur at wind speeds between 8 m/s and 10 m/s, combined with a sea temperature of less than $8^0$ C, and an air temperature less than the freezing point of sea water. At that location, the stronger the wind, the higher the spray is lifted. While the height of sea spray icing is usually limited to 15 m to 20 m above the sea surface, there have been reports of sea spray icing up to 60 m above the sea surface (ISO, 2010). The standard identifies growth rates for ice accretion, based on air temperature and wind speed, and classifies icing by intensity as slow (<10 mm/hour), fast (between 10 and 30 mm/hour), or very fast (>30 mm/hour). ISO 19906 gives some indication of possible exposure times based on season within the Arctic, but it is relatively crude. The ISO standard also gives guidance on maximum thickness due to icing as a function of structure height, which is the same as the NORSOK standard (NORSOK, 2007). It is based on a total accumulation of ice within height bands above sea level, but no indication of the environmental factors giving rise to these icing parameters. The ISO standard states that the lack of available data requires urgent comparisons between collected data and the exchange of experiences since this will be a way to improve knowledge and data necessary for a future comprehensive international standard for atmospheric icing. Detailed information about icing frequency, intensity, etc. should be collected (Arctic Operations Handbook 2013).

In NORSOK N-003 (NORSOK, 2007) section 6.4.2, ice accretion due to sea spray and atmospheric icing are considered separately, and ice accretion thickness and density are specified for various elevations on the structure. Ice caused by sea spray is further categorized by the geographic locations and summarized in Table 3-1.

**TABLE 3-1: ICE ACCRETION LEVELS IN NORSOK N-003 (NORSOK, 2007)**

| Height above sea level [mm] | ACTION CASE 1 | | | ACTION CASE 2 | |
|---|---|---|---|---|---|
| | Ice caused by sea-spray | | | Ice caused by rain/snow | |
| | $56^0$ N to $68^0$ N [mm] | North of $68^0$ N [mm] | Density [kg/m$^3$] | Thickness [mm] | Density [kg/m$^3$] |
| 5 to 10 | 80 | 150 | 850 | 10 | 900 |
| 10 to 25 | Linear reduction from 80 to 0 | Linear reduction from 150 to 0 | Linear reduction from 850 to 500 | 10 | 900 |
| Above 25 | 0 | 0 | - | 10 | 900 |

The “Canadian Standard CSA S471” (CSA, 2004) gives only a short discussion on snow and ice accretion in Section 5.2.3, which states ice accretion from sea spray, freezing rain or drizzle, freezing fog, or cloud droplets shall be considered in the design. In the absence of specific information, the ice that can form on the structure may be assumed to have a density of 900 kg/m$^3$. As a final note, the CSA code states that a designer should obtain as much environmental data as possible for the region of operation, including data from climatic atlases, ship measurements, site measurements from rigs operating in the area, and coastal stations.

DNV-GL rules for fishing vessels (DNV-GL, 2015a) state in section 1.3.5 that allowance for ice accretion in the worst operating condition shall be covered within the stability booklet. The allowance applied is the same as IMO requirements, i.e. 30 kg/m$^2$ on exposed weather decks and gangways, 7.5 kg/m$^2$ for the projected lateral area of each side of the vessel above the water plane. In Part 6 Chapter 6 Section 3 of the rules (DNV-GL, 2015b) “Operations in Cold Climate-Winterized”, it says the icing weight distribution shall be calculated for decks, gangways, wheelhouse tops, and other horizontal surfaces, as defined in Table 3-2. It can be seen that they have introduced allowances for reduction of icing weight with height, which are also included in the RMRS and NORSOK formulations.

**TABLE 3-2: ICE ACCRETION LEVELS IN DNV-GL WINTERIZATION REQUIREMENTS (DNV-GL, 2015B)**

| | Icing load (kg/m²) | | |
|---|---|---|---|
| | from forward extremely to 50 m aft F. P. | 50 to 100 m aft of F. P. | > 100 m aft of F. P. |
| > 18 m from WL | 30 | 30 | 30 |
| > 12 to 18 m from WL | 40 | 30 | 30 |
| > 6 to 12 m from WL | 80 | 40 | 30 |
| 0 to 6 m from WL | 120 | 60 | 30 |

ABS (ABS, 2015), in general, refers to the polar code and the intact stability code for ice load estimation. Regardless of the vessel size, type, or geographic location, the guide prescribed some icing monographs developed by the United States National Oceanic and Atmospheric Administration (NOAA) from actual icing reports from fishing vessels, U.S. Coast Guard, and towing vessels operating in Alaskan waters (Overland et al., 1986). These reports were based on icing events that lasted anywhere from 1 to 26 hours but averaged 3 to 6 hours. They are based on wind velocity, air temperature, water temperature, and the freezing point of sea water. This simple-to-apply model requires a minimum amount of information and hence is attractive for regulators as a method for identifying potential for icing accumulation. Some researchers consider the model is too simple to be accurate (Makkonen et al., 1991). The NOAA National Weather Service Environmental Modeling Center provides an online forecast for ice accretion risk at: http://polar.ncep.noaa.gov/marine.meteorology/vessel.icing/. Appendix 3, Figure 2 of the code provides information for ice accretion against wind velocity for air tempe ratures ranging from –34°C (–30°F) to –7°C (+20°F) as shown in Figure 3-2.

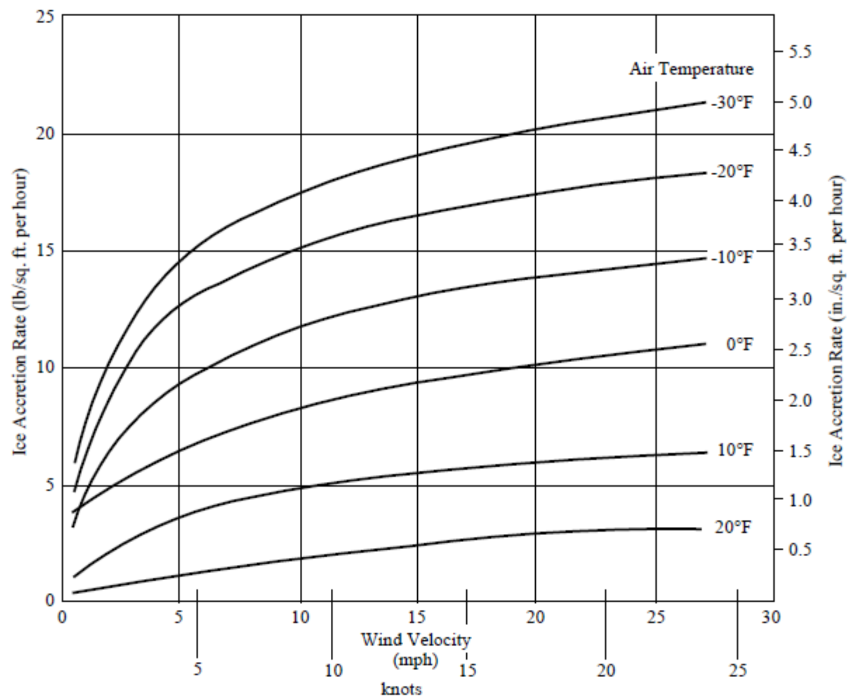


Source: U.S. Navy Cold Weather Handbook for Surface Ships, Figure 7-3, (May 1988)
Accreting Surface: Flat Panel; Water Spray Temperature: 41-48°F

**FIGURE 3-2: ICE ACCRETION VERSUS WIND VELOCITY FOR SIX AIR TEMPERATURES (ABS 2015)**

Depending on the severity of the winter, Lloyd's Register (LR, 2015) has three different requirements for ice accretion values. Section 10 "Stability due to Ice Accretion – Winterisation-S" says the effect of icing is to be considered in the stability calculations and to be complied with the IMO Code on Intact Stability Resolution MSC.267(85), as amended – Chapter 6 – Icing Considerations. The ice accretion values are to be taken as an additional mass per unit area, as given in Table 3-3. The level of winterization is given by the coldest expected temperature encountered by the ship, and its duration, with Level C as the mildest (short duration transits in low temperatures), and Level A as the most extreme (e.g. ships operating year-round in the Arctic or Antarctic).

**TABLE 3-3: ICE ACCRETION VALUES (LR 2015)**

| Winterisation Level | Horizontal deck kg/m$^2$ | Vertical side kg/m$^2$ |
|---|---|---|
| Winterisation S(C) | 30 | 7.5 |
| Winterisation S(B) | 60 | 15 |
| Winterisation S(A) | 100 | 25 |

All the rules, standards, guides, or codes give maximum allowable ice thickness (combined with ice density) or mass per unit area of the exposed structure without reference to the expected environmental conditions. The IMO Polar code applies a constant value for ice accumulation, in terms of kg/m$^2$, with a separation between horizontal and vertical surfaces. Lloyds Register has more severe requirements based on the expected level of winterization required. Other requirements are more complex, with allowances for height above the waterline (RMRS, NORSOK) or a combination of height and distance from the spray origin (DNV-GL). None of the standards or codes gives predictions for the amount of ice accretion that take into account differences in the type of structure in the same atmospheric conditions. In effect, the assumption is that the type of structure has no effect on the distribution of icing.

Figure 3-3 shows a comparison of the allowance for ice accretion given by each of the requirements reviewed, against height above the waterline. There is clearly a high degree of variation between the codes, which may reflect possible variations with type of ship or type of offshore structure used to develop the code, but there is no specific guidance on which method to use for a given ship or offshore structure.

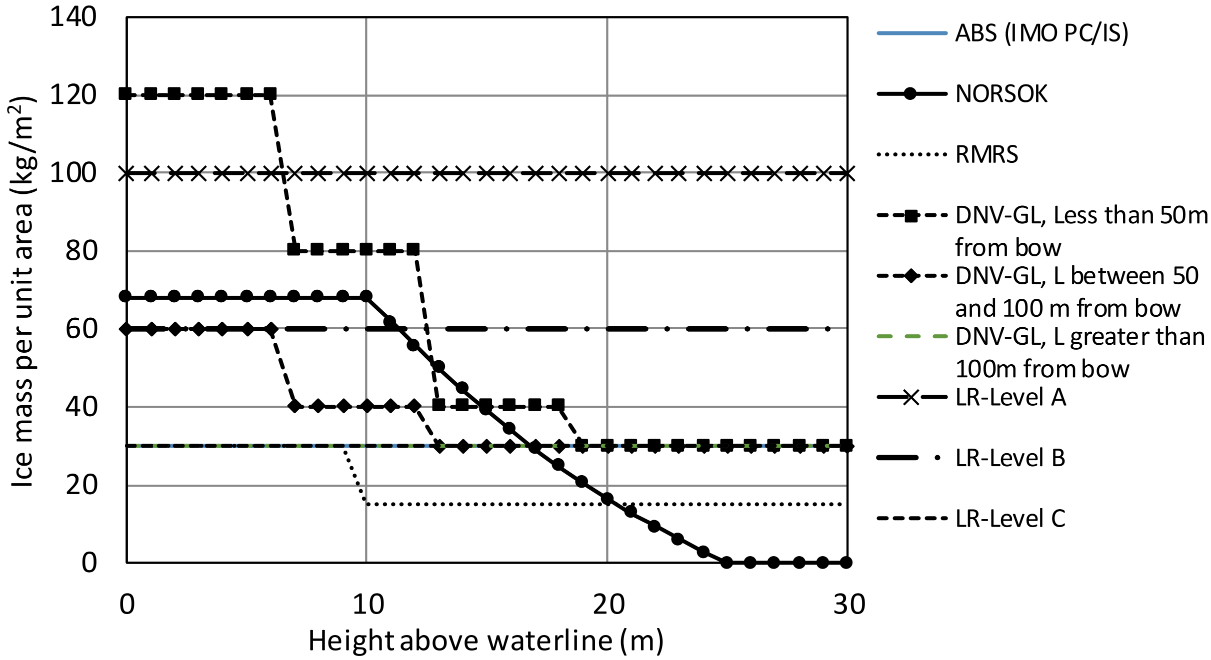


**FIGURE 3-3: ACCUMULATION OF ICE ON HORIZONTAL SURFACES AGAINST HEIGHT ABOVE THE SEA SURFACE, AS GIVEN BY DIFFERENT STANDARDS AND GUIDES.**

The codes were developed based on the limited population of ships and ship types and were focused on specific geographic regions. Moreover, the formulae rely mostly on data collected for smaller vessels, and extrapolation to the larger vessels used in oil and gas operations is questionable. Icing codes and standards suggest the requirements for the total amount of ice accumulation on the structure, and the amount is irrespective of the size or type of the vessel, and the environmental conditions within the operating area.

## 3.3 Ice Accretion Measurements

Various measurement techniques were applied in the past to estimate the amount of spray water and the resulting icing amount. Both field trial and model scale experiments were conducted which are discussed in this section.

### 3.3.1 Field Measurements

Field measurements of icing events are very challenging, costly, and sometimes dangerous. Not many researchers have collected data on actual ice accretion measurements. Some researchers investigated the wave-impact sea spray (Borisenkov and Pchelko, 1975; Horjen and Vefsnmo, 1985; Panov, 1976; Ryerson, 1995; Thomas, 1991), while others focused on the measurements of the accumulated ice and its distribution on the deck (Gagnon et al., 2009; Lozowski et al., 2000).

#### *3.3.1.1 Measurements of Full-Scale Spray*

Most of the icing observations were based on small to medium-sized fishing vessels. Limited information is available on icing observations on larger vessels (Ryerson, 1995). In the late 1980s, Zakrzewski and colleagues published several papers on the spraying of ships (Zakrzewski 1987, Zakrzewski, Lozowski & Muggeridge 1988, Zakrzewski & Lozowski 1987). (Zakrzewski 1987) developed an empirical model for collision-generated spray (ship-wave interaction) based on Russian field data for a 39 m Russian fishing boat "MFV Narva" (Borisenkov and Pchelko, 1975) in the Sea of Japan in February 1973. During these trials, a cylinder was placed on the main deck of the ship at the ship's foremast and water was collected from a single splash of the spray. Spray generated from the wave crest due to ship roll/pitch motion was neglected. The data set was not published.

The data were retrieved and compiled by Zakrzewski (1986b, 1986a) from a soviet icing database and expressed in an empirical formula. This formula was used for validation by many researchers as benchmark data for spray generation due to their completeness (Dehghani et al., 2016a; Kulyakhtin and Tsarau, 2014a; Lozowski et al., 2000; Samuelsen et al., 2017; Shipilova et al., 2012). Horjen et al. (1986) reported another spray experiment on a whaling vessel Endre Dyrøy in Norwegian, which was later translated by Samuelsen et al. (2017). The spray was collected by a circular pipe-bend collector with a diameter of 0.1 m at the heights of $z1 = 6.6m$, $z2 = 7.5m$, $z3 = 9.1m$, and $z4 = 10.9$ m.

The frequency of slashing was also measured on an MFV by Panov (1976) and given in Table 3-4, but there are no published data sets on the amount of spray water (Zakrzewski, 1986a). Panov (1976) reported that the MFV operating in a 6 m wave, 125° heading at 6 knots produced approximately 1 to 1.1 $m^3$ of water to the entire MFV per minute for the bow height equal to 3.7 m (Zakrzewski, 1986a).

**TABLE 3-4: SPRAY FREQUENCY DATA OF (PANOV, 1976)**

| Wavelength | Spray Frequency [No/min] | | | | | | | |
|---|---|---|---|---|---|---|---|---|
| λ =10 m | 14.86 | 11.88 | 13.69 | 15.74 | 12.30 | 12.87 | 14.46 | 13.87 |
| λ =20 m | 14.87 | 15.99 | 11.09 | 10.07 | 9.82 | 10.85 | 12.10 | 15.05 |
| λ =30 m | 16.07 | 12.09 | 8.89 | 10.14 | 8.99 | 10.02 | 11.04 | 10.01 |
| λ =50 m | 12.97 | 14.90 | 9.08 | 7.94 | 5.89 | 6.00 | 6.91 | - |
| λ =100 m | 9.86 | 12.02 | 5.97 | 5.86 | 5.06 | 4.95 | 5.98 | - |

Tabata (1969) described the Japanese field experiments on a 350-metric ton patrol vessel during which both the ice growth rates and the spray events were measured (Zakrzewski, 1986a). The spray flux was measured aboard using toilet tissue collectors (Ryerson, 1995). Muzik and Kirby (1992) conducted spraying experiments in an artificial island Tarsiut Island in 1982, where spray water was collected in 45-gallon drums. No raw data was given, but the mean horizontal spraying flux density data was expressed as an empirical formula. Forest et al. (2005) later used these data and expressed the spraying frequency and liquid water content as a function of wave height. They presented a new spray generation algorithm that predicts a significant increase in spray flux due to wave-structure impact when the significant wave height exceeds a critical value of 3.15 m. This algorithm was implemented in RIGICE04 – a Canadian ice accretion prediction model. Although the island is analogous to a fixed offshore structure, "large" spray cloud observations may not be directly transferable to an offshore rig. More validation is required once full-scale or model scale data for a rig are available (Forest et al., 2005).

Spraying measurements on a rig Treasure Scout was also mentioned by Horjen (2015). Based on the measurements, Horjen and Vefsnmo (1985) presented a time-averaged spray mass flux formula. However, only the weather parameters were reported. The icing amount was estimated from photos and observations from the deck.

It can be noticed that in early studies researchers used buckets to collect the water and reported the data in the form of an empirical formula. Ryerson (1995) was the first to introduce modern technology in measuring spray properties. He measured the spray flux on a 115 m U.S. Coast Guard Cutter (USCGC) Midgett in the North Pacific Ocean and the Bering Sea during February and March 1990 – a vessel larger than a typical fishing boat (Figure 3-4). Using a stroboscopic droplet camera installed 10 m above the deck, he measured spray event duration, drop size and concentration, and liquid water content in the spray cloud. The observations showed that there is a range of droplet diameters from very fine, at 14 µm, to very large, at 7700 µm and the mean droplet concentration was $4 \times 10^5$ drops/m$^3$. This gives more information than the liquid water content alone. However, his model did not consider the droplet velocity data, which is crucial to obtain the path of a spray cloud around a vessel (Dehghani et al., 2016a).


FIGURE 3-4: DECK SPRAY ON CGC MIDGETT (RYERSON, 1995)

To identify thresholds for spray generation in terms of ship motions, Thomas (1991) carried out full-scale heavy weather sea trials on two comparatively larger ships: the USCGC Midgett in the Bering Sea, and the USS Monterey in the North Atlantic Ocean. The spray events were recorded by video cameras mounted on the forward superstructure. The bow spray data was compiled by counting the number of observed bow spray events during a 20-minute measurement at a constant heading. The time history of ship motions was simultaneously measured aboard both vessels using a Ship Motion Recorder (SMR) and a tri-axial accelerometer. The paper does not mention the sea states or ship's operating conditions explicitly. Thomas (1991) found that the onset of bow spray is not directly related to true wind or relative wind—neither alone can cause water to be lofted above the bow; if ship bow motions were insufficient to create a spray, then wind alone cannot generate spray clouds. Bow motion was measured by ship pitch and vertical acceleration in the forward part of each ship. The spray was created when the pitch was greater than 1.06° and vertical acceleration was greater than 0.19 g's on the CGC MIDGETT, and when the pitch was greater than 1.46° and acceleration greater than 0.22 g's on the USS Monterey. The smaller pitch angle and acceleration required to create spray in the CGC MIDGETT is attributable to the smaller size and freeboard of the Coast Guard Cutter. Generally, the CGC MIDGETT sprays about 8 to 10% more frequently than does the USS Monterey. In general, bow pitch acceleration was a reasonable predictor of spray event frequency on both the CGC MIDGETT and the USS Monterey. Once accelerations crossed the threshold for each ship, correlations were good except at the highest accelerations.

Lebiedzlnski and Thomas (1993) further analyzed the data for USS Monterey and presented a qualitative description of spray generation mechanisms and identified new spray criteria in terms of ship motions. They found that there is no single indicator of bow spray production, but indicated a vertical acceleration of 0.1 g as a threshold value for spray events. However, in some cases, they reported that even sufficiently large vertical accelerations did not produce spray, which led them to suggest that a ship experiencing a certain vertical acceleration combined with a distinct relative position between the ship and wave would be the best indicator of a spray event. Ryerson (2013) also analyzed the field data of Thomas (1991) and echoed that the vertical acceleration was a reasonable predictor of spray events on both vessels. The publications identified a threshold but did not give any formula to estimate spray frequency.

#### *3.3.1.2 Measurements of Full-Scale Icing*

Ryerson (1995) in his spray experiment also measured accreted ice thickness using an ultrasonic rangefinder. No reliable conclusion was drawn from 23 measured samples. To overcome the limitation of ultrasonic methods for spongy ice accretion, Chung et al. (1998a) developed a mechanical ice measurement sensor and installed it on the jack-up rig, Rowan Gorilla III, in the Sable island region, offshore Nova Scotia, Canada. The sensor measured the weight of the accreted ice and its moments on the vertical plate from 1992 to 1998 from which the average ice thickness was calculated. The meteorological data were also collected for all potential icing events. These data were than used to validate RIGICE predictions. Lozowski et al. (2002) designed a new icing sensor to measure ice accretion thickness up to 500 mm that was deployed on Rowan Gorilla III jack-up platform. They reported raw sensor data, weather data, wind speed, direction, and air temperature from November 1998 to Feb 2000.

Visual-based technology was implemented by Gagnon et al. (2009). They developed an automated icing detection and monitoring system, which consists of a CPU connected to two high-resolution digital cameras aboard the Atlantic Kingfisher, an offshore supply vessel. The cameras were positioned to view the foredeck and a portion of the ocean ahead and beside the vessel. The captured images were then processed using a simple image processing technique to estimate the amount of icing.

Various authors have compiled and published marine icing databases. Jones and Andreas (2012) compiled measured sea spray droplet concentration distributions from many experiments over the ocean done by many researchers near the ocean surface for wind speed from 0 to 28.8 m/s. From this concentration function, they derived a spray generation function to describe the sea spray flux which spans droplet diameters from 0.5 to 500 µm, including film, jet, and spume droplets and is valid for wind speeds up to 25 m/s. They mainly focused on the wind-generated spray, which they classified into two distinct groups. At moderate-to-high wind speeds (up to 20 m/s), it generates film and jet droplets which result in small ice accumulations. At very high wind speed, it produces spume droplets which cause high icing rates. Spume droplets are generated by the wind tearing water off the crests of waves. They assumed all of the impinging water freezes on impact, which may not be the case. Some of the droplets are deflected by airflow and fly around the structure (Kulyakhtin and Tsarau, 2014a). They proposed equations for spray concentration and liquid water content based on the wind velocity only.

The Canadian Hydraulics Centre of the National Research Council of Canada created a comprehensive marine icing database described in detail by Kubat and Timco (2005). The database contains survey data of more than 1200 events of marine icing for different environmental conditions collected from 1968 to 1980 on the east coast of Canada. Data was collected from different types of vessels such as fishing vessels, ferries, tugs, supply vessels, tankers, icebreakers, etc. The vessel length ranges from 35m to 150m. Different factors and parameters of icing are recorded. For example, geographic location, temperature, location of icing on the vessel, wind speed and air temperature, vessel speed and air temperature, wind direction, vessel heading, etc. This survey data can only give some qualitative assessments on icing severity for different environmental conditions but has limited usefulness in the formulation and evaluation of marine icing models and forecasts (Lozowski, 2017).

The database analyzed by Brown and Agnew (1985) in Canadian waters includes ships ranging in size from fishing trawlers to cargo ships. They found icing to be associated with seas of 2 to 4 m off the east coast of Canada and in Hudson Bay, but seas of 1 to 12 m in the Scotian Shelf area, the Grand Banks, and off Newfoundland. Seas of 6 to 8 m accompanied icing in the Gulf of St. Lawrence, Labrador Sea, and the eastern Arctic. The western Arctic had seas of less than 2.5 m during icing. Ryerson (1991) found that waves averaged about 1.6 m high, and swells 1.8 m off the Canadian east coast during icing.

Norwegian Coast Guard measured 37 cases of ice accumulation from three similar vessels: KV Andenes, KV Nordkapp, and KV Senja in the period 1983–1998. The data was published in 2017 by Samuelsen et al. (2017). More recently, the icing was observed in the Norne and Draugen fields in the Norwegian Sea, but no measurements were reported (Arctic Operations Handbook, 2013). To summarize, there are a few publications that give data on ice accretion as a function of environmental conditions. A comprehensive list of reported field measurements is compiled in Table 3-5.

TABLE 3-5: SUMMARY OF FIELD MEASUREMENTS CONDUCTED IN THE PAST

| Year | Category | Description | Reference |
|---|---|---|---|
| 1969 | Spray + Icing | Measured aboard a 350-metric ton patrol vessel using toilet tissue collectors | (Tabata, 1969) |
| 1975 | Spray + Icing | Measured spray on MFV Narva. | (Borisenkov and Pchelko, 1975) |
| 1976 | Spray | Measured spray frequency on MFV. | (Panov, 1976) |
| 1980 | Icing | Reported 39 cases of icing events | (Stallabrass 1980) |

| Year | Category | Description | Reference |
|---|---|---|---|
| 1980 | Icing | Icing measurement on semi-submersible rig Ocean Bounty during the winter of 1979-1980. | (Hansen et al., 2012; Jones and Andreas, 2009) |
| 1983 | Icing | 12 recordings of total ice accumulation from a stationary weather-ship AMI. | (Eide, 1983) |
| 1985 | Icing | Only published Alaskan data and 58 of them were selected and applied in Overland et al. (1986). | (Pease, 1985) |
| 1985 | Icing | The Ice Accretion Problem in Canadian Waters Related to Offshore Energy and Transportation | (Brown and Agnew, 1985) |
| 1986 | Spray | Measured on the whaling vessel Endre Dyrøy | Horjen (1986) |
| 1987 | Icing | 307 cases of icing in Canadian Water | (Roebber and Mitten, 1987) |
| 1988 | Icing | Offshore drilling rig SEDCO 708 and SEDCO 709 icing event, which includes 60 observations, were reported. | (Horjen, 2015) |
| 1989 | Spray + Icing | Icing events on offshore rig Treasure Scout | (Horjen and Vefsnmo, 1985) |
| 1989 | Icing | Reported 45 cases of icing events from a single stern trawler MT "Zandberg", and 115 cases translating Russian papers from the 1970s. | (W.P. Zakrzewski, 1989) |

| Year | Category | Description | Reference |
|---|---|---|---|
| 1990 | Spray + Icing | Superstructure spray flux and ice accretion were measured on a 115-m Coast Guard cutter in the North Pacific Ocean and the Bering Sea during February and March 1990. | (Ryerson 1995) |
| 1991 | Spray | Measured spray frequency on two coast guard vessels. | (Thomas, 1991) |
| 1992 | Spray | Spray measurements on Tarsuit Island | (Muzik and Kirby, 1992) |
| 2000 | Icing | Measured ice accretion on offshore rig Rowan Gorilla III jack up platform using weight sensors. Data were collected from November 1998 to Feb 2000. | (Lozowski et al., 2002) |
| 2005 | Icing | Compiled a database of more than 1200 icing events in Canadian water. | (Kubat and Timco, 2005) |
| 2009 | Icing | Used digital cameras aboard an offshore supply vessel Atlantic Kingfisher and estimated icing amount by image processing technique. | (Gagnon et al., 2009) |

| Year | Category | Description | Reference |
|---|---|---|---|
| 2017 | Icing | Norwegian Coast Guard measured 37 cases of ice accumulation from three similar vessels: KV Andenes, KV Nordkapp, and KV Senja in the period 1983–1998. The data was allowed to publish for scientific purposes in 2017. | (Samuelsen et al., 2017) |

### 3.3.2 Model Scale Experiments

#### *3.3.2.1 Measurements of Model Scale Spray*

The alternative to field measurement is to conduct model experiments. In model experiments, facility limitations determine the technique required to adequately represent the full-scale conditions. There are very limited data found in the literature related to model testing of marine icing. Most model experiments focus on simulating the icing process, while very limited interest in modeling spray generation was found. It is believed that the physics of spray generation is complex and cannot be reproduced by existing physical models (Kulyakhtin and Tsarau, 2014b).

Sea spray is widely modeled by spray nozzles both in the marine field (Kulyakhtin et al., 2016) and in the aerospace industry (Anderson 1995). Chung et al. (1998b), are among the few researchers who performed model scale experiments to obtain ship-generated spray in the clear water towing tank at the Institute for Marine Dynamics (IMD), National Research Council of Canada, in St. John's, Newfoundland. A 1:13.43 scale model of the stern trawler 'Zandberg', with an overall length of 3.83 m and beam 0.86 m, was used. 23 collecting gages installed on the deck were used to collect the spray. The ship was allowed to move freely in pitch, heave, and surge, but was constrained in roll, yaw, and sway. They found that the horizontal distribution of precipitating spray mass, averaged over many individual spray events, decays exponentially from the source (Chung et al., 1999). It should be noted that no attempt was made to scale the spray droplets during the experiment and the spray droplets produced during the experiment were unrealistically large at full-scale (Chung et al., 1998b). Based on their few test conditions (head wave only, ship speed (full scale) in the range of 2.5 to 8 m/s, and wave height 2.5 to 5 m), they proposed a spray flux formula, which is only applicable where wind drag is not significant (Chung et al., 1995). As the wind direction changes from 0 to 90 degrees, the total intercepted spray mass decreases due to the diminishing area of the spraying zone.

Sapone (1990), in a tow tank experiment, found that bows with increased flare (tested from 35 to 55° flare angles) reduce the wetted area of decks. Greater flare also reduced the volume of spray liquid water reaching decks, reduced the distance spray traveled aft, and produced finer drops at the deck edge than did bows with less flare angle. In his model experiments, Sapone (1990) used surfactants to reduce the surface tension of the water. In order to generate spray below the region of flare, spray root devices were fitted to each bow in the same manner as turbulent stimulators are fitted in the resistance test. The devices were made of plastic strips measuring 3.00 x 0.56 x 0.19 inches that were attached to each hull using silicon rubber cement. Various wavelength to ship length ratios were examined at Froude numbers that resulted in the greatest relative vertical velocity between the falling bow and rising wave. These combinations produced out-of-phase ship/wave motions and achieved the desired impacts, but also resulted in fore foot emergence and bow stem plunging with the associated shipping of water. To decouple the spray event from the deck wetting event (green water), the wave length was shortened to limit model pitching motions and its slope was steepened to increase the rate of convergence with the bow and spray root devices.

The hull form with a small flare angle and small knuckle collected the highest amount of spray water. Even though Sapone (1990) introduced the most sophisticated approach to scale down the critical spray properties, the water's Weber number (ratio of inertia to surface tension forces) was still 22 times smaller than the full-scale requirement. Scaling up the amount of water to full-scale would give an unrealistic and questionable value. Model experiments for spray are generally not reliable because Froude scaling cannot be applied to model spray generation for the water of natural surface tensions (Lebiedzlnski and Thomas, 1993) and even in this case where the surface tension was reduced, the reduction did not achieve perfect scaling.

Muzik and Kirby (1992) did a 1:30 scale model experiment of their full-scale measurements of spray events at Tarsuit Island. An interesting approach was used to match the droplet size with full-scale size by keeping the wind velocity the same as the full-scale measurements. Spray data were collected over half of the island by measuring the volume of water deposited on the model throughout a test. This volume was then doubled to give the total spray overtopping volume. The authors suggested interpreting the results as having at least ±15% possible error. The results are 2.5-3 times higher than the comparable field results. The authors suggested scaling the wind properly to model the amount and distribution of spray correctly.

Some simplified experiments on wave run up against a vertical wall in model scale (Bodaghkhani et al., 2018) and full scale (Aalbers and Poen, 2015), and splash produced by a free-falling buoyant sphere (Sampson et al., 1996) were reported, but they are not representative of the dynamic nature of ship-wave interactions, and therefore are not discussed here.

#### *3.3.2.2 Measurements of Model Scale Icing*

Most of the ice accretion model experiments discussed in the literature took place in an icing wind tunnel (Chen et al., 2015; Szilder et al., 2000). Szilder et al. (2000) performed a physical model test in a cold room to simulate marine spray ice accretion and developed a numerical model. They used a model scale factor of ten and used fresh water to avoid the complexity of the saline water freezing process. They analyzed the ice accretion as a function of water spray mass flux and the heat transfer conditions.

Koss et al. (2012) did model experiments on ice accretion on a circular cylinder. Chen et al. (2015) did a scale model study of ice accretion in a wind tunnel. They discussed in detail the scaling laws for icing, such as flow field similarity Reynolds number vs Mach number, energy balance similarity, water droplets trajectory and impact properties similarity, water catch similarity, etc.

Anderson (2003) discussed in detail several methods for scaling icing test conditions and compared various scaling methods. Tests were conducted with cylinders of different diameters in the Lewis Icing Research Tunnel (IRT). They used spray nozzles to control the liquid water content and droplet size. To measure the ice accretion rate, Owusu et al. (2013) designed a special capacitive probe that can also detect ice. The concept measures the change in capacitance and resistance due to ice accretion between two charged cylindrical probes. It can also detect the type of icing -glaze ice vs rime ice. It measures simultaneously the change in capacitance and resistance between two electrically charged cylindrical probes due to the presence of accreted ice on each probe surface.

Chung et al. (1998a) simulated the ice accretion in a cold room by running small fans to produce convective heat transfer. The unidirectional spraying was generated by using a handheld garden hose and a nozzle that produced droplets in the millimeter size range. The ice thickness was measured by inserting a sharp rod into the ice.

**TABLE 3-6: SUMMARY OF SCALE MODEL ICING EXPERIMENTS**

| Year | Data Type | Description | Reference |
|---|---|---|---|
| 1990 | Spray | Conducted spray experiments by scaling surface tension of water at MIT | (Sapone 1990) |
| 1992 | Spray | Measured both full-scale and model scale sprays on Tarsuit Island. | (Muzik and Kirby, 1992) |
| 1998 | Spray | Did a model scale experiments on MFV Zandberg at NRC | (Chung et al. 1998) |
| 2000 | Icing | Marine spray ice accretion in a cold room. | (Szilder et al., 2000) |

## 3.4 Review on Theoretical Spray Models

The rate of incoming water from wave-impact generated sea spray, which is usually the amount of water in a unit volume of air, is called Liquid Water Content (LWC). Most previous LWC formulas were developed based on field measurements conducted mainly on fishing trawlers (Borisenkov and Pchelko, 1975; Horjen, 1989; Zakrzewski, 1986b). The first LWC equation was given by Katchurin et al. (1974) as a function of wave height only. Borisenkov and Pchelko (1975) gave a non-dimensional formula based on their measurements on the Medium size Fishing Vessel (MFV) Narva. Later Zakrzewski (1986b) extended this formula for other parameters including wave height and ship speed relative to waves. Brown and Roebber (1985) also modified Borisenkov's formula and expressed the exponential term of the equation as a function of wave height. Horjen and Vefsnmo's formula (Horjen et al., 1988), which was based on spray measurements on a Japanese ship, is also expressed as a function of wave height only. Chung and Lozowski (1998) improved this method using model scale experiments with a Canadian fishing trawler, MV Zandberg. Their new model was also a function of wave heights and ship speeds. They indicated that the model is only valid for the ship and operating conditions they considered. Recently, Horjen updated the mass flux formula to include wind and ship speed parameters (Horjen, 2013).

The US Navy made spray measurements on larger-size coast guard vessels, but no LWC formula was given (Ryerson, 1995; Thomas, 1991). As mentioned earlier, Ryerson (1995) measured spray cloud and drop measurements with a stroboscopic video camera that was set about 10 m above the sea surface to avoid any damaging effects of green water but also to limit the camera to observe only spray events reaching that high. The sample volume that was viewed by the camera was 3.96 $cm^3$. Drops not sharply in focus were not considered because they resided outside of the defined sample volume. As a result, only about 2.5% of the drops passing through the sample volume appear in the video frames. No correction was applied for turbulence or variation in wind speed with height.

There are some numerical models developed to predict icing, mainly for offshore structures. However, when it comes to LWC and spray inflow, all of the models rely on the empirical formulas discussed earlier. Among them, the LWC formula of Zakrzewski (1986b) is the most popular. It was used in the computer model of spray (Lozowski et al., 2000), in computational fluid dynamics (CFD) simulation (Shipilova et al., 2012), in MARICE (Kulyakhtin and Tsarau, 2014a), and in recent numerical models (Dehghani et al., 2018, 2016b). Samuelsen et al. Samuelsen et al. (2017) used both Zakrzewski's (Zakrzewski, 1986b) and Horjen's (Horjen et al., 1988) formula and concluded that Horjen's formula severely under-predicts LWC for low wave conditions. In RIGICE4 (Forest et al., 2005) and ICEMOD (Horjen, 2013), the authors used their own empirical LWC formula developed from measurements on fixed offshore structures discussed in Section 3.3.1.1 .

Once the cloud of spray water is produced, it travels over the ship due to wind action and impinges on vertical surfaces or falls onto the deck. The time it remains airborne after formation is the duration of the spray event. This is another important parameter of sea spray. This duration, together with spray velocity, determines where the ice would build up on the deck and also determines the icing rate. The duration depends on the ship speed relative to the wave at impact, the relative wind speed (Zakrzewski, 1986a), hull shape, and the nature of the ship-wave impacts.

Thomas (1991) also found that relative wind speed played a role in determining the duration of spray events. Zakrzewski (1986a) proposed an empirical formula based on the data collected on the fishing vessel Narva (Eq. (2)). The formula was later modified by Lozowski et al. (2000) to match Ryerson's data (Ryerson, 1995) for the larger size cutter USCG Midgett (Eq. (3)). Samuelsen et al. (2017) argued the validity of Eq. (3) and proposed a new one based on linear regression analysis of Ryerson's data (Ryerson, 1995) (Eq. (4)). Horjen (2013) gave a theoretical expression for the duration of spray considering wavelength and relative wind speed to ship speed.

$$t_{dur} = 20.62 \frac{H_s V_{sw}}{V_a^2} \tag{2}$$

$$t_{dur} = 10 \frac{H_s V_{sw}}{V_a^2} \tag{3}$$

$$t_{dur} = 0.123 + 0.7009 \frac{H_s V_{sw}}{V_a} \tag{4}$$

where $H_s$ is the significant wave height, $V_{sw}$ is the relative velocity between significant waves and the vessel, $V_a$ is 10 m wind.

Ship response to waves determines the frequency of spray generation. In general, vessels with shorter pitch periods spray more frequently (Ryerson, 2013). Spray frequency is an important parameter since it affects the icing process. If the spray frequency is low, the impinging water will have more time to freeze and create an ice layer or add to ice previously formed (Ryerson, 2013). Only a few field experiments (Horjen et al., 1986; Panov, 1976; Thomas, 1991) attempted to register the frequency of spray generation. Field observations on the spray frequency of MFV Narva were reported by Panov (1976) and an empirical formula was proposed (Eq. (5)) where the period between successive ship-wave encounters $T_{sw}$ was estimated (Zakrzewski, 1986b) by Eq. (6).

$$N_s = 15.78 - 18.04 \exp\left(-\frac{4.26}{T_{sw}}\right) \; [\min^{-1}] \tag{5}$$

$$T_{sw} = \frac{\lambda}{V_{sw}} = \frac{\lambda}{1.25\sqrt{\lambda} - V cos\beta} \quad [s] \tag{6}$$

where $\beta$ is the heading angle and $\lambda$ is the wavelength. The Eq. (4) is recommended only for MFV's of Soviet-type for $15 \geq T_{sw} \geq 3.5s$ (Zakrzewski, 1986b).

Horjen (2013, 1989) and Zakrzewski (1986b) hypothesized that every second significant wave produces spray on an MFV type vessel and used Eq. (7). However, Horjen (2013) suggested that the spray frequency along with the spray duration and spray mass flux need more study. Lozowski et al. (2000) assumed that for a larger vessel like the USCGC Midgett, spray generates from every fourth ship-wave collision (Eq. (8)) and applied this hypothesis to analyzing Ryerson's data (Ryerson, 1995). This assumption was also supported by Samuelsen et al. (2017) and was applied to predict icing on a similar-length vessel, MS Nordkapp.

$$N_s = \frac{V_{sw}}{2\lambda} = \frac{1}{2T_{sw}} \; [s^{-1}] \tag{7}$$

$$N_s = \frac{1}{4T_{sw}} \; [s^{-1}] \tag{8}$$

The above formulas are based solely on the ship's relative velocity, a parameter that does not account for the geometry or seakeeping characteristics of the vessel (Lebiedzlnski and Thomas, 1993). The hull forms of other types of vessels differ significantly from fishing vessels resulting in different motion responses to waves. The seakeeping characteristics, therefore, will be different for each type of vessel (Thomas, 1991).

In determining the threshold criteria, neither Lebiedzlnski and Thomas (1993) nor Ryerson (2013) considered the relative freeboard of the vessels. A vessel with a greater freeboard tends to deflect spray away and reduce the entrainment of drops into the relative wind (Ryerson, 2013). Therefore, it may see less spray water, even with the same pitch and accelerations. It is evident in the published data that the USCGC Midgett sprays about 8 to 10% more frequently than does the USS Monterey which can be attributed to the smaller size and freeboard of the former.

The limiting freeboard criterion is common in deck wetness calculations where the Rayleigh distribution for the probability calculation is generally used (Sasa et al., 2019). Buchner et al. (2014) found the probability of freeboard exceedance calculated by the traditional Rayleigh distribution significantly underestimates the non-linear relative wave motions and developed an empirically modified Rayleigh distribution. Theoretical distribution of non-linear motions in the prediction of deck wetness for the sandglass-type floating body was proposed by Du et al. (2017). The deck wetness is calculated by considering the relative vertical motions between a ship's bow and the instantaneous height of the waves (Du et al., 2017; Sapone, 1990). These calculations do not take the velocity of the incoming water into account. However, if the velocity of the rising water is high (as in the case of a spray event), the bow flare may deflect the water away from the deck edge and deck wetness may occur in the form of finer drops, or may not occur at all if there is no wind.

For the deck to be wet, Lloyd et al. (1986) report that both the relative motions and water velocity should be considered simultaneously. They state that along with the freeboard exceedance at some stations, the absolute vertical velocity of the water surface at the same station must be less than a critical velocity for a deck wetness event to happen. The freeboard exceedance leads to a possibility of either a deck wetness event or a spray generation event. Du et al. (2017) identified both mechanisms in their model experiments. However, their model only accounts for the overtopping deck wetness, and ignores the splashing events since the amount of shipped water due to the later mechanism was relatively small.

Blackmore and Lozowski (1997, 1994), in their spray model, assumed that spray water decreases with an increase of freeboard. They also included the vessel length in the model as a "spray access window" whose length was assumed as half the ship length and height was assumed proportional to the wave group velocity. The spray flux was estimated by dimensional analysis. All the proportionality constants were derived from the field data of MFV Narva (Zakrzewski, 1986b). The characteristic motion of the vessel was not considered. No spray frequency and no criteria for spray generation were given.

Overland (1990) proposed a spray generation threshold as a function of ship length based on seakeeping theory. However, the threshold was set based on deck wetness, and not on spray generation. Ryerson (2013) explained that seawater shipped on board as evidenced by deck wetness is less likely to freeze due to insufficient time for heat to be removed from the large mass of water. Sapone (1990) distinguished between deck wetting and spraying based on the delivery process of the seawater. A high dynamic pressure zone accompanied by a large pressure gradient causes the fluid to accelerate rapidly. This accelerated fluid goes through a primary and secondary breakup to form droplets as explained in Section 2.2.3 In deck-wetness events, the locally elevated water mass exceeding the local freeboard moves inwards onto the weather deck due to the momentum of the wave and collapses under the influence of gravity. It can be concluded from the above discussion that the critical velocity of the rising water distinguishes between the two events. Spray can be called a form of deck wetness, but not all deck wetness events are spray-events.

Hull shape also influences the amount of spray lofted over the superstructure. Ships with greater freeboard in the bow area and greater bow flare tend to deflect spray away and reduce entrainment of drops into the relative wind (Ryerson, 2013). Sapone (1990) reported that bows with increased flare reduced the wetted area of the deck, reduced the distance spray traveled aft, and produced finer drops at the deck edge than did bows with less flare.

## 3.5 Review on Numerical Spray Models

Discretizing the governing equations for very fine water droplets over a very large domain in the size scale of a vessel makes numerical simulations of spray very challenging. Grid-based computational fluid dynamics (CFD) can be used to simulate the spray process; however, it faces two difficulties. First, low-quality mesh deformation usually introduces large numerical errors, and second, mesh reconstruction requires high computing time (Qu et al., 2016). Fragmentation and large reconstruction of breaking free surfaces create numerical instability due to mesh overlapping and domain distortion (Domínguez et al., 2019; Kanehira et al., 2020; Zha et al., 2021). For example, simulations of bubble, droplet, and spray formation in plunging breaking waves were conducted using a grid-based code CFDSHIP-IOWA (Z. Wang et al., 2016). It took millions of CPU hours at the US DoD supercomputing center to simulate a wave of only 27 cm long.

A large domain of 500 m by 125 m of ocean surface was modeled to study wind-generated sea spray using the Numerical Flow Analysis (NFA) code (Dommermuth et al., 2014, 2007). Various types of jets forming from an 8.98 m long wave were captured using an enormous 17.2 billion grid points (Dommermuth et al., 2014). Despite the number of grid points, no droplets were produced because the grid resolution of 6.1 cm was too large. The simulations were performed on the SGI ICE X at the US Air Force Research Laboratory and the Cray XE6 at the US Army Engineer Research and Development Center. Fifty seconds of simulation ran for 740 hours and generated 275 TB of data. Fu et al. (2013) used the NFA to produce the formation of a ship-generated spray sheet. A tightfitting domain of about 3 m by 1.5 m size was meshed by 514 million grid cells. A Cray XT6 with 576 processors took approximately 24 hours to complete the simulation.

Lagrangian meshless methods, on the other hand, bring significant advantages over classical mesh-based methods to simulate the breaking wave impact phenomenon (Guilcher et al., 2014). The Lagrangian motion of particles enables non-diffusive simulation and thus allows for very sharp interfaces. It proves to be well adapted for multi-species problems. Smooth Particle Hydrodynamics (SPH)- a meshless Lagrangian particle-based method is a widely validated and accepted method for solving violent flows (Kanehira et al., 2020; Kawamura et al., 2016; Roselli et al., 2019; Shadloo et al., 2016; Zha et al., 2021). The method can avoid numerical diffusion, the governing equation is free of convective terms, hence avoids numerical errors that can be seen in Eulerian methods (Kanehira et al., 2020).

SPH-based open-source solver DualSPHysics has been successfully employed by many researchers to study violent free surfaces (Altomare et al., 2020; Kanehira et al., 2020; Kawamura et al., 2016; Roselli et al., 2019; Tagliafierro et al., 2021). Green water shipping onboard a vessel was simulated and validated against model scale experiments by Kawamura et al. (2016). Two different size domains were created, one for transient motion in the following sea and the other for the periodic steady-state in the stern quarter sea. Water depth was reduced to one-third, shifted from deep water to shallow water, for the quarter sea to accommodate the limitation of computing resources.

Short crested and multi-directional waves in a circular basin were modeled by Kanehira et al. (2020), where a reasonable agreement was reported against the model scale experimental data. Waves with lower frequencies and steepness were better predicted than the higher frequency and steeper waves. Finer resolution of the domain with a larger number of particles or adaptive resolution was suggested to improve very high-frequency waves.

Roselli et al. (2019) simulated the surf zone originating from wave breaking and run-up on sloped beaches in shallow water based on DualSPHysics solver. Validation against experimental data showed that the wave-breaking kinematics were well captured. The maximum errors in the wave crests and troughs were found after wave splash-up, where fragmentation of the free surface occurred. Air entrapment in the experiment was identified as a possible factor that was not modeled, limiting the accuracy of the simulation. A multi-phase solver was recommended to improve the prediction.

A full-scale SPH simulation of a wave impacting a large pier in a sea storm was simulated by Altomare et al. (2020). The water surface elevation and velocity field were extracted from the two-dimensional (2D) simulations and applied as a forcing boundary condition in the two-dimensional (3D) simulations, eliminating the requirements for a very large domain for the waves to fully develop. Domínguez et al. (2013) also demonstrated a full-scale SPH simulation of wave impacting an oil rig with a large fluid domain of 170 m × 114 m × 68 m. A particle spacing of 6 cm generated more than 1 billion particles and was computed on 64 GPUs [Tesla M2090] for almost a week.

Most of the numerical simulations of water spray, green water, or breaking wave in the past studies were conducted in model scale; either in 2D (Roselli et al., 2019) or 3D (Kawamura et al., 2016; Silva et al., 2017; Z. Wang et al., 2016). Full-scale 3D simulations were carried out mostly for resistance and self-propulsion and were validated against model scale data (Begovic et al., 2020) or other potential theories (Tezdogan et al., 2016). Most 3D models use zero forward speed of the ship (only heave and pitch) in the simulation (Greco et al., 2013), or prescribed motions extracted from model experiments (Silva et al., 2017) to minimize the domain size.

To the best of the author's knowledge, wave-generated spray for ships in full scale has never been simulated. Very recently, Tagliafierro et al. (2021) simulated whisker spray generated by a high-speed planing hull at Fr = 1.443 in calm water using DualSPHysics. No quantitative validation was presented, only a qualitative depiction of the spray was discussed.

Once a water droplet is ejected from the sea water, it interacts with the airflow, exchanges momentum, heat, and moisture with the surrounding air (Veron, 2015). Bigger droplets can further break up to form smaller droplets through the droplet breakup phenomenon (Dehghani et al., 2017; Veron, 2015). Droplet trajectories from the ejection spots toward the marine vessel determine the rate of water droplets received on the vessel (Zakrzewski et al., 1988).

The trajectory depends on the gravity force, wind velocity, initial size and velocity of droplets, and many other parameters. Among them, droplet size distribution, droplet velocity distribution, and droplet concentration are the crucial input for droplet trajectory analysis (Dehghani et al., 2016a; Zhuang et al., 1993). Using Newton's law, the equation of motion of a single spherical droplet can be established (Lozowski et al., 2000; Zakrzewski et al., 1988). However, these analytical models cannot take into account Faxen effects (effects of flow curvature), Saffman lift (lift effects from velocity gradients in the air), and Magnus effect (effects from the rotation of the drop). Among the listed factors, droplet concentration is generally ignored in past studies by assuming the spray cloud is dilute and droplets travel over the vessel individually without affecting each other (Dehghani et al., 2018, 2016b, 2016b; Kulyakhtin and Tsarau, 2014a).

Simulation of the break-up of the fluid into these droplets is in its early development stages (Cleary and Serizawa, 2019). A large number of droplets and their variations in size, and the necessary presence of air and water phases to obtain proper spray behavior make the simulation complex (Nielsen and Østerby, 2013). Currently, CFD simulations of sprays are being conducted in various ways: Direct Numerical Simulation (DNS), Reynolds-averaged Navier Stokes (RANS), Large Eddy Simulation (LES) all of which are based on solving the Navier-Stokes equations in an Eulerian framework (Pereira et al., 2018).

Eulerian-Lagrangian methods can be considered a better alternative to circumvent this mesh tangling problem, where the water sheet is generated in Eulerian space that converts into droplets in Lagrangian space. Droplet impingement and droplet distribution were studied by Kulyakhtin et al. (2014) using this approach, where a discrete phase model (DPM) of FLUENT was used to estimate the trajectories of the droplets of sizes in the scale of micrometers (13.1, 17.1, and 45 μm), which are the characteristic size of jet droplets (Veron, 2015). The concentration of droplets was assumed dilute, and the interactions among them and their influence on the airflow were neglected. Nielsen and Østerby (2013) used Eulerian grids for water and Lagrangian particles for individual droplets, and heuristic algorithms to create transitions between the two in their water spray simulation.

The recent development of VOF to DPM model within commercial CFD codes (StarCCM+, FLUENT) simulates liquid lumps in VOF, where Adaptive Mesh Refinement (AMR) can be applied to refine mesh dynamically only in areas of interest. The model looks for liquid lumps that separate from the main liquid body and converts them to point masses based on the conversion criteria (sphericity and droplet size range) set by users rather than the outcome of the simulation. The natural transition from liquid to droplet is very complex for the Eulerian-Lagrangian method (Pereira et al., 2018).

SPH has the potential to offer significant advantages where significant amounts of free surfaces are being constantly created and where droplet collisions are possible (Pereira et al., 2018). This method can model both water sheets and droplets without requiring any complex transitions between them, making it a reasonable choice for simulating spray. A coupled SPH-DEM approach was proposed by Cleary and Serizawa (2019) and Li et al. (2018), where the droplets were modeled as discrete entities using the Discrete Element Method (DEM), and SPH was used to model contiguous fluid. This approach allows modeling collisions between droplets and preserves the spherical shape of the droplets. Zhao et al. (2018) demonstrated an application of SPH to simulate water spray generated from airplane tires. In this study, a fully Lagrangian meshless SPH method is, therefore, utilized.

### 3.6 Summary

From the review of the literature, it can be seen that the conditions which result in wave generated spray freezing on the superstructure of a ship or an offshore platform are extremely complex, and the amount of accumulated ice will depend on the meteorological conditions (wind speed, air temperature, water temperature and freezing point of seawater), the resulting wave heights, and the vessel speed and direction of motion relative to the waves. There is evidence that the amount of ice will vary also with height above the waterline, the shape of the structure above the waterline, and the distance along with the structure from where the spray is generated, most commonly the bow area of the ship. A rigorous treatment of ice accretion requires a detailed understanding of the specific conditions determining the interaction between the structure and the environment, including the wind flow around the structure. Assessing specific cases, using physics-based approaches would be the ideal outcome, and methods such as CFD, to study the complete problem may lead to future applications for design studies, but they require specialist knowledge and are time-consuming to apply.

The amount of superstructure icing on a ship or floating offshore platform is needed primarily to assess the impact of the additional weight on the hydrostatic stability. The additional weight and resulting reduction in the maximum righting arm have resulted in the loss of many ships, usually small fishing vessels, due to ice build-up. Other factors, such as safe access to decks and walkways by the crew and the operation of equipment onboard the ship also require an understanding of the build-up of frozen spray.

Current trends within regulations are moving toward goal based design rather than prescriptive rules. In order to successfully apply goal based design to ice accretion, we need to combine a method of predicting icing conditions with the amount of ice that will accumulate. This requires knowledge of the conditions likely to cause icing for the area where the ship or offshore structure will operate, the length of exposure to those conditions, the geometry of the structure, and some knowledge of where the ice will accumulate and to what depth, which can finally lead to the stability or other safety factor assessment. All of these elements are presented in separate places, but nothing in the reviewed literature brings them all together into a unified methodology.

To develop a full methodology of goal based design for ice accretion there are two critical knowledge gaps, both of which are complex to close, and require new methods and techniques. One is a comparison of ice accretion rates for different structures in the same icing conditions. This should include large ships, small ships, and offshore structures. The second knowledge gap is validation data that compares predicted ice growth rates for all types of ship and offshore structures against observed values. Computer codes and experiment facilities are not yet at the level of development required to study the whole problem. The complex interaction between the structure and a multi-phase fluid, including spray are not fully understood.

The first knowledge gap requires experiments or simulations for different types of structures in the same nominal icing conditions, including the effect of sea states. The second gap requires observations from sea trials with different types of ships in a range of different conditions, and preferably some cases where data are recorded two types of structures are recorded simultaneously. Given the relative rarity of conditions when ice accretion occurs, this presents a significant challenge. There are some useful databases (e.g. Kublat and Timco, 2005) that can be used for high-level correlation studies in the same manner as Overland et al. (1986). The eventual goal is a modified value of Overland et al.'s ice predictor for different sizes of ships, different types of offshore structures, and possibly different levels of fetch, where significant wave heights would be different for the same wind speed.

The current study dedicates to fill two crucial gaps in ice accretion prediction research:

1. Development of a novel spray generation model applicable to any sizes and types of vessels – which is the basis of the theoretical model of the current study and is discussed in Chapter 4.
2. Development of a benchmark numerical simulation to compare spray generation rates and their distributions for different structures in the same icing conditions and sea states, which is covered in Chapter 5.

# Chapter 4 :

# Theoretical Model

## 4.1 Introduction

Early works provided climatological estimates of icing, generally ignoring ship dynamics although acknowledging its importance. For example, Zakrzewski (1989) reported: "the differences in size, mass, and ship design will result in differences in the ship-wave interactions, even though the ship [forward] motion and air-sea parameters may be the same". Field measurements (Thomas, 1991) also confirm that different types and sizes of vessels have different levels of vulnerability to spray. Classification societies require an effective analysis tool to estimate the extent of icing during a particular voyage. In this study, this gap is filled with a simple model that considers all the relevant parameters. Some of the previously discussed limitations are addressed by developing a threshold to calculate the probability of spraying and subsequently estimating the frequency of spray generation considering ship motion characteristics, spray water jet velocity, and bow geometry.

Due to the ship's motion and the effects of wind drag and gravity, spray droplets can eventually impinge onto the ship's exposed surfaces. To determine time-averaged spray flux onto a ship, three major spray parameters need to be estimated: 1) the amount of water produced in a single ship-wave impact, 2) the frequency of spray generation, and 3) the distribution of spray water on the surface of the deck and superstructure. This chapter deals with the first two parameters. The third parameter is analyzed in Chapter 5, section 5.5.

## 4.2 Derivation of the Spray Properties

The impact between a ship and a wave can be considered as a combination of a water entry problem and the problem of a wave breaking against a wall. The main difference between the two mechanisms is that in the former the kinetic energy results from the fast-moving solid, whereas in the latter the kinetic energy results from the fast-moving liquid (Dias and Ghidaglia, 2018). In the ship-wave impact case, the resultant kinetic energy is a combination of both mechanisms. The research presented in this thesis has evolved around this dual energy principle to derive formulas for LWC and spray duration. It was assumed that LWC and spray duration are proportional to the total dissipated energy due to the impact. This makes the model applicable to any size and type of vessel. An energy-based spray mass flux formula was proposed by Horjen (1989) considering only the wave energy and neglecting the size effect of the ship. The following section discusses the present method.

When waves impact or collide with structures such as ships, offshore platforms, or coastal structures, clouds of droplets are generated under certain conditions as described in Section 2.2. The primary source of water in spray icing is the lofting of water over the ship's bow as a result of the bow plunging into waves and swells (Ryerson, 1995). When the bow encounters a wave, it may cause a jet or sheet of water to rise above the ocean surface along the hull of the ship, due to the displacement of the wave by the bow as described in Section 2.2.2 . As the water jet rises, the air is entrained, and the jet begins to break into drops. The amount of water that falls on a deck for any given period is described by spray flux (Samuelsen et al., 2017; Zakrzewski, 1986b) as

$$F_s = EV_d l_{wc} N_s t_{dur} \ kg/m^2 s \tag{9}$$

where $E$ is the collection or collision efficiency of the droplets, $V_d$ is the droplet velocity (m/s), $l_{wc}$ is the liquid water content of the spray (kg/m$^3$), $N_s$ is the spray frequency (s$^{-1}$), and $t_{dur}$ is the duration of the spray cloud (s). In this work, the focus is on estimating three essential parameters: $l_{wc}$, $N_s$, and $t_{dur}$. Collection efficiency was estimated by Kulyakhtin and Tsarau (2014a), and $V_d$ can be estimated by previous trajectory models (Dehghani et al., 2016a; Lozowski et al., 2000; Mintu et al., 2019).

### 4.2.1 Liquid Water Content (LWC)

LWC is the first and most important input for spray icing prediction and is important for a good estimation of ice accretion (Kulyakhtin and Tsarau, 2014a). The phenomena of breakup and atomization caused by wave impact on a vessel's bow have not yet been investigated although there are some reports with introductory ideas about these phenomena (see Section 2.2.3 ). A simplistic approach is proposed here. The objective is to develop an LWC formula taking into account ship size, operating conditions, and weather conditions. It is assumed that LWC is proportional to the total energy produced due to a particular ship-wave collision. That is

$$l_{wc} \propto \mathrm{E_T}$$
$$l_{wc} = C_s . \mathrm{E_T} \tag{10}$$

where $\mathrm{E_T}$ is the total ship-wave impact energy and $C_s$ is a spray constant that is to be derived from field measurements. Considering the exponential vertical distribution of the spray water as proposed by Borisenkov and Pchelko (1975), Eq. (10) can be written as

$$l_{wc} = C_s . \mathrm{E_T} . \exp(-0.55h') \text{ kg/m}^3 \tag{11}$$

where $h'$ is the elevation of the spray cloud above the deck.

$E_T$ can be estimated as

$$E_T = \sqrt{{E_\xi}^2 + {E_S}^2} \quad (12)$$

where $E_\xi$ is the total wave energy that can be derived from linear wave theory as

$$E_\xi = \frac{1}{8}\rho g {H_s}^2 \lambda |B_e| C_f \quad (13)$$

where $\rho$ is the density of water, $g$ is the gravitational constant, $H_s$ is significant wave height, $\lambda$ is the wavelength, $C_f$ is the bow flare coefficient responsible for the bow-shape effect on the spray quantity. $C_f$ is defined by Jensen and Mansour (2003) as

$$C_f = \frac{0.4}{tan\alpha} \quad (14)$$

where $\alpha$ is the stem angle of the ship hull.

$B_e$ is the effective beam of the vessel defined in a simple way as

$$B_e = \begin{cases} \dfrac{B}{cos\beta} & (for\ 0^0 < \beta < 90^0) \\ L_{BP} & (for\ \beta = 90^0) \end{cases} \quad (15)$$

where $\beta$ is the ship's heading angle relative to wave and $L_{BP}$ is the ship's length between perpendiculars.

The magnitude of the impact of a moving ship depends on the kinetic energy carried by the ship (Bhattacharyya, 1978). This kinetic energy is dissipated through the deformation of the wave if no deformation for the ship's hull is assumed. Ship impact energy due to forward motion (relative velocity (Bhattacharyya, 1978)) is calculated as

$$E_S = \frac{1}{2} m V_{sw}^2 \tag{16}$$

$$V_{sw} = Vw - Vs.\cos\beta$$

$$m = \rho.(1 + m_a).L.B.T.C_b.$$

where $V_{sw}$ is the ship speed relative to the incoming wave celerity, $Vw$. $m$ and $m_a$ are the mass and the added mass of the ship, respectively. $Vs$ is the ship's speed at heading $\beta$. $T$ and $C_b$ are draft and block coefficient of the hull, respectively. The added mass of the ship is a function of ship responses to waves (Bhattacharyya, 1978). The value can be estimated from Lewis form factors. For simplicity, a fixed value is assumed.

To derive the spray constant, $C_s$, the field data of Borisenkov and Pchelko (1975) was used. The LWC was expressed by the formula in current notations as

$$l_{wc} = 2.42x10^{-2}\exp(-0.55h') \text{ kg/m}^3 \tag{17}$$

$h'$can be taken from the sea surface elevation as described by Samuelsen et al. (2017) and Eq. (17) becomes

$$l_{wc} = 2.42x10^{-2}\exp\big(-0.55(z - 3.5)\big) \text{ kg/m}^3 \qquad z \geq 3.5\ m \tag{18}$$

where $z$ is taken from the sea level instead of the deck level. Eq. (18) can be re-written, in a similar way to Zakrzewski (1986b), to include the energy term as follows

$$l_{wc} = w_0 * \frac{\mathrm{E_T}}{E_{T_0}} * \exp\big(-0.55(z - 3.5)\big) \text{ kg/m}^3 \tag{19}$$

where $w_0 = 2.42x10^{-2}$ kg/m$^3$ from Eq. (17). The total impact energy of the MFV Narva, $E_{T0}$, is calculated for a ship speed of 2.83 m/s moving forward at a heading angle of 100 degrees relative to a significant wave height of 3.09 m and a wave period of 6.8 s as reported by Zakrzewski (1986b). The ship particulars are tabulated in Table 4-1. The value of spray constant $C_s$ is therefore calculated as $4.69x10^{-10}\ s^2m^{-5}$. This constant covers all unknown factors such as the effect of air entrapment, wave diffraction and so on. The new expression for LWC thus becomes

$$l_{wc} = 4.69e^{-10}.\mathrm{E_T}.\exp\big(-0.55(z - 3.5)\big)\ \text{kg/m}^3 \tag{20}$$

This expression can be used for any size and type of vessel. The effectiveness of this expression is examined in the validation studies section.

### 4.2.2 Duration of Spray

The duration of spray is redefined considering the following assumptions:

1. The duration of spray is proportional to the total energy dissipated during a given collision. The more energy it dissipates, the more time the spray cloud remains flying.
2. The duration is inversely proportional to the relative wind speed as reported by Zakrzewski (1986a).

3. Hull shape also affects the duration of the cloud as suggested by Zakrzewski (1986) (1986a).

Using dimensional analysis, the following expression for spray duration was developed.

$$t_{dur} = \frac{E_T}{g C_f \Delta V_{wr}} \quad (21)$$

where $E_T$ is the total energy released during the ship-wave collision, $C_f$ is bow flare coefficient (Eq. 14), $\Delta$ is mass of the vessel in kg, and $V_{wr}$ is the relative wind speed.

### 4.2.3 Derivation of Spray Frequency

#### *4.2.3.1 Spray Frequency*

The frequency of spray events affects the icing process. Previous spray frequency formulas are derived empirically from field observations considering only the ship's forward speed and oceanographic conditions. The significance of various degrees of ship motions on the spray frequency is ignored. However, in reality, the interrelationships of heave and pitch motions under wave actions together with surge motion determine the number of spray events that a ship may experience in a given period. ShipMo3D analysis at the early stage of this research reveals that there is a correlation of ship motion with spray as shown in Figure 4-2. The figure shows ship's heave velocity and vertical acceleration are contributing significantly to the time-averaged spray flux reported by Samuelsen et al. (2017).

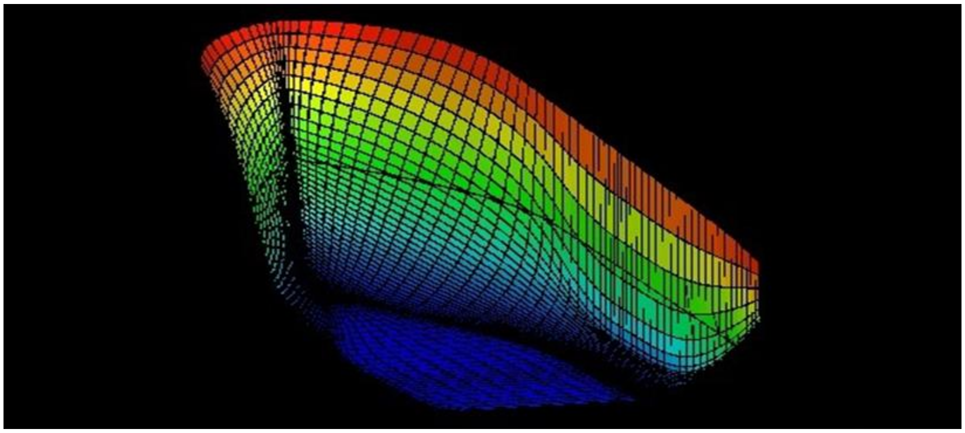

**FIGURE 4-1: SHIPMO3D HULL MODEL**

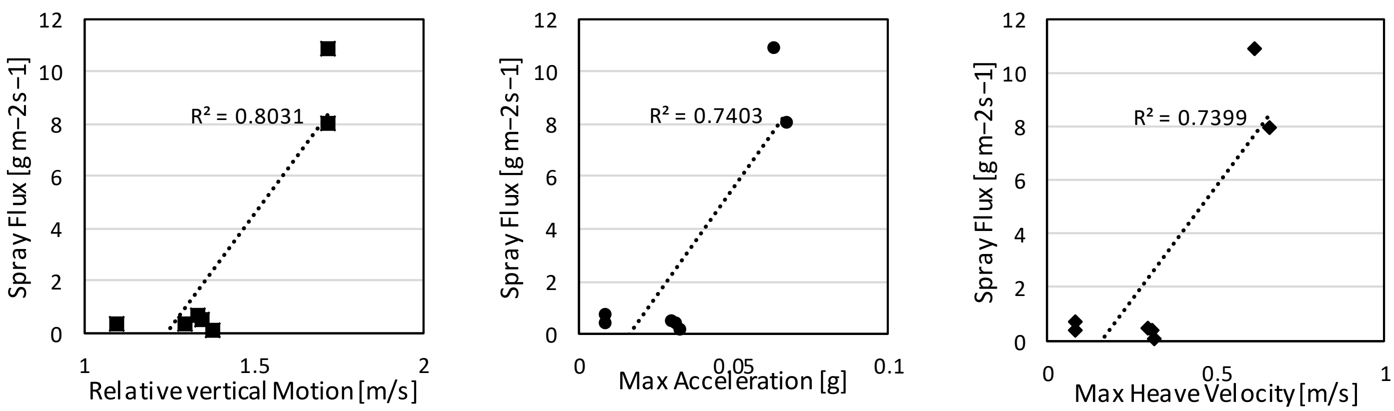


**FIGURE 4-2: RELATIONSHIP BETWEEN SHIP MOTIONS AND SPRAY FLUX**

To incorporate ship size and motion, a theoretical model for estimating the frequency of sea spray can be proposed. Ship motions can easily be estimated by strip/panel methods. However, in this work, we propose a simple framework for a quick estimate of spray frequency. The model inputs are, therefore, restricted to the ship's principal particulars, its operating conditions, and environmental conditions.

#### 4.2.3.2 Ship Motions

Ship motions were computed using the semi-analytical expressions given by Jensen et al. (2004). For completeness of the current work and to correct an error in the original reference (personal communication), the formulas are reproduced here.

The frequency response functions $\phi_z$, $\phi_\theta$ for heave (z) and pitch (θ), for the vertical wave-induced motions of a homogeneously loaded box-shaped vessel can be derived analytically by linear strip theory. By neglecting the coupling terms between heave and pitch and assuming a constant sectional added mass equal to the displaced water, the equations of motion in regular waves with amplitude $a$ can be written as

$$2\frac{kT}{\omega^2}\ddot{z} + \frac{A^2}{kB\alpha^3\omega}\dot{z} + z = aF\cos(\varpi t) \tag{22}$$

$$2\frac{kT}{\omega^2}\ddot{\theta} + \frac{A^2}{kB\alpha^3\omega}\dot{\theta} + \theta = aG\sin(\varpi t) \tag{23}$$

where $T$ is the draft of the vessel, $B$ is the beam. The wavenumber, $k = \frac{\omega^2}{g}$, $\omega$ is the wave frequency, $g$ is the gravitational constant. The frequency of encounter $\varpi$ is given by

$$\varpi = \omega - kV_s cos\beta \equiv \alpha\omega \tag{24}$$

The solution of Eq. (22) and Eq. (23) gives frequency response functions for heave and pitch, respectively as

$$\phi_z = \eta F \tag{25}$$

$$\phi_\theta = \eta G \tag{26}$$

where,

$$\eta = \frac{1}{\sqrt{(1-2kT\alpha^2)^2 + \left(\frac{A^2}{kB\alpha^2}\right)^2}} \tag{27}$$

$$\alpha = 1 - F_n\sqrt{kL}cos\beta \tag{28}$$

$$F_n = \frac{V_s}{\sqrt{gL}} \tag{29}$$

where $V_s$ is the ship speed, $L$ is the length of the vessel, and $\beta$ is the heading angle relative to the wave direction as shown in Figure 4-3. ($180^0$ corresponding to head sea).

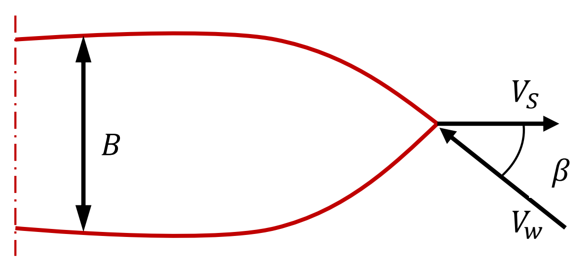


**FIGURE 4-3: COORDINATE SYSTEM**

The sectional hydrodynamic damping, $A$, is modeled by the dimensionless ratio between the incoming and the diffracted wave amplitudes with the following approximation (Jensen et al., 2004)

$$A = 2\sin\left(\frac{\bar{\omega}^2 B}{2g}\right)\exp\left(-\frac{\bar{\omega}^2 T}{g}\right) = 2\sin\left(\frac{1}{2}kB\alpha^2\right)\exp(-kT\alpha^2) \tag{30}$$

The forcing functions $F$ and $G$ are given by

$$F = S_c f \frac{2}{k_e L}\sin\left(\frac{k_e L}{2}\right) \tag{31}$$

$$G = S_c f \frac{24}{(k_e L)^2 L}\left[\sin\left(\frac{k_e L}{2}\right) - \frac{k_e L}{2}\cos\left(\frac{k_e L}{2}\right)\right] \tag{32}$$

The effective wavenumber $k_e$, factor $f$, and the Smith correction factor $S_c$ (error in the original work revealed through personal communication) is approximated by Eq. (33), Eq. (34), and Eq. (35), respectively.

$$k_e = |k cos\beta| \tag{33}$$

$$f = \sqrt{(1-kT)^2 + \left(\frac{A^2}{kB\alpha^3}\right)^2} \tag{34}$$

$$S_c = \exp(-kT) \tag{35}$$

The frequency response function for the vertical motion, $v(t)$, in a longitudinal position $x$ from the center of gravity is shown in Eq. (36). And the respective frequency response function for the acceleration is expressed by Eq. (37).

$$\phi_V = \sqrt{\phi_z^2 + x^2\phi_\theta^2} \tag{36}$$

$$\phi_g = \bar{\omega}^2\phi_V = \alpha^2 kg\phi_V \tag{37}$$

The relative vertical motion $r(x,t)$ with respect to the wave elevation $\xi(x,t)$ is

$$r(x,t) = v(t) - \xi(x,t) \tag{38}$$

The frequency response functions for the relative vertical motion with respect to the wave elevation in a longitudinal position $x$ from the center of gravity can be defined as

$$\phi_r = \sqrt{(\phi_z - cos\xi(x))^2 + \left(x\phi_\theta + sin\xi(x)\right)^2} \tag{39}$$

where

$$\xi(x) = \varepsilon_e + \varepsilon_r + k_e x \tag{40}$$

$$cos\varepsilon_e = \frac{1-kT}{f}; \quad sin\varepsilon_e = \frac{A^2}{kB\alpha^3 f} \tag{41}$$

$$cos\varepsilon_r = \eta(1 - 2kT\alpha^2); \quad sin\varepsilon_r = -\frac{A^2}{kB\alpha^2}\eta \tag{42}$$

The frequency response function for the relative vertical velocity is

$$\phi_{rv} = \varpi.\phi_r \tag{43}$$

The total relative vertical bow velocity can be found as

$$V_{rw} = \phi_{rv}\xi(x,t) \tag{44}$$

The response spectrum of relative motion and relative velocity for a wave height of $H_s$ is given by Eq. (45) and Eq. (46), respectively.

$$m_{0s} = \phi_r^2 \left(\frac{H_s}{2}\right)^2 \tag{45}$$

$$m_{2s} = \phi_{rv}^2 \left(\frac{H_s}{2}\right)^2 \tag{46}$$

*4.2.3.3 Relative Freeboard*

The effective relative freeboard is defined by (see Figure 4-4)

$$F_{br} = F_b + \phi_r \xi \tag{47}$$

where $F_b$ is the freeboard at the still water line, and $\xi$ is the amplitude of the wave. If $F_{br}$ is positive, the deck is above the water. If it is negative, the deck is below the water. In a ship-wave collision, the bow wave due to the forward movement of the ship can be considered negligible. The dynamic swell-up of rising water is more relevant to deck wetness (Sapone, 1990). Thus a water jet velocity due to dynamic pressure zones is introduced.

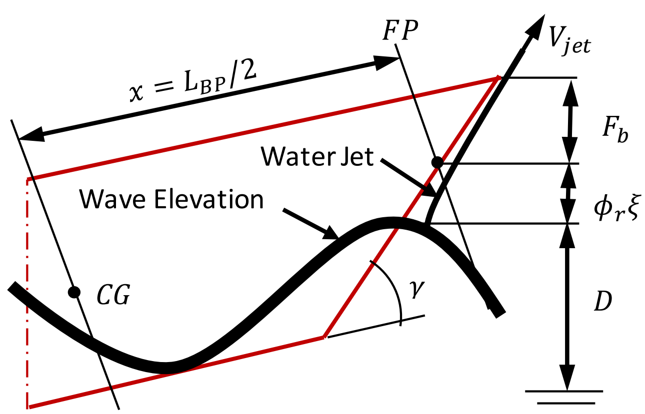


**FIGURE 4-4: SKETCH OF A SHIP-WAVE IMPACT TO DEFINE SPRAY THRESHOLD**

#### 4.2.3.4 *Water Jet Velocity*

The ship-wave collision produces a thin sheet of water jet as described in detail in 2.2.2 The ejection velocity of the jet due to wave impact on a vertical wall is estimated by (Cooker and Peregrine, 1995)

$$V_{jet} = -\frac{2V_{sw}}{\pi}\log\left(\frac{x}{D}\right) \tag{48}$$

where $D$ is the water depth. This equation says that the vertical velocity at the wall location $(x = 0)$ becomes infinite. Watanabe and Ingram (Watanabe and Ingram, 2015) proposed an alternative to avoid this singularity. The finite mean velocity may be found by explicitly integrating $V_{jet}$ over the jet thickness $h_1$ as expressed by Eq. (49). For an inclined wall, which is more applicable to a ship bow, Okamura (Okamura, 1993) extended Cooker's formula to Eq. (50).

$$V_{jet} = -\frac{2V_{sw}}{\pi}(\log(h_1) - \log(D) - 1) \tag{49}$$

$$V_{jet} = -V_{sw}\cot\frac{b+1}{2b}\pi\,, b > 1 \tag{50}$$

where $b = 90/\gamma$, and $\gamma$ is the stem angle as shown in Figure 4-4.

#### 4.2.3.5 *Defining Spray Frequency*

We assume that the spray frequency depends on the relative vertical velocity of a jet of water that has to overcome the relative local freeboard of a vessel to reach the deck. If the spray jet cannot reach the deck, it does not qualify as a spray event since it will not contribute to the icing process. Note that considering only the relative freeboard and not the relative velocity would result in green water frequency as discussed earlier. The spray frequency can be defined as

$$N_s = \frac{1}{2\pi}\sqrt{\frac{m_{2s}}{m_{0s}}}\ x\ P_{spray}\ [s^{-1}] \tag{51}$$

where $m_{0s}$ and $m_{2s}$ are variances of relative vertical motion and relative vertical velocity of the ship, respectively, and can be calculated by Eq. (44) and Eq. (45).

Assuming jet velocity and bow velocity as statistically independent events, the standard deviation of the combined velocity can be found as

$$S_{spray} = \sqrt{V_{jet}^2 + V_{rw}^2} \tag{52}$$

Assuming spray frequency is analogous to the whipping frequency, described by Jensen and Mansour (2003), that follows an exponential distribution, the probability of spray is given by

$$P_{spray} = exp\left(-\frac{V_{spray}}{S_{spray}}\right) \tag{53}$$

where the threshold velocity for the spray is defined in a similar way to Aalbers and Poen (2015) as

$$V_{spray} = \sqrt{2gF_{br}} \tag{54}$$

An interactive ship motion calculator has been developed using Python as shown in Figure 4-5, where all the methodologies explained in this section were implemented

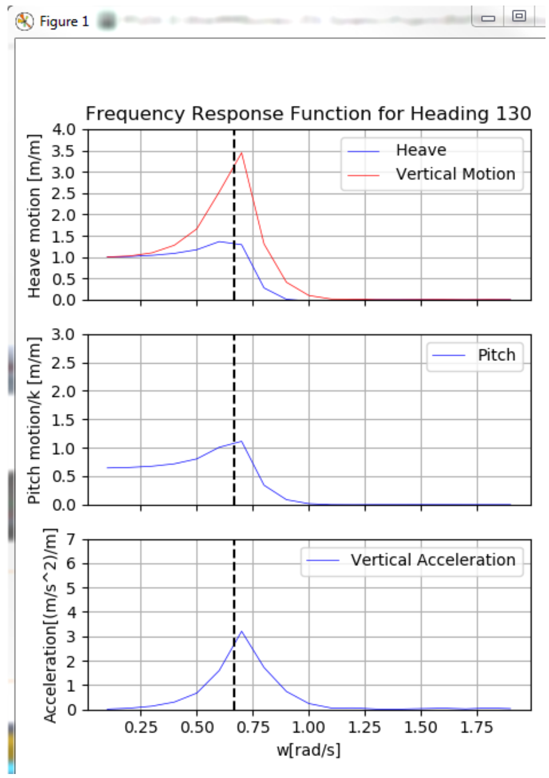


**FIGURE 4-5: PYTHON SHIP MOTION SOLVER**

## 4.3 Validation Studies

Among the three studies of full-scale spray generation available in the literature (Samuelsen et al., 2017), two of them were selected here due to their completeness. These include data from the 39m Russian fishing boat "MFV Narva"(Borisenkov and Pchelko, 1975), and the 115 m US Navy vessel "USCGC Midgett"(Ryerson, 1995). The third data set reported by Horjen et al. (1986) is missing ship particulars. Borisenkov and Pchelko (1975) did not report the raw data of their field survey. Some data were retrieved by Zakrzewski (1986b) from a soviet icing database. However, how the spray property was measured is unknown. Wave frequency was not measured during the field trial of Midgett (Ryerson, 1995). It was estimated from wave height using an empirical formula described by Horjen (2015). This may underestimate for low waves and overestimate for high waves as reported by Samuelsen et al. (2017). More realistic wave parameters may improve the prediction quality. The principal particulars of the vessels are given in Table 4-1.

TABLE 4-1: PRINCIPAL PARTICULARS OF NARVA AND MIDGETT

| Parameters | MFV Narva | USCGC Midgett |
|---|---|---|
| LOA (m) | 39.5 | 115 |
| Beam (m) | 7.3 | 12.80* |
| Depth (m) | 6.5 | 12.19 |
| Draft (m) | 3 (Zakrzewski et al., 1988) | 4.27 |
| Freeboard (m) | 3.5 (Samuelsen et al., 2017) | 7.92 |
| Stem angle (deg) | 70 | 40 |
| Displacement (tonne) | 462 (W.P. Zakrzewski, 1989) | 2703 |
| Ship speed (m/s) | 2.83 | 6~12 |
| Added Mass+ | 0.8 | 0.9 |

* The principal particulars of the vessel were not reported by Ryerson. The values are extracted from Thomas (Thomas, 1991) assuming they both referred to the same Midgett despite some ambiguities in the reported dimensions.

+ Since Midgett has a larger sectional area, we assumed a larger added mass for it than that of Narva.

### *4.3.1* Liquid Water Content (LWC)

Figure 4-6 shows the operating conditions and Figure 4-7 compares the results with Zakrzewski's (Zakrzewski, 1986b) model for the fishing boat Narva. The wave height was 3.09 m and the wave period was calculated from the wind speed by a fifth-degree polynomial regression (Zakrzewski, 1986b). The prediction is reasonable within a 1% error margin. The spray constant was derived from this field measurement, so a good prediction was expected.

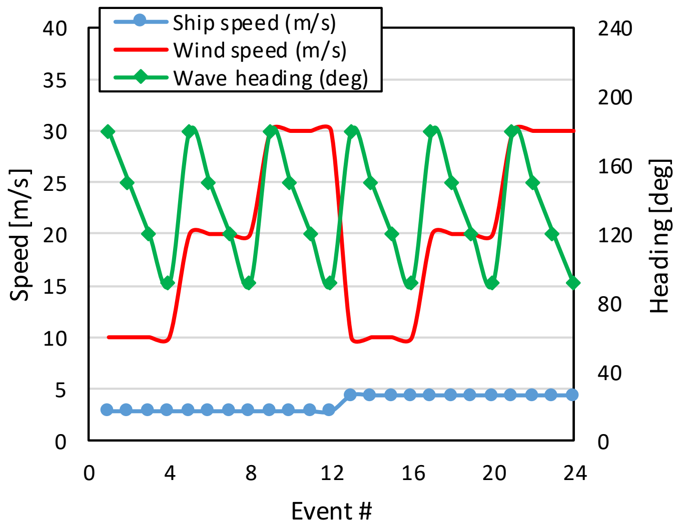


**FIGURE 4-6: OPERATING CONDITIONS OF MFV NARVA (ZAKRZEWSKI, 1986B)**

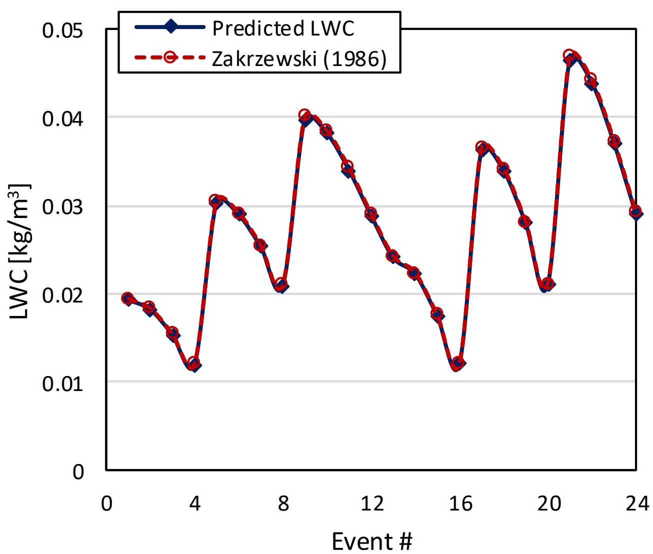


**FIGURE 4-7: LWC COMPARISON FOR MFV NARVA**

The same LWC expression was applied to predict LWC for the considerably larger vessel, Midgett. Among the 39 recorded spray events, some were identified as outliers as indicated by Ryerson

(1995) and were not considered in this study. There is a large variation in field data as can be seen from Figure 4-8 that summarizes the operating and oceanographic conditions of the respective spray events and their corresponding LWC.

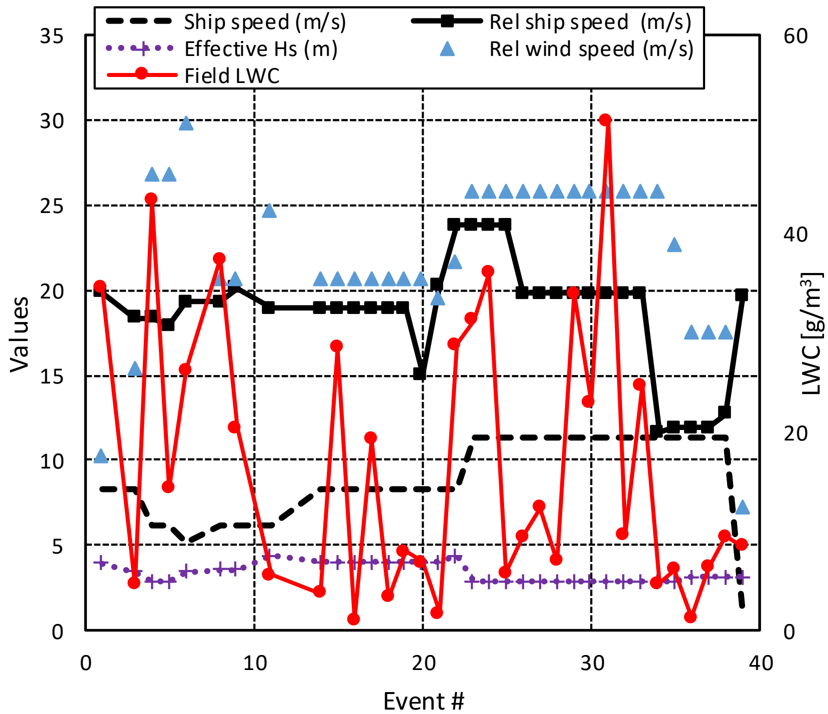


**FIGURE 4-8: OPERATING CONDITIONS OF USCGC MIDGETT (RYERSON, 1995)**

For the exact same conditions, the measured LWC varies up to 26 times (event# 15 vs 16). Drops were sampled from a very small volume in the stroboscopic camera when compared to the total size of the respective spray cloud. The spatial variation of drops within spray clouds was unknown and may be the cause of the variations in data (Ryerson, 1995). To eliminate the uncertainties in measurements, a statistical data analysis approach was applied in this study. The operational and environmental conditions for the first ten events were not consistent, hence not suitable for statistical analysis. The remaining data set were grouped into four speed-zones based on the ship speeds relative to waves. The average LWC values for each individual speed-zones were calculated and compared with our prediction model. The predicted LWC is reasonable and consistent with the field measurements as can be seen in Figure 4-9. It also shows how Zakrzewski's model under-predicts the LWC for the larger size vessel.

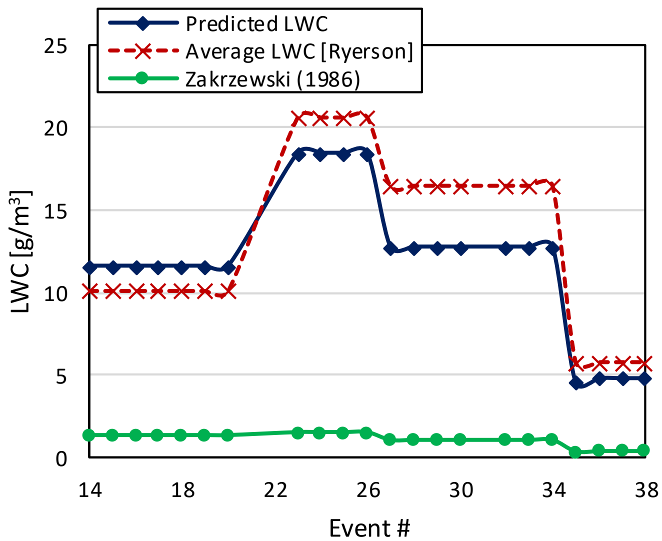


**FIGURE 4-9: COMPARISON OF LWC WITH FIELD DATA OF RYERSON (RYERSON, 1995)**

### 4.3.2 Spray Duration

In a similar fashion, predicted spray durations for Narva are compared with field measurements and existing empirical models in Figure 4-10. The results agree well with Zakrzewski's model for low wind speed. For higher wind speeds, Zakrzewski's model under-predicts due to the square term of the wind velocity as opined by Samuelsen et al. (2017). It is also worthy to note that Zakrzewski derived the empirical constant for a wind velocity of 10-12 m/s, which is the likely reason for good agreement only in this region. The average value of the predicted duration is comparable with the field measurements shown by the black dotted line. On a close examination of the saw-tooth pattern of predicted spray duration in Figure 4-10, it was revealed that spray duration is correlated to LWC (see Figure 4-11). The more LWC an event produces, the longer the spray duration. This also explains why Ryerson found a somewhat longer spray duration for the 115 m cutter than that of a 35-m trawler (Ryerson, 1995).

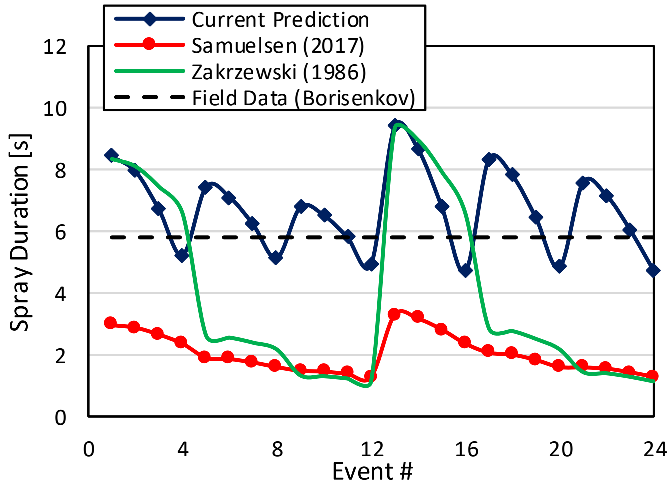


**FIGURE 4-10: COMPARISON OF SPRAY DURATIONS FOR MFV NARVA**

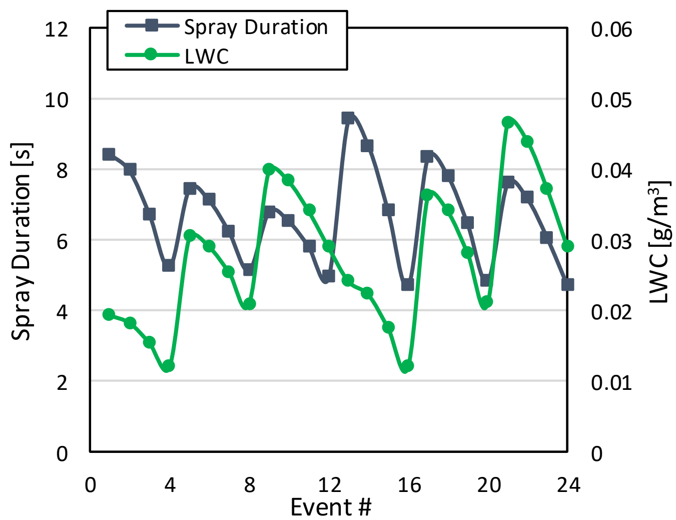


**FIGURE 4-11: SPRAY DURATION VS LWC**

Figure 4-12 compares spray durations for Midgett. In general, the predictions are reasonable and consistent with the field measurements. For the highest (event# 23 to 26) and lowest relative speed-zones (event# 35 to 38), both Lozowski's (Lozowski et al., 2000) and Samuelsen's

(Samuelsen et al., 2017) model show large prediction errors. For the remaining speed zones, the present predictions are in reasonable agreement with the other models.

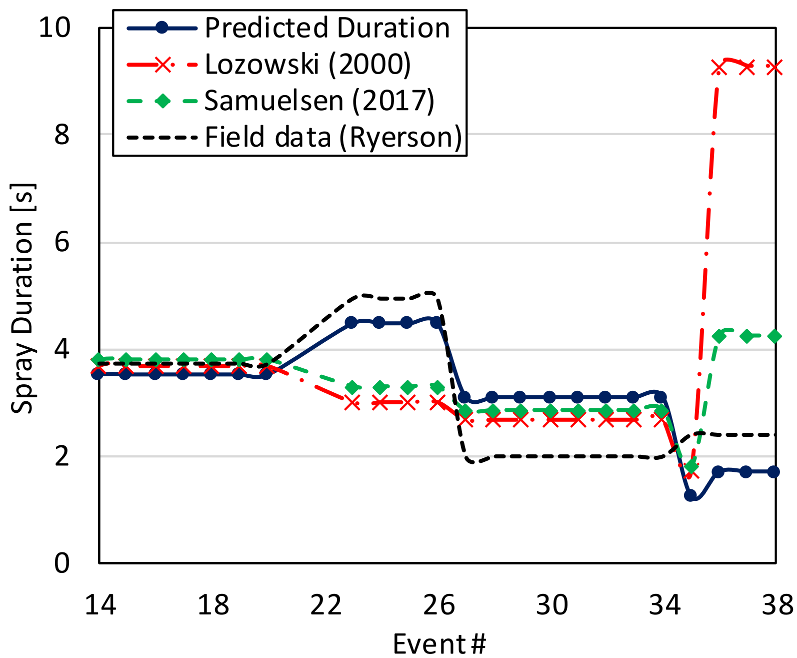


**FIGURE 4-12: COMPARISON OF SPRAY DURATIONS FOR USCGC MIDGETT**

### 4.3.3 Spray Frequency

As stated earlier, there are only a few publications found in the literature describing spray frequencies. Among them, only Panov's field data (Panov, 1976) contains all the necessary elements (ship particulars, sea states, and measured values for spray frequencies) for the current model to apply. These data were retrieved by Zakrzewski (1986a) from soviet icing reports. The USCGC Midgett data was also considered and compared with Lozowski's formula (Eq. (8)). In both cases, ship speed was set to Vs = 6 knots, the heading angle = 125°, and the wave height was 6 meters as reported by Zakrzewski (1986a).

Figure 4-13 compares the findings with the field measurements (data given in Table 3-4) along with Panov's empirical formula (Eq. (5)) for various wavelengths. Overall, good agreement with the field observations can be seen except for the steepest 10 m wave, which shows a 20% error. However, it is better than Zakrzewski's prediction.

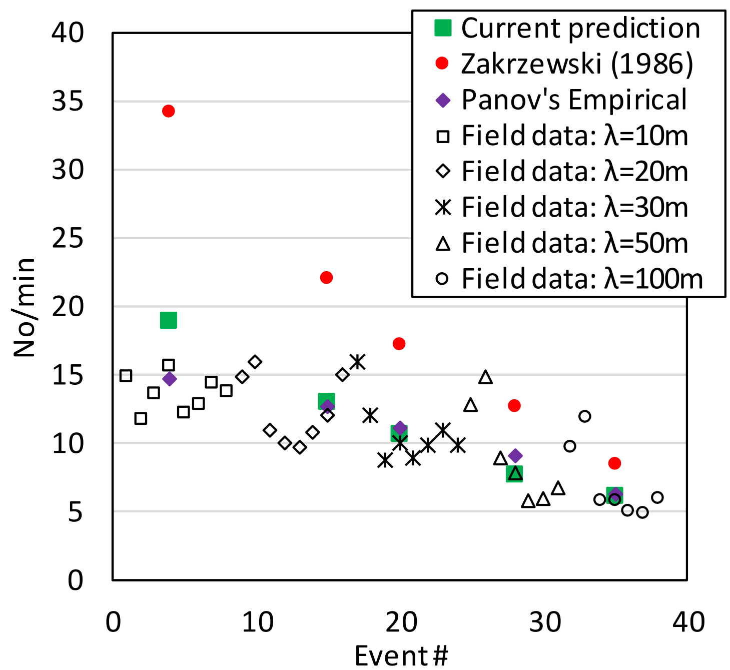


**FIGURE 4-13: COMPARISON OF SPRAY FREQUENCIES FOR MFV NARVA WITH FIELD MEASUREMENT (PANOV, 1976).**

Figure 4-14 compares the spray periods for both Narva and Midgett. Lozowski speculated spray period for Midgett would be four times the spray period of a fishing boat like Narva. The figure shows that it depends on the wave frequencies and can vary from two to four times. Ryerson (1995), however, did not report any spray frequency for Midgett to compare.

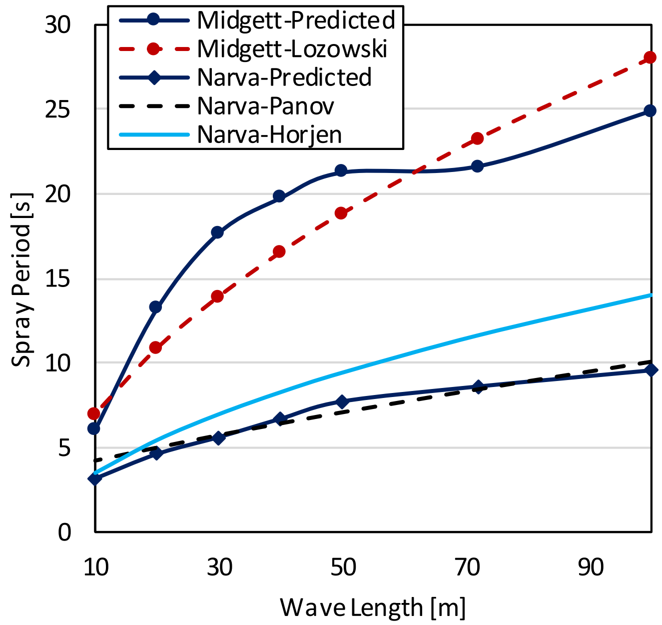


FIGURE 4-14: COMPARISON OF SPRAY FREQUENCIES FOR USCGC MIDGETT AND MFV NARVA

## 4.4 Alternative LWC

An alternative theoretical method to estimate spray water due to a ship-wave collision is proposed in this section. The sheet velocity was modeled by the pressure-impulse theory of Cooker and Peregrine (1995) and droplet distributions were modeled by using Watanabe and Ingram (2015) model. The spray formation depends strongly on whether the sea wall is impacted by a pre-breaking, breaking, or broken wave (Watanabe and Ingram, 2015). The mechanism for the formation of sea sprays through the splash-up event is likely to be more complicated than that of the nozzle jets since the vortices produced under breaking wave surfaces cause significant surface deformations through the surface–vorticity interactions. Bodaghkhani et al. (2018) and Lozowski et al. (2000) used linear wave theory to predict jet velocity. Watanabe and Ingram (2015) showed how much it underestimates (see Figure 4-15).

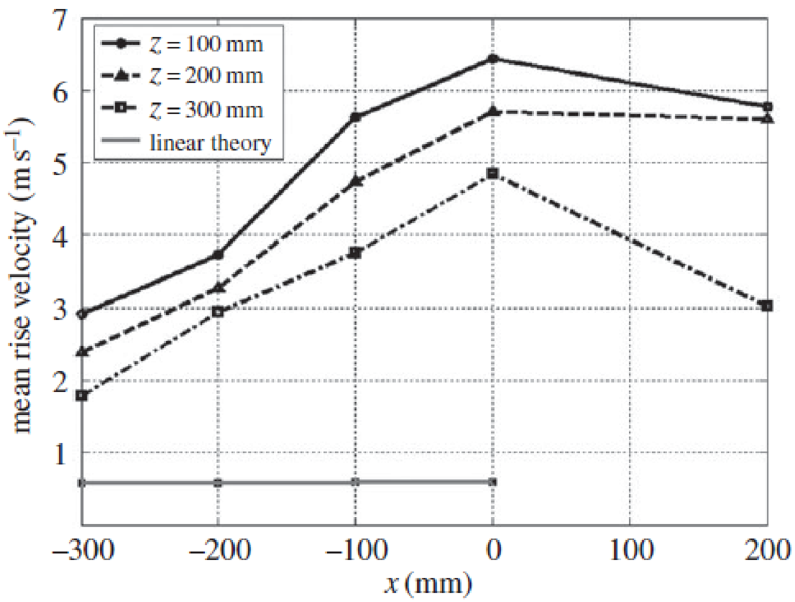


**FIGURE 4-15: ENSEMBLE MEAN RISE VELOCITIES OF THE JETS AND THEORETICAL MAXIMUM VERTICAL VELOCITY OF THE STANDING WAVE (WATANABE AND INGRAM, 2015)**

The ejection velocity of the jet due to wave impact on a vertical wall was estimated by Cooker and Peregrine (1995) as described in Section 4.2.3.4 . The water sheet thickness and ligament diameter based on the jet velocity can be defined as (Dombrowski and Johns, 1963), respectively

$$h = \mathrm{kF}^{\frac{2}{3}}\left(\frac{9f^2\sigma\rho_L k}{2\rho_a^2 U^4}\right)^{-\frac{1}{3}} \tag{55}$$

$$d_L = 0.9614\left[\frac{K^2\sigma^2}{\rho_a\rho_L U^4}\right]^{\frac{1}{6}}\left[1 + 2.60\mu\sqrt[3]{\left(\frac{K\rho^4 U^7}{72\rho_L^2\sigma^5}\right)}\right]^{\frac{1}{5}} \tag{56}$$

where, $K$ = 0.05, is the spray parameter, $f$ =12, F =1 for inviscid flow, σ is the surface tension of the water, $\rho_a$ and $\rho_L$ are the density of air and water, respectively.

The probability distribution of the droplets can be defined after (Watanabe and Ingram, 2016) as follows:

$$\mathrm{P}\ln(x) = \frac{1}{x\lambda\sqrt{2\pi}} \exp\left(\frac{-(\ln x - \mu)^2}{2\lambda^2}\right) \tag{57}$$

$$\lambda = 0.0074t^* + 0.73 \tag{58}$$

$$\mu = -0.0068t^* - 0.24 \tag{59}$$

$$t^* = \frac{t_i}{\tau_r} \tag{60}$$

where $x = \frac{d}{D}$, $t_i$ is the arrival time of the jet at the vertical level z from the time to start the flip-through and $\tau_r$ is the capillary time for the rim deformation

$$\tau_r = \sqrt{\rho a_i^3/\gamma} \tag{61}$$

where $a_i$ is the rim diameter, which is assumed to be equal to the ligament diameter $d_L$.

The total number of droplets, and therefore the amount of spray water is related to the drop radius $r$ by the following expressions (Watanabe and Ingram, 2016):

$$N_e \propto r^{-\frac{5}{2}} \tag{62}$$
$$N_s \propto r^{-2}$$

where $N_e$ and $N_s$ are the number of droplets at the early break-up stage and at the fully fragmented state, respectively. For MFV Narva operating at 2.83m/s in head sea condition, the calculated value for LWC was found to be 0.0326 kg/m$^3$. The size distributions at various vertical heights are shown in Figure 4-16. It should be noted that this method is only applicable to vertical walls at head sea conditions.

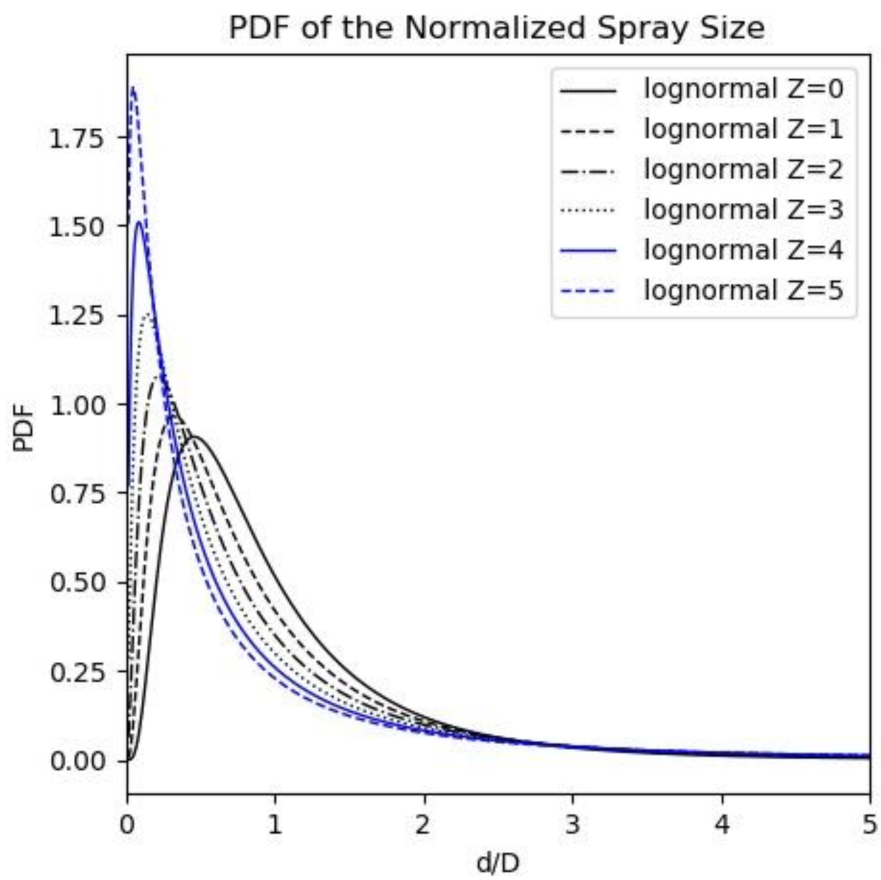


**FIGURE 4-16: DROPLET SIZE DISTRIBUTION AT VARIOUS HEIGHTS (Z)**

## 4.5 Discussion

The energy-based model proposed here is a semi-empirical model that takes into account ship particulars as well as sea state and is fast in computation and simple to apply. More field data is, however, desirable to tune the spray constant precisely. The model is also applicable to special situations. For example, if there is no ship motion, there is still some possibility of spray generation due to wave splashing and static swell-up of water, which can occur in front of the bow (Aalbers and Poen, 2015; Bhattacharyya, 1978). For a zero forward speed in waves (Figure 4-17), this model is consistent with Zakrzeski's model. The limitation of Zakrzewski's model, however, is evident in Figure 4-18 which shows LWC for the same ship speed, wind speed, and sea state at different heading angles (from 180 degrees to 90 degrees) is increasing with larger ship sizes. For larger size vessels, even though it produces a larger amount of spray for a single spray event, the frequency of spray generation would be lower than that of a smaller vessel and therefore, the accumulated spray flux for a given period should be lower than a smaller size vessel. Figure 4-19 depicts how increasing ship size increases the duration, while other models do not reflect any sensitivity. Validation with model test data was not attempted since the comparison may not be valid due to unknown scale effects (Lebiedzlnski and Thomas, 1993). Measurements without appropriate scaling may give an unrealistic amount of water, larger droplet size, and incorrect droplet concentration (Dehghani et al., 2016b).

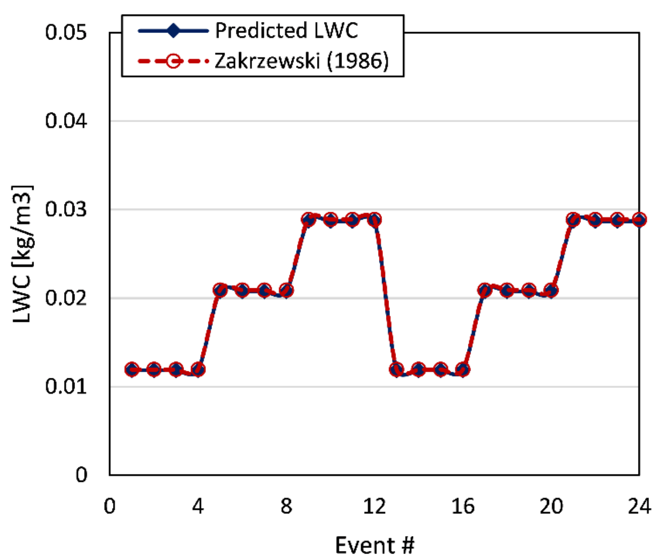


**FIGURE 4-17: LWC AT ZERO FORWARD SPEED IN WAVES**

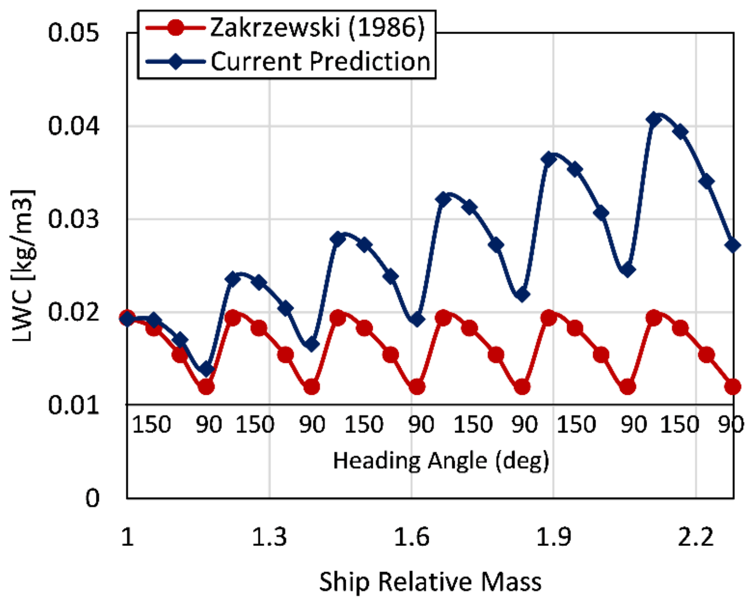


**FIGURE 4-18: EFFECT OF SHIP SIZE ON LWC AT DIFFERENT HEADINGS**

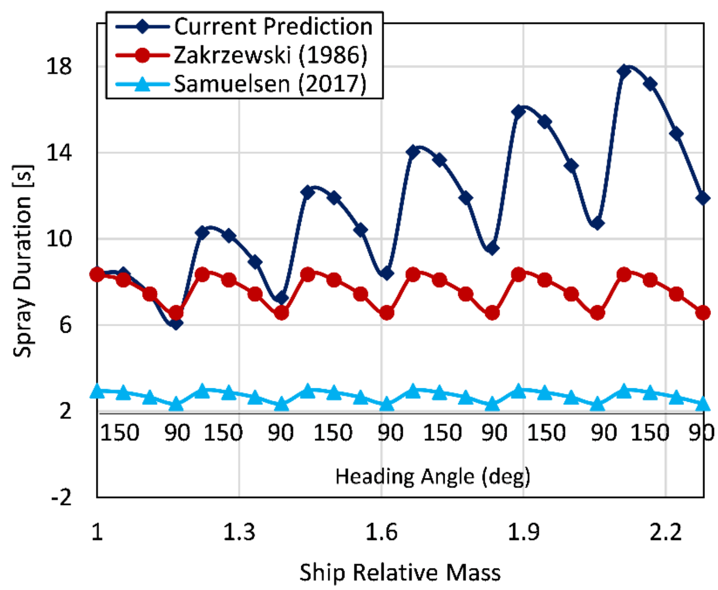


**FIGURE 4-19: EFFECT OF SHIP SIZE ON SPRAY DURATION AT DIFFERENT HEADINGS**

Although there are a few discrepancies noted in Figure 4-14, it was found that Lozowski's hypothetical assumption for the spray frequency/period of the larger size vessel Midgett is comparable to the theoretical prediction presented here. However, the limitation of Lozowski's formula is revealed in Figure 4-20 which shows a vessel with a smaller freeboard tends to get spray water more frequently. In this particular case, it is 9-18% more frequent, whereas the empirical formulas are insensitive to hull geometry.

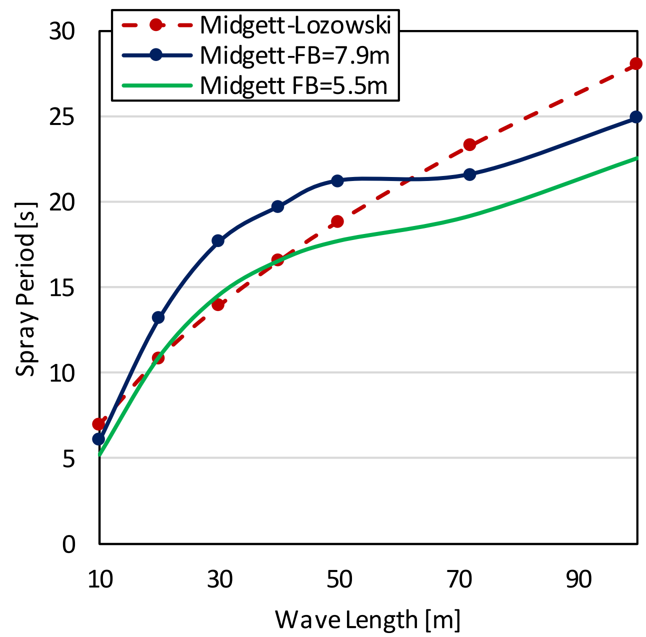


**FIGURE 4-20: EFFECT OF FREEBOARD ON SPRAY FREQUENCY**

Although the current model incorporates ship parameters, it also has some limitations. Bow motion out of phase with wave motion will produce the largest spray. When the ship's natural pitching and heaving periods are in near synchronization with the wave frequencies, there will be the greatest likelihood of slamming and severe spray events. The current model does not take that into account. The phase difference between the ship motion and wave motion also affects spray frequency. Especially in irregular waves, when in-phase, the ship would rise on a crest, and sink in a trough, and not create a spray for many wave encounters. When out-of-phase, it would plunge into each wave and create spray events for nearly every wave. During the gradual shifts from the in-phase toward the out-of-phase over time, it may produce little or no spray. This clustering of spray events, from frequent to infrequent, affects the icing process (Ryerson, 2013) and needs to be considered. The randomness of the wave phase may be examined in time domain in future studies. Hull girder natural frequency and vibration due to slamming may also contribute to the spray, which was not considered in this study.

# Chapter 5 :

# Numerical Model

## 5.1 Introduction

Although theoretical models give a quick estimate of the spray properties, they often do not model all aspects of the spray physics. Numerical simulation can offer an integrated approach where multiple physical elements can be modeled properly and overcome many of the limitations of scaled model experiments and field measurements. Theoretical and empirical models together with numerical models can give a broader understanding of the dynamic nature of spray physics.

The multi-scale nature of this problem was broken into two-part simulations. In the first part, simulations of wave generated spray due to a moving ship was developed. The distribution of the generated spray and the droplet trajectories were simulated in the second part. The chapter begins with a detailed description of the SPH method. Then, the selection of computer hardware to run the simulations is discussed. The development of the two-part simulations is explained sequentially in two sections.

## 5.2 SPH Method

### 5.2.1 Governing Equations

SPH is a mesh-less, fully Lagrangian method (Gingold and Monaghan, 1977), where the grids are completely abandoned and the continuum is represented by a set of material points known as particles. Particles are geometrical positions in the continuum that carry physical properties such as volume, mass, momentum, temperature, concentration, or other hydrodynamic properties (Shadloo et al., 2016). The differential form of the Navier-Stokes equations is transformed into particle summations by discrete approximations. The continuity and momentum conservation equations for weakly compressible fluid are described by

$$\frac{d\rho}{dt} = -\rho\nabla.u \tag{63}$$

$$\frac{du}{dt} = -\frac{\nabla P}{\rho} + g + \nu_0\nabla^2 u + \frac{1}{\rho}\nabla.\vec{\tau} \tag{64}$$

where $\rho$ is the fluid density, $u$ is the velocity vector, $P$ is the pressure, $g$ is the gravitational acceleration, $\nu_0$ is the laminar kinematic viscosity, and $\vec{\tau}$ is the large eddy simulation Sub-Particle Scale (SPS) stress tensor (Dalrymple and Rogers, 2006). The pressure P can be directly computed from the equation of state (Batchelor, 1967; Monaghan et al., 1999) for single and multi-phase flow respectively as

$$P(\rho) = B\left[\left(\frac{\rho}{\rho_0}\right)^{\gamma} - 1\right] \tag{65}$$

$$P(\rho) = B\left[\left(\frac{\rho}{\rho_0}\right)^{\gamma} - 1\right] + X - a\rho^2 \tag{66}$$

where the coefficient $B = C_S^2\rho_0/\gamma$ is constant for each phase, $C_S$ is the speed of sound, $\rho_0$ is the initial density of the fluid, and $\gamma$ is the isentropic expansion factor. The inclusion of the -1 term in the equation of state allows automatic capturing of free surface behavior and fragmentation (Pereira et al., 2018). The term X signifies a constant background pressure and the term $a\rho^2$ prevents the dispersion of the air into the water and the subsequent fragmentation of the interface (Mokos et al., 2015), where $a$ is a cohesion factor defined as

$$a = 1.5g(\rho_{0w}/\rho_{oa}^2)L \tag{67}$$

where $\rho_{0w}$ and $\rho_{0a}$ are the initial densities of the water and air respectively and $L$ is the characteristic length scale of the problem being modeled.

### 5.2.2 Discretization of Governing Equations

The derivatives of the governing equations are estimated at any point in space using a kernel approximation, which is analogous to finite difference and finite volume discretization techniques in mesh-based CFD. The principle is to approximate any function F by the integral approximation:

$$\langle F(r) \rangle = \int_{\Omega} F(r')W(r - r', h)dr' \tag{68}$$

where $W$ is the kernel function, $r$ is the position vector, $h$ is the smoothing length that is the influencing area of the kernel function, Ω is the interpolation domain, and the symbol ⟨ ⟩ denotes an approximation.

In discrete SPH, equation (68) is further approximated using the interpolant formula and called particle approximation (Z.-B. Wang et al., 2016).

$$\langle F(r_i) \rangle = \sum_{j=1}^{N} F(r_j)W(r_i - r_j, h)\frac{m_j}{\rho_j} \tag{69}$$

where $N$ is the total number of particles in the calculation region.

In SPH notation, equation (63) and (64) can be discretized respectively after (Dalrymple and Rogers (2006) as

$$\langle \frac{d\rho_i}{dt} \rangle = \rho_i \sum_j \left[ (u_i - u_j).\nabla_i W_{ij} \frac{m_j}{\rho_j} \right] + \mathfrak{D}_t \tag{70}$$

$$\langle\frac{du_i}{dt}\rangle = -\sum_j m_j\left(\frac{P_i + P_j}{\rho_i.\rho_j}\right)\nabla_i W_{ij} + g$$
$$+\sum_j m_j\left(\frac{4\nu_0 r_{ij}.\nabla_i W_{ij}}{(\rho_i+\rho_j)(r_{ij}^2+\eta^2)}\right)u_{ij} \quad (71)$$
$$+\sum_j m_i\left(\frac{\vec{\tau}_{ab}^{\,j}}{{\rho_j}^2}+\frac{\vec{\tau}_{ab}^{\,i}}{{\rho_i}^2}\right)\nabla_i W_{ij}$$

where t is time, r is particle position, u is velocity, P is pressure, ρ is density, m mass, g = (0, 0, -9.81) $ms^{-2}$ is the gravitational acceleration, $\nu_0$ is the laminar kinematic viscosity, $\vec{\tau}$ is the SPS stress tensor, $\eta^2 = 0.01\,h^2$, and $W_{ij}$ is the kernel function that depends on the distance between particles i and j (Altomare et al., 2017).

The density diffusion term $\mathfrak{D}_t$ modified by Fourtakas et al. (2020) with a recommended coefficient of 0.1 (Altomare et al., 2020; Kanehira et al., 2020) was applied to improve the pressure field in the wave basin. The stability, accuracy, and speed of SPH simulation depend on the choice of the smoothing kernel distribution as well as the smoothing length (Shadloo et al., 2016). In this work, the Quintic (Wendland, 1995) kernel was used. Wendland kernel circumvents clustering of neighboring particles due to the onset of the tensile instability (Zha et al., 2021) and is widely used (Altomare et al., 2020; Kanehira et al., 2020; Kawamura et al., 2016). It is expressed as:

$$W(r,h) = \frac{7}{4\pi h^2}\left(1-\frac{q}{2}\right)^4(2q+1) \quad 0 \le q \le 2 \quad (72)$$

where $q = \frac{r}{h}$, $r$ is the distance between any two given particles i and j, and $h$ is the smoothing length.

### 5.2.3 Multi-Phase SPH Method

For multi-phase SPH, momentums for water phase and air phase are discretized respectively as:

$$\langle\frac{du_i}{dt}\rangle = -\sum_j m_j\left(\frac{P_i + P_j}{\rho_i.\rho_j} + \Pi_{ij}\right)\nabla_i W_{ij} + g \tag{73}$$

$$\langle\frac{du_i}{dt}\rangle = -\sum m_j\left(\frac{P_i + P_j}{\rho_i.\rho_j} + \Pi_{ij}\right)\nabla_i W_{ij} - 2a\rho_a^2\sum_j\frac{m_j}{\rho_j}\nabla_i W_{ij} + g \tag{74}$$

where t is time, u is velocity, P is pressure, ρ is density, m mass, g = (0, 0, -9.81) $ms^{-2}$ is the gravitational acceleration, and $W_{ij}$ is the kernel function that depends on the distance between particles i and j (Altomare et al., 2017). The artificial viscosity term $\Pi_{ij}$ is used to resolve numerical instability and is given by:

$$\Pi_{ij} = \begin{cases}\frac{-\alpha\overline{c_{\iota J}}\mu_{ij}}{\overline{\rho_{\iota J}}} & u_{ij}.r_{ij} < 0\\ 0 & u_{ij}.r_{ij} > 0\end{cases} \tag{75}$$

where α is a coefficient that needs to be tuned in order to introduce realistic dissipation (Altomare et al., 2015), $\overline{c_{\iota J}} = \frac{c_i + c_j}{2}$ is the mean speed of sound, $\mu_{ij}$ is the kinematic viscosity given by

$$\mu_{ij} = \frac{h.u_{ij}.r_{ij}}{r_{ij}^2 + 0.01h^2} \tag{76}$$

where $r_{ij} = (r_i - r_j)$ and $u_{ij} = (u_i - u_j)$ are the particle position and velocity respectively and $h$ is the smoothing length.

## 5.3 Computing Hardware: CPU vs GPU

### 5.3.1 Introduction

Most practical CFD simulations are computationally expensive. This simulation time can be reduced in two ways. The most common approach is to use high-performance computing (HPC) on supercomputers consisting of multiple CPU cores. Most engineering firms either use their own cluster, which typically consists of 8 to 32 cores, or lease a massive cluster through cloud computing. The total cost of ownership (TCO) of a cluster is relatively high and maintenance cost is another burden.

Alternatively, the simulation can be accelerated cheaply by using novel computing architectures such as General Purpose Computing on Graphical Processing Units (GPGPUs) (Crespo et al., 2011), commonly referred to as GPU. Figure 5-1 compares GPU architecture with traditional CPU. GPU is a powerful parallel programming model where graphics cards are used as an execution device that contains a large number of high-performance processors. Originated from the video gaming industry, it is now gaining interest in engineering applications because of recently accessible programming interfaces namely Compute Unified Device Architecture (CUDA).

| **CPU** | **GPU** |
|---|---|
|  |  |

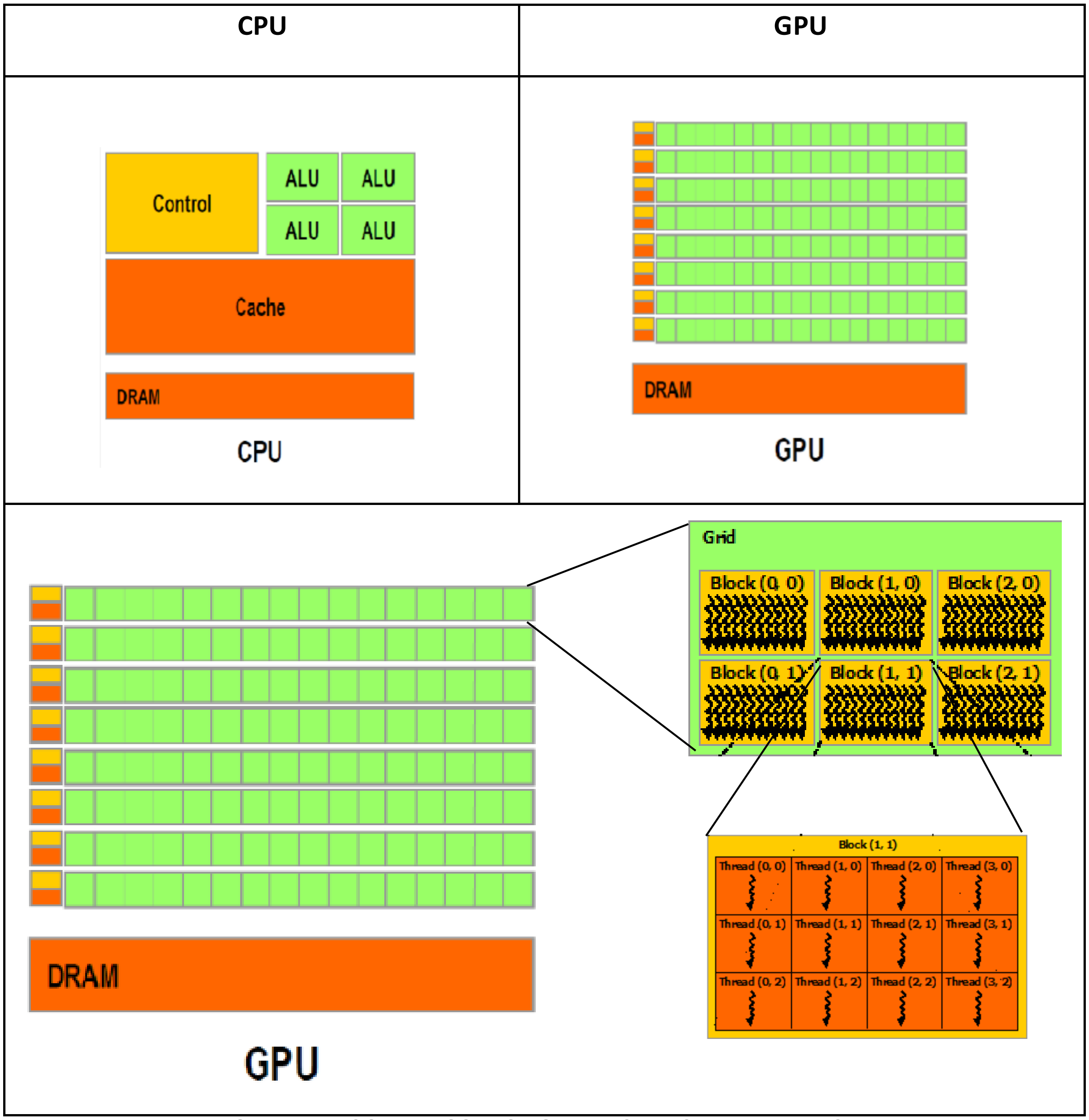


FIGURE 5-1: COMPARISON OF GPU ARCHITECTURE WITH CPU

CUDA is required to communicate with the GPU. It uses a standard C programming language to implement algorithms on the GPU, without the programmer having any expertise in graphics programming, by using OpenGL, DirectX, and shading language (Normore, 2010). A good overview of GPU and its architecture, compared to CPU is given by Normore (2010). The multi-threading capability makes the GPU computationally very efficient. The lower cost and ease of maintenance of GPU in comparison with large multi-core HPC systems is another attractive feature. The increase in computational power and lower cost ratio of GPU are increasing faster than that of traditional CPUs (Alawneh et al., 2016).

GPU implementation of CFD codes has been studied by many researchers. Both mesh-less CFD (Crespo et al., 2011; Osborne, 2009) and mesh-based CFD (Ansys Inc., 2014; Jespersen, 2010, 2009; Liu et al., 2016; Normore, 2010) have been studied. SPH-based CFD is a Lagrangian mesh-less approach that does not require a computational mesh. It simulates fluid by simulating particles. Whereas mesh-based CFD simulates the fluid continuum through discretization of that continuum (Normore, 2010). The underlying algorithms of different CFD codes and their implementation on GPU, therefore, require different techniques to optimize the performance.

To the author's best knowledge, a CUDA based GPU application of a fluid simulation was first demonstrated by Osborne (2009). He implemented SPH based CFD on various types of GPU configurations. Crespo et al. (2011) accelerated an SPH based CFD simulation using a GPU parallelization technique. They compared four different GPU cards: GTX 260, TESLA M1060, GTX 285, and GTX480 and achieved speedups of up to two orders of magnitude over a single core CPU. Jespersen of NASA (Jespersen, 2010, 2009) also recognized GPU as an accelerating tool for CFD simulation. He ran CFD code OVERFLOW on a workstation with GTX8800 and Tesla C1060 GPU card and compared the performance against a single CPU. He achieved a speedup of 40%. Liu et al. (2016) conducted OpenFOAM simulations of a lid-driven cavity flow where they optimize the computational load by proposing a hybrid CPU+GPU solution method. Commercial CFD like ANSYS Fluent (Ansys Inc., 2014) has started using GPU where they demonstrated a significant speedup of ANSYS simulations.

Some researchers implemented only parts of the mesh-based CFD algorithms on the GPU device. Normore (2010) developed algorithms to implement SIMPLE (Semi-Implicit Method for Pressure-Linked Equations) and PISO (pressure-implicit with splitting of operators) algorithms on GPUs and compared the performance of different NVIDIA and Tesla GPUs. He obtained a speedup of up to 650 times per time step compared to a single core CPU. Xiang et al. (2017) also implemented the SIMPLE algorithm on a GPU and simulated a lid-driven cavity flow, where they obtained a speedup of up to 78 times compared to a sequential CPU. Alawneh et al. (2016) demonstrated a significant reduction of simulation time in several ice engineering applications using GPU. There are other non-scientific applications of fluid simulation on GPU with applications in video games and visual effects, which are not considered in this paper.

It can be noted that most authors compared the performance of a GPU over a single core CPU, where in reality, a multi-core CPU is typically used for CFD simulation. In this study, the performance of a GPU is compared against a more practical number of CPU cores to demonstrate a commercial benefit of using GPU. The open-source CFD code, DualSPHysics (Crespo et al., 2015) is used for simulation purposes. Two different scenarios are simulated on a 16 core CPU and a single GPU card. They are discussed in the following sections.

In this study, two scenarios were simulated to compare the performance of a single GPU card. The first case study generates a 2D regular wave of 0.1 m height and 1.3 s period using a piston-type wave maker. The particle numbers vary from 51,000 to ~320,000 to give a finer resolution of the domain. The second study deals with a more realistic and practical CFD simulation, where a free-floating 3D fishing boat on a regular wave of 3.09 m high and 6.75 s period is simulated. The principal particulars of the fishing vessel are given in Table 5-1. The 3D model is shown in

Figure 5-2, while Figure 5-3 shows the particle representation of the vessel. The total particle number varies from ~50,000 to ~0.75 million. The wave is generated with a piston-type wave maker.

TABLE 5-1: FISHING BOAT PRINCIPAL PARTICULARS

| Item | Value | Unit |
|---|---|---|
| LOA | 19.8 | m |
| LBP | 18.17 | m |
| Breadth | 7.9248 | m |
| Depth | 4.1656 | m |
| Lightship Weight | 115,107.954 | kg |
| Lightship Draft | 2.456 | m |

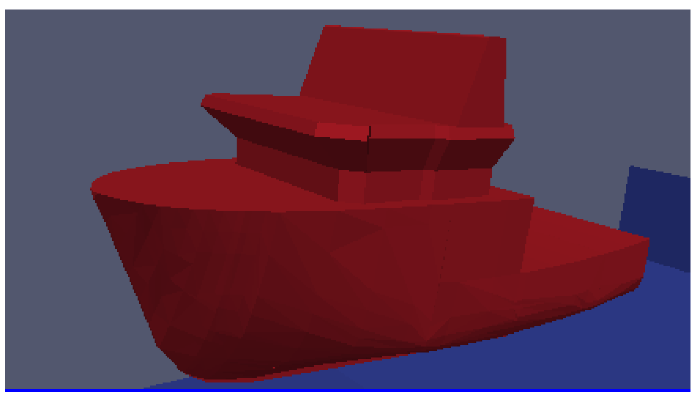

FIGURE 5-2: 3D MODEL OF THE FISHING BOAT

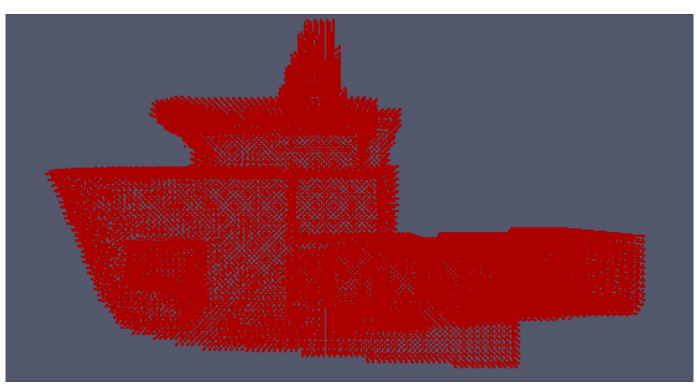

FIGURE 5-3: PARTICLE REPRESENTATION OF THE VESSEL

The test simulations are presented for 10 seconds of physical time for the 2D case and 14 seconds for the 3D case. The performance of the GPU is measured for various resolutions of the domain by running the same simulations for various numbers of particles. The length of the simulation was restricted by the available computing resources. The ACENET server of Compute Canada (www.computecanada.ca) was used to run the simulations on the CPU cluster. The study focuses on the acceleration of simulation time only, and not the simulation results. The results of the violent ship-wave interactions are covered in Section 5.4.

**BOUNDARY CONDITION**

A moving wall boundary condition was imposed on the piston-type wavemaker. An open periodic boundary condition was applied instead of using lateral solid walls to avoid any friction and any small reflection that might occur in the direction perpendicular to the incoming wave direction (Crespo et al., 2015). The floating ship is modeled using 'dynamic' boundary particles, which create a repulsive force to prevent fluid particles from penetrating the ship (Crespo et al., 2011).

The active wave absorption mechanism was not available in the version of the code that was used here. Therefore, the simulation length is set in such a way as to avoid any wave reflection. However, a passive wave absorber is used by creating a dissipative beach as shown in Figure 5-4. The scope of the work is not to simulate a long time series of waves but to compare the performance of the computational devices for a short period of time, hence justifies the simulation setup.

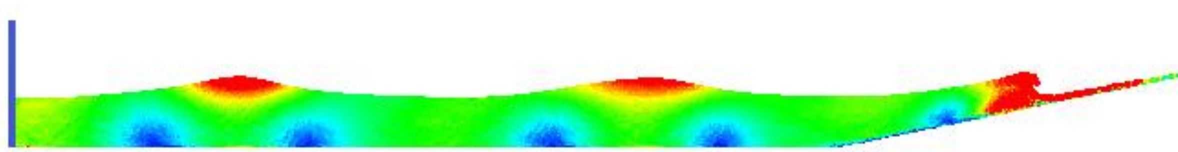

FIGURE 5-4: DISSIPATIVE BEACH PROFILE. COLOR INDICATES FLUID VELOCITY.

### COMPUTING RESOURCES

A 16-core Quad-Core AMD Opteron 2.7 GHz CPU with 16 GB memory was used since it is a typical server setup in most commercial applications (Henkel and Treiber, 2015). The specifications of the GPU are given in Table 5-2. For the current comparison, we used GTX Titan Black. Tesla K80 and Tesla T4 were used later for the simulations presented in Section 5.4 and Section 5.5. The computer containing the GPU card was an Intel ®Xeon® CPU E5-2620 v2 @ 2.10 GHz (2 processors).

TABLE 5-2: SPECIFICATIONS OF THE GPUS

| | Properties | NVIDIA GTX Titan Black | NVIDIA Tesla K80 | NVIDIA Tesla T4 |
|---|---|---|---|---|
| ENGINE SPECS | CUDA Core | 2880 | 2496 | 2560 + turing tensor core: 320 |
| | Clock Rate (GHz) | 1.07 | 1.2 | 1.55 |
| | Compute Capability | 3.5 | 3.7 | 7.5 |
| MEMORY SPECS | Memory Speed | 7.0 Gbps | | |
| | Standard Memory Config. | 6 GB | 12 GB | 16 GB |
| | Memory Interface | GDDR5 | GDDR5 | GDDR6 |
| | Memory Bandwidth | 336 GB/sec | 240.6 GB/sec | 320 GB/sec |

### SIMULATION RESULTS

The elevation of the simulated 2D regular wave is shown in Figure 5-5. It can be seen that the GPU simulation produces the same results as that of the CPU. The numerical results are found to be reasonably accurate compared to the theoretical value as shown in Figure 5-5. Simulations at a different resolution of the domain show a close agreement between theoretical and numerical results as depicted in Figure 5-6.

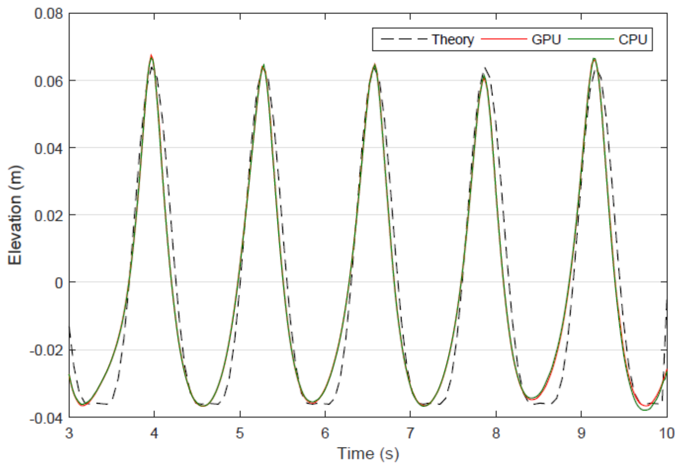


**Figure 5-5: Wave elevation at x=2m**

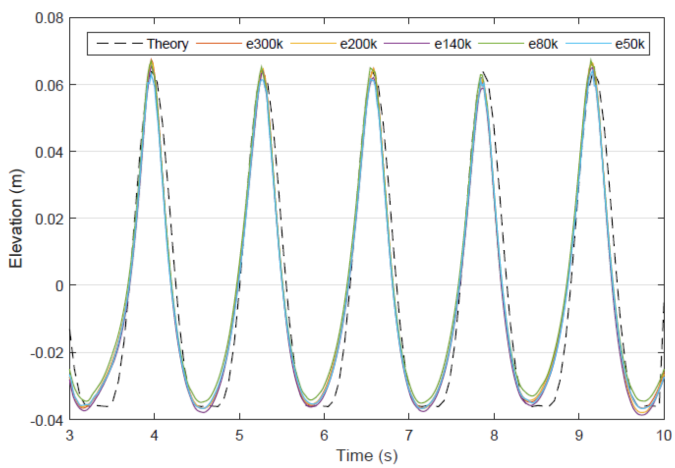


**FIGURE 5-6: CONVERGENCE OF WAVE ELEVATIONS FOR DIFFERENT PARTICLE NUMBERS**

In the second case study, the six degrees of freedom (DOF) motion of the fishing boat is computed from the 3D simulation of ship-wave interactions. Figure 5-7 shows the time series of the rotational motions, while the linear motions of the floating ship are shown in Figure 5-8. The dotted lines in both figures show the results from the CPU executions. It can be seen from the figures that the motions are accurately reproduced by the GPU simulations.

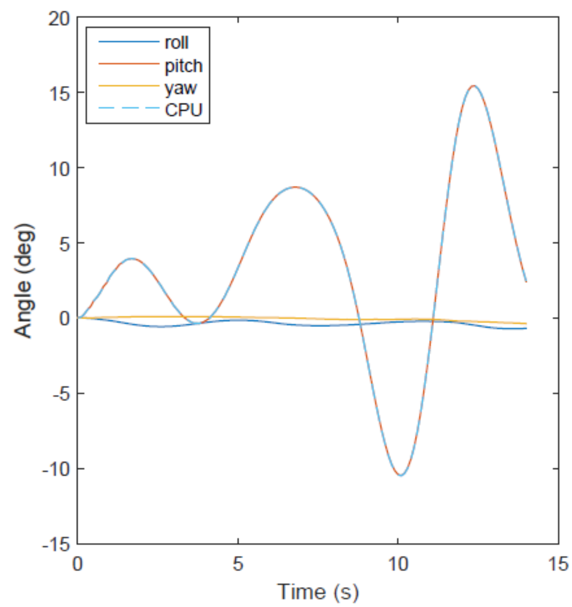


FIGURE 5-7: ROLL, PITCH, AND YAW OF THE FLOATING SHIP. THE DOTTED LINE SHOWS THE SAME FOR CPU COMPUTATION

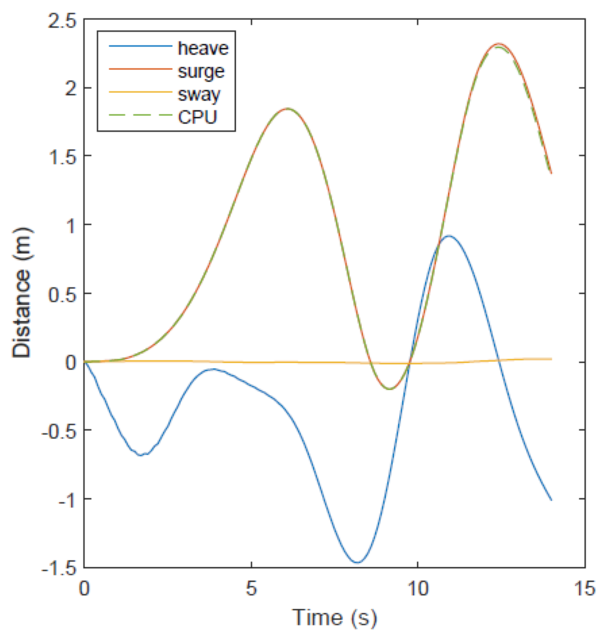


FIGURE 5-8: HEAVE, SURGE, AND SWAY MOTIONS OF THE SHIP. THE DOTTED LINE SHOWS THE SAME FOR CPU COMPUTATION

### 5.3.2 Performance Evaluation of GPU

Now that the accuracy of the GPU computations is validated with the theoretical and the corresponding CPU results, the efficiency of the GPU can be assessed. The performance of the

GPU over CPU is evaluated by comparing the total execution time of the simulation, the time required per iteration, and by comparing computation time distributions for both CPU and GPU executions.

Figure 5-9 compares the total computation time for the 2D wave case. It can be seen that the simulation time for CPU execution increases exponentially compared to that of GPU as the number of particles (np) increases. Figure 5-10 shows the number of time steps processed per second in GPU and CPU for various numbers of particles. It can be seen that for 750,000 particles, GPU can handle ~ 2-time steps per second, while the 16 core CPU can do only ~0.15 timesteps per second. The full simulation costs ~1.5 days (30.38 hrs) on the CPU cores, while the GPU finishes it up within 2.3 hours. Further analysis of the simulation runtime is also evaluated. There are three main steps of SPH computation: neighbor list creation (NL), particle interaction (PI), and system update (SU). Both CPU and GPU spend more than 90% of their respective execution time to calculate PI as shown in Figure 5-11.

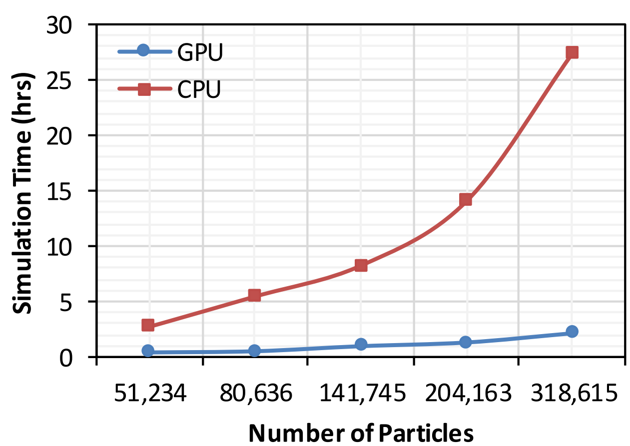


FIGURE 5-9: TOTAL SIMULATION TIME FOR 2D WAVE GENERATION CASE

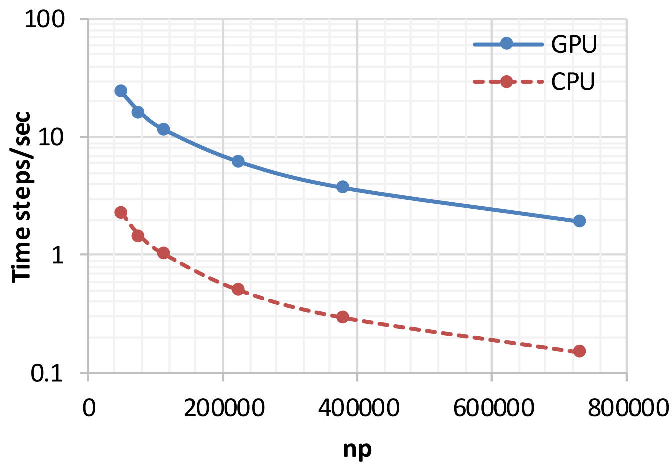


**FIGURE 5-10: PERFORMANCE EVALUATION OF GPU**

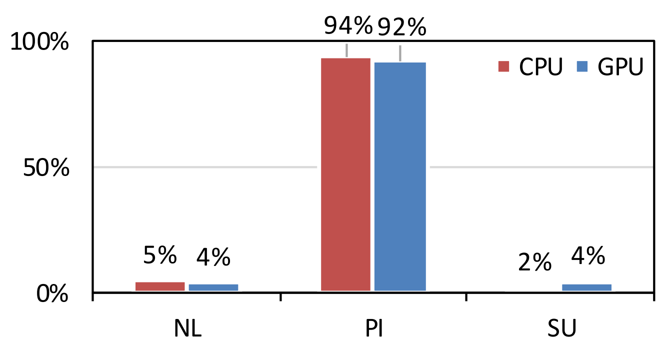


**FIGURE 5-11: COMPUTATION TIME DISTRIBUTION**

Figure 5-12 through to Figure 5-14 compare the percentage of the execution time of NL, PI, and SU for CPU and GPU. GPU spends a larger percentage of time for SU than that of CPU, but as the particle number increases, the percentage decreases significantly and comes closer to CPU percentage.

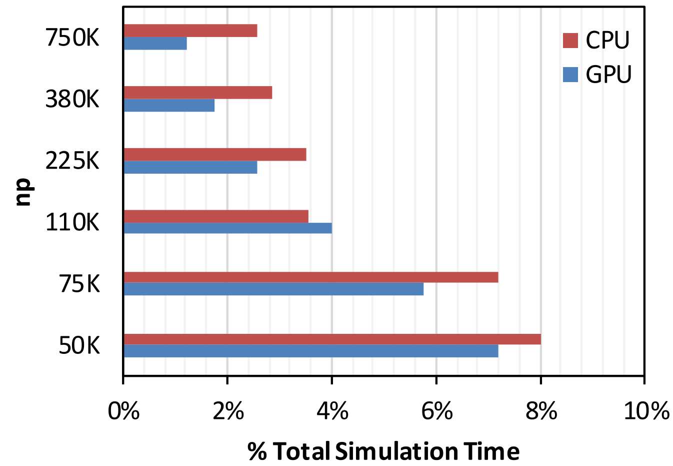


FIGURE 5-12: COMPARISON OF EXECUTION TIME FOR NEIGHBOUR LISTING (NL)

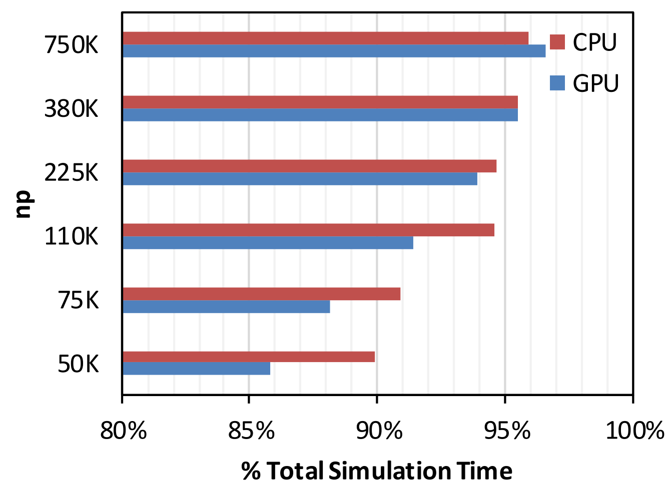


FIGURE 5-13: COMPARISON OF EXECUTION TIME FOR PARTICLE INTERACTION (PI)

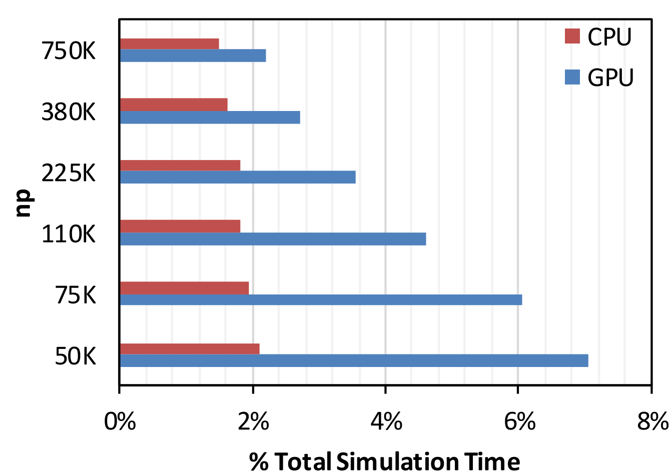


FIGURE 5-14: COMPARISON OF EXECUTION TIME FOR SYSTEM UPDATE (SU)

In other words, the performance of the GPU is more pronounced when the simulation domain is larger. It explains the exponential difference of simulation time between GPU and CPU for a large number of particles in Figure 5-9. For the other two steps (NL and PI), GPU spends less percentage of time than that of CPUs. The overall speedup of a particular simulation depends on hardware constraints and model characteristics (Ansys Inc., 2014). For the current simulation setup, an average speedup of 11 is obtained. For the 2D case, the speedup is around 10, while for the 3D case, it is 11.80.

Figure 5-15 summarizes the performance of the GPU, where two different Y-scales are used for clarity. The overall speedup refers to the Y-scale on the right side, while the rest of the parameters refers to the Y-scale on the left side. In general, the speedup increases as the resolution of the domain increases. The optimal performance of a GPU depends on the simulation size, GPU's architecture, and memory configuration.

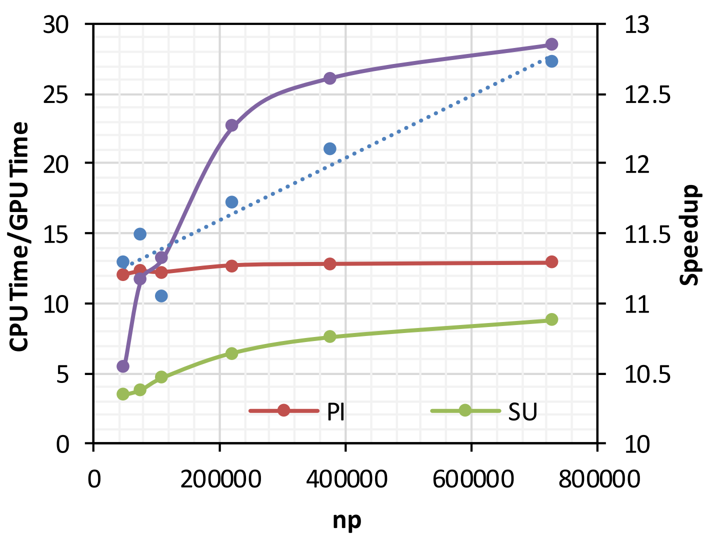


**FIGURE 5-15: EFFICIENCY OF GPU**

### 5.3.3 Cost-Benefit Analysis

The lower TCO and ease-of-maintenance of GPUs in comparison with large multi-core HPC systems are other important advantages. In this section, a straightforward cost-benefit analysis is shown for 5 years timeframe. Table 5-3 gives estimated costs of a 16 core CPU workstation (Henkel and Treiber, 2015) and an enterprise-grade GPU desktop. Please note that hardware maintenance costs and personnel costs are not considered here to keep the calculation simple.

TABLE 5-3: OVERVIEW OF HARDWARE COST

| | **CPU Workstation** | **GPU Desktop** |
|---|---|---|
| Purchase cost | \$10,000 | \$7,000 |
| Depreciation time | 5 years | 5 years |
| Costs per year | \$2,000 | \$1,400 |
| Cost per hour of simulation | \$0.2283 | \$0.1598 |

The cost of a full simulation is calculated for both 2D and 3D cases and compared in Figure 5-16 and Figure 5-17. It is found that GPU not only speedups the simulation time, but also reduces the simulation cost significantly. Figure 5-16 and Figure 5-17 show that, for both 2D and 3D cases, around 90% of the simulation cost can be saved by replacing a multi-core CPU with a single GPU card.

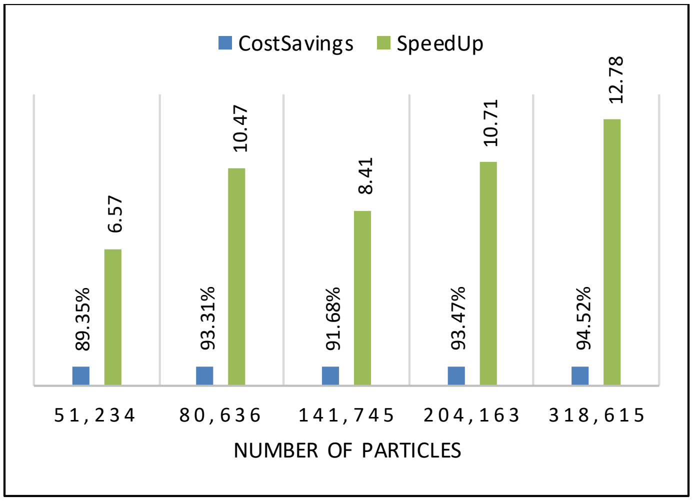


**FIGURE 5-16: POWER/COST RATIO ANALYSIS-2D CASE**

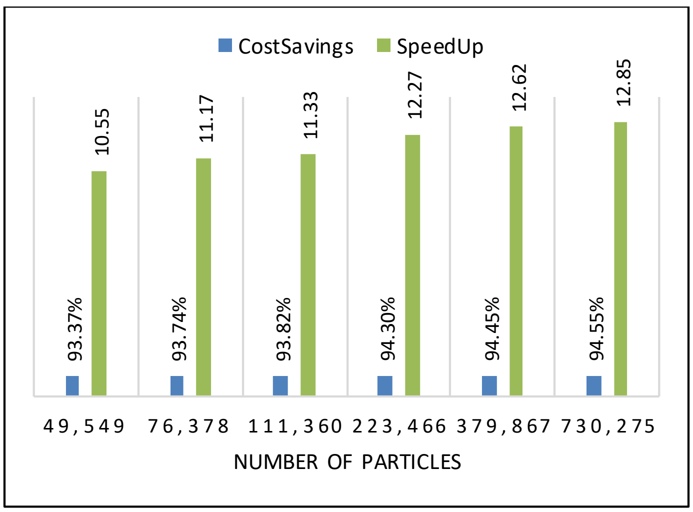


**FIGURE 5-17: POWER/COST RATIO ANALYSIS-3D CASE**

### 5.3.4 Conclusions

The performance and benefits of GPU computing for CFD simulation are discussed in this section. A 2D wave generation and a 3D full-scale 6-DOF floating ship simulation under wave action are simulated to demonstrate the superior computing performance of a single GPU over a multi-core CPU workstation. The accuracy of the GPU computing is validated with the theoretical results and the corresponding CPU computations. The simulations are performed by an open-source SPH-based CFD code, DualSPHysics. It is demonstrated that for both 2D and 3D cases, a regular desktop with a single GPU card can speed up the simulation up to an order of magnitude compared to a 16 core CPU workstation. A mesh-less CFD code is used to evaluate the performances, but the GPU implementation of traditional mesh-based CFD is also performed by other researchers, and a significant reduction of computing time is reported (Ansys Inc., 2014; Jespersen, 2010, 2009; Liu et al., 2016).

Any computer with a CUDA enabled GPU card can be used as high-performance computing (HPC) device. Also, eGPU[1], which is a portable GPU, can be attached to a laptop to transform it to perform as good as a workstation. The performance of multi-GPUs is comparable to a large cluster machine and it can be seen as a future generation computing system. Moreover, the TCO of large clusters is very high, where GPUs are a very cheap alternative that also consumes less energy.

Although there are many advances in the industry, access to reasonably-priced CFD simulation power remains a common challenge. GPU computing can save a significant amount of simulation cost. It is probably cheaper than cloud computing considering the cost of data storage, data transfer, and software costs. Cloud computing can save around 40%[2] cost compared to the 90% saving in this scenario. Future work should focus on the application of multi-GPUs to study more realistic and practical engineering problems even faster. In this study, all the SPH simulations were executed on various GPUs depending on their availability.

---

[1] http://www.nvidia.com/object/quadro-external-graphics.html
[2] https://cfd.direct/cloud/cost/

## 5.4 Simulation of Spray Cloud

### 5.4.1 Introduction

Simulation of spray events involves a range of physics processes: wave breaking, air entrapment, the breakup of water sheets and droplets, de-coupling spray water from green water, and finally distributions of resultant droplets over the deck. Reproducing all these physics elements in an integrated numerical simulation, therefore, is challenging. The multi-scale nature of this problem also makes simulation computationally expensive. However, different stages of the spray process can be modeled separately. In this paper, the open-source code DualSPHysics version 5.0 was used to simulate full-scale wave-generated sea spray. The section is organized as follows: first, the choice of available spray measurement data for validation studies is discussed in the next section. Then various SPH techniques that were employed are discussed. The simulation results are then presented and compared against field measurements and the theoretical model described in Chapter 4.

### 5.4.2 Sea Spray Data

The limited data available for ship-wave impact generated spray falls into two categories: 1) scale model experiments (Chung et al., 1998b; Sapone, 1990) and 2) full-scale field measurements (Borisenkov and Pchelko, 1975; Horjen et al., 1986; Panov, 1976; Ryerson, 1995; Thomas, 1991). For water spray, model scale results are not reliable due to inappropriate scaling of the real phenomenon as described in Section 3.3.2.1 . Among the three studies of full-scale spray generation available in the literature as reported by Samuelsen et al. (2017), data from the 39 m Russian fishing boat "MFV Narva" (Borisenkov and Pchelko, 1975) were selected for validation in this study due to their completeness. This data was also used by many researchers as benchmark data for spray generation (Dehghani et al., 2016a; Kulyakhtin and Tsarau, 2014a; Lozowski et al., 2000; Samuelsen et al., 2017; Shipilova et al., 2012). The data were retrieved and compiled by Zakrzewski (1986b, 1986a) from a soviet icing database and expressed in an empirical formula. How the spray property was measured is, however, unknown.

The amount of water that falls on a deck for a single impact event is described as spray flux (Samuelsen et al., 2017; Zakrzewski, 1986b)

$$F_s = EV_d l_{wc} t_{dur}\ kg/m^2 \quad (77)$$

where $E$ is the collection or collision efficiency of the droplets, $V_d$ is the droplet velocity (assumed to be equal to local relative wind speed), $t_{dur}$ is the duration of the spray event, and $l_{wc}$ is the liquid water content of the spray measured at the field measurements of (Borisenkov and Pchelko (1975) and expressed as

$$w = 24.2\exp(-0.55Z)\ \ g/m^3 \quad (78)$$

where Z is the elevation above the deck of the MFV.

This empirical formula was further generalized by Zakrzewski (1986b) and a new version is proposed in Section 4.2.1 , respectively:

$$l_{wc} = 6.36\mathrm{e}^{-5} H_s V_r^2.\exp\big(-0.55(z-3.5)\big)\ \mathrm{kg/m^3} \quad (79)$$

$$l_{wc} = 4.69e^{-10}.\,\mathrm{E_T}.\exp\big(-0.55(z-3.5)\big)\ \mathrm{kg/m^3} \quad (80)$$

where $H_s$ is the significant wave height, $V_r$ is the ship velocity relative to the wave, $\mathrm{E_T}$ is the total energy released by a single ship-wave impact, $z$ is elevation from the sea level instead of from the deck after Samuelsen et al. (2017).

The total amount of spray water was calculated assuming the spray flux was coming through the "window" of 10 m height and breadth equal to the beam of the vessel as reported by Zakrzewski (1986a). Previous numerical simulations (Mintu et al., 2019) and theoretical models (Dehghani et al., 2016a) indicate this "window" assumption is reasonable.

For the MFV Nava, no lines plan was available in the literature. Based on the available data spread out in multiple references as summarized in Table 4-1, the hull geometry of Narva was estimated using DelftSHIP and Rhino CAD software. Special attention was given to match the bow shape (bulwark contour and stem angle). The lines plan is given in Appendix A and a 3D CAD model is shown in Figure 5-18.

**TABLE 5-4: PRINCIPAL PARTICULARS OF MFV NARVA**

| Parameters | Target Values | Achieved | References |
|---|---|---|---|
| LOA (m) | 39.5 | 39.664 | (Zakrzewski et al., 1988) |
| LBP (m) | N/A | 36.0 | |
| Beam (m) | 7.3 | 7.3 | |
| Draft (m) | 3.0 | 3.0 | |
| Freeboard (m) | 3.5 | 3.5 | (Samuelsen et al., 2017) |
| Stem angle (deg) | 70 | 70 | (Dehghani et al., 2016b) |
| Contour of the bulwark | $X = 0.5457Y^2$ | $X = 0.5457Y^2$ | (Zakrzewski et al., 1988) |
| Displacement (tonne) | 462 | 402.55 | (W.P. Zakrzewski, 1989) |

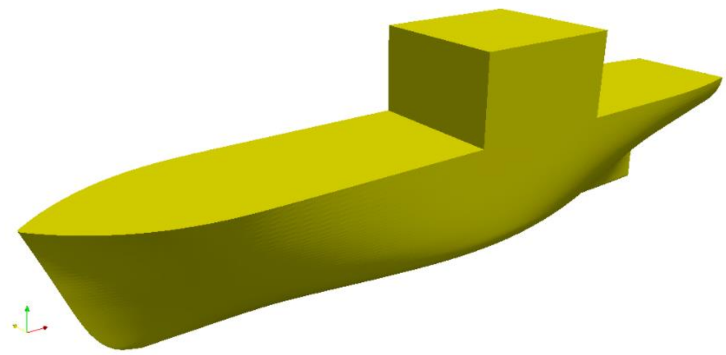

**FIGURE 5-18: 3D CAD MODEL OF MFV NARVA**

### 5.4.3 Boundary Conditions

The size of the domain for this study was selected considering several objectives: 1) to minimize wave reflection, 2) to minimize wave decay during long simulations as reported by Kanehira et al. (2020), and 3) long enough for the moving ship to encounter at least one wave at the highest speed. Different sizes of wave basins with different types of wave generators (piston vs flap) and fitted with dissipative beach or numerical wave absorber at the end of the tank were examined. The domain that demonstrated the best characteristics in terms of accuracy and computational time was selected and is shown in Figure 5-19. A dynamic boundary condition (DBC) (Crespo et al., 2015) was applied to the flap-type wave paddle and the ship. The boundary particles were set to a no-slip condition. The motion of the wave paddle was assigned by a time-dependent input file to generate the target waves. The ship was modeled as a rigid floating object which moves at a desired forward speed with the ability to heave and pitch freely. The other motions were restricted. The ship stops at $2L_{BP}$ from the wave maker, fulfilling ITTC recommendation for inlet boundary condition to avoid any wave reflection. The side walls of the tank were modelled as open boundaries with no physical walls (Gomez-Gesteira et al., 2012), therefore no friction.

The walls were spaced apart by five times the effective beam of the vessel for head sea encounter, a standard size width also used by Kawamura et al. (2016) and Tagliafierro et al. (2021). A numerical wave damper was installed at the end of the tank to cancel out wave reflections (Crespo et al., 2015). Various depths were examined to finalize an optimal depth that fulfills deep water wave criteria.

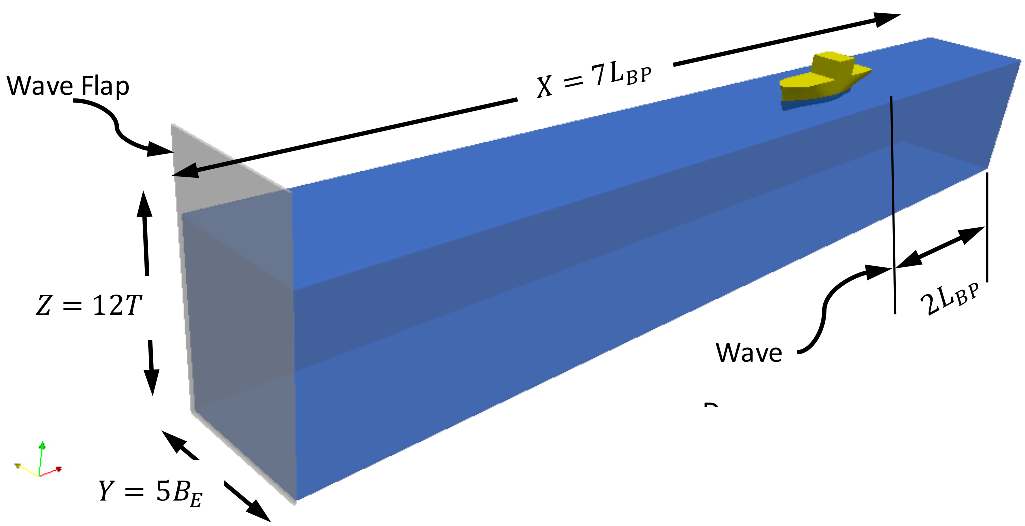


**FIGURE 5-19: FULL-SCALE NUMERICAL WAVE BASIN.**

It was observed in the simulation that the DBC created a non-physical gap between the incoming water and ship's boundary as reported by Kanehira et al. (2020) and Mokos et al. (2016). To counter this numerical effect, a particle shifting technique with a default shifting coefficient was applied. A particle shifting algorithm proposed by Vacondio et al. (2013) for weakly compressible SPH model was employed in this study. The particle shifting distance $\delta r_s$ is given by:

$$\delta r_s = -D\nabla C_i \tag{81}$$

where $D$ is a diffusion coefficient and $C_i$ is the particle concentration calculated as:

$$D = Ah\|\boldsymbol{U}\|_i dt \tag{82}$$

where $A$ is a dimensionless constant, $\|\boldsymbol{U}\|_i$ is the local particle velocity, and $dt$ is the current time step.

$$\nabla C_i = \sum_j \frac{m_j}{\rho_j} \nabla W_{ij} \tag{83}$$

A free surface correction that limits diffusion to the surface normal but allows shifting on the tangent to the free surface was employed to avoid a truncated-kernel error and the consequent non-physical instabilities as reported by Zha et al. (2021).

### 5.4.4 SPH Parameters

A non-dimensional smoothing length of $h/dp = 1.7$ was used as recommended (Altomare et al., 2017; Kanehira et al., 2020). Here, $h$ is the smoothing length and $dp$ is the particle resolution. A second order accurate explicit time integrator called simplistic scheme was employed with a variable time step (Kanehira et al., 2020; Roselli et al., 2019). This scheme also works better for high-frequency impacts expected in this study [DSPH guide v4.2]. A laminar SPS viscosity scheme with a kinematic viscosity of water of $10^{-6}$ $m^2s$ was used to treat the viscous dissipation of momentum.

### 5.4.5 Numerical Collection Box

A numerical collection box of the same size of the "window" (10 m height and breadth equal to the beam of the vessel) and length equal to a few ship lengths was placed just above the deck to capture the spraying water. The box captures the number of particles that go in and out of the pre-defined boundary. It also computes the average velocity of the particles. The volume of the water is calculated by multiplying the volume of one particle by the total number of particles. With the velocity of the particles, the flow rate also can be calculated. An NVIDIA Tesla T4 GPU was used to run the simulations. The specifications are given in Table 5-2.

### 5.4.6 Results and Discussion

#### *5.4.6.1 Wave Generation*

Wave characteristics were not recorded during the field measurements of (Borisenkov and Pchelko, 1975; Panov, 1976), but were later recovered by Zakrzewski (1986b, 1986a) based on the fetch and duration reported by the former authors. As per their report, regular waves of two different heights and various ship lengths to wavelength ratios (L/λ) were generated as tabulated in Table 5-5. The default wave generation function for the flap-type wavemaker of DualSPHysics was not able to produce the waves accurately and so a new wave generation function was implemented. The movement of the flap for deep water was calculated and imposed as an external boundary motion. It is found that for $dp = H/10$, longer waves (3W1 and 6W2) were produced very accurately (within 5% error margin) as shown in Figure 5-20 and Figure 5-21. This $dp$ resolution is also recommended by Altomare et al. (2017). However, for the higher frequency, steeper wave 6W4, a larger error margin was evident when compared with the linear wave theory (see Figure 5-22).

**TABLE 5-5: SELECTED REGULAR WAVE PARAMETERS**

| Wave ID | Wave Height, Hs [m] | Wave Period, Tp [s] | Ship length to Wavelength [L/λ] | Steepness [Hs/λ] |
|---|---|---|---|---|
| 3W1 | 3 | 6.8 | 0.55 | 1/24 |
| 6W2 | 6 | 6.8 | 0.55 | 1/12 |
| 6W4 | 6 | 5.06 | 1.00 | 1/6.65 |

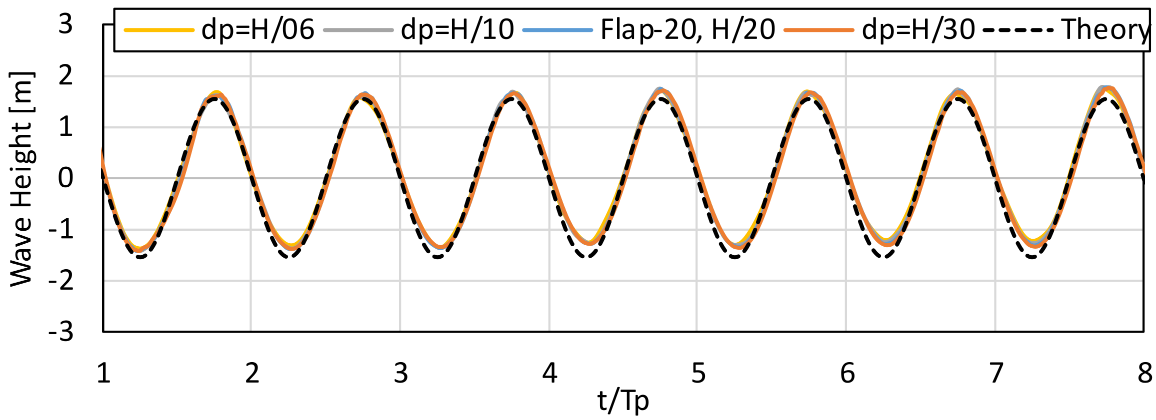


**FIGURE 5-20: COMPARISON OF NUMERICAL AND THEORETICAL WAVE ELEVATION AT VARIOUS PARTICLE RESOLUTIONS FOR 3W1 (HS = 3 M, TP = 6.8 S).**

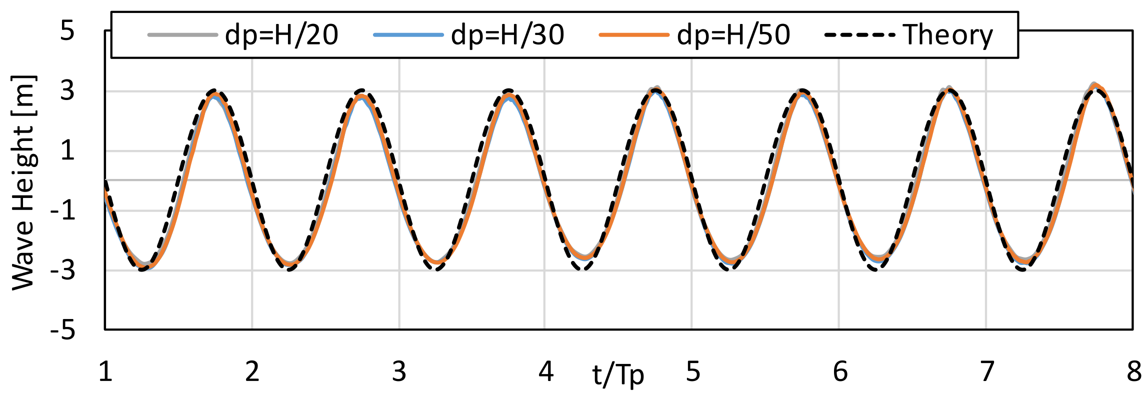


**FIGURE 5-21: COMPARISON OF NUMERICAL AND THEORETICAL WAVE ELEVATION AT VARIOUS PARTICLE RESOLUTIONS FOR 6W2 (HS = 6 M, TP = 6.8 S).**

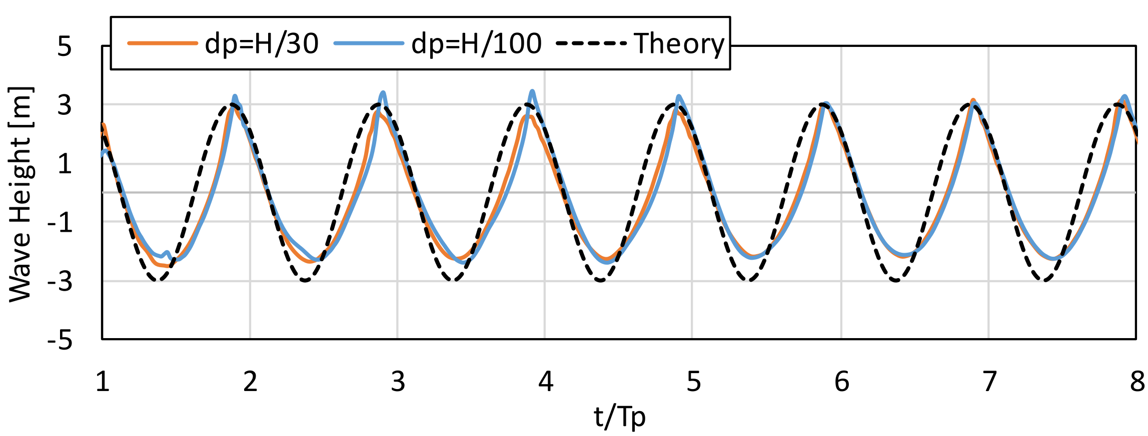


**FIGURE 5-22: COMPARISON OF NUMERICAL AND THEORETICAL WAVE ELEVATION AT VARIOUS PARTICLE RESOLUTIONS FOR 6W4 (HS = 6 M, TP = 5.06 S).**

### *5.4.6.2 2D Spray Simulation*

It was realized early in the study that the generation of spray in a simulated environment would be challenging. At zero forward speed with various encounter frequencies, it was found that the boat simply reacted almost in phase to the incoming wave and resulted in some green water but no sign of spray generation. It was recognized that a surge motion along with heave and pitch with a certain phase difference between waves and ship motions are required to produce spray within the limited size of the wave basin. The timing of the collision between waves and the moving ship is therefore important.

2D simulations were performed first to fine-tune the spray generation, by changing the phase difference between the waves and ship motion. The ship was kept stationary until the wave was fully developed. After four to five wave cycles, the ship was allowed to move forward at designated speeds of Fr 0.156 and 0.222. The ship was allowed to pitch and heave in addition to surge, while roll, sway, and yaw motions were restricted. Figure 5-23 shows the ejection velocity and volume of spray water for each wave impact for Fr 0.156. In addition to visual inspection, a spray ejection velocity threshold was used to distinguish between spray water and green water as defined in Section 4.2.3.5 . Any spray speed below the threshold was considered green water.

For wave 6W2, the wavelength was too long compared to the ship length ($L/\lambda$ =0.55). As a result, excessive pitch motion caused green water shipping. Only spray events occurred at 28.7 s and 37.9 s. With an $L/\lambda$ =1, wave 6W4 created the cleanest spray events (no green water) more frequently than the rest.

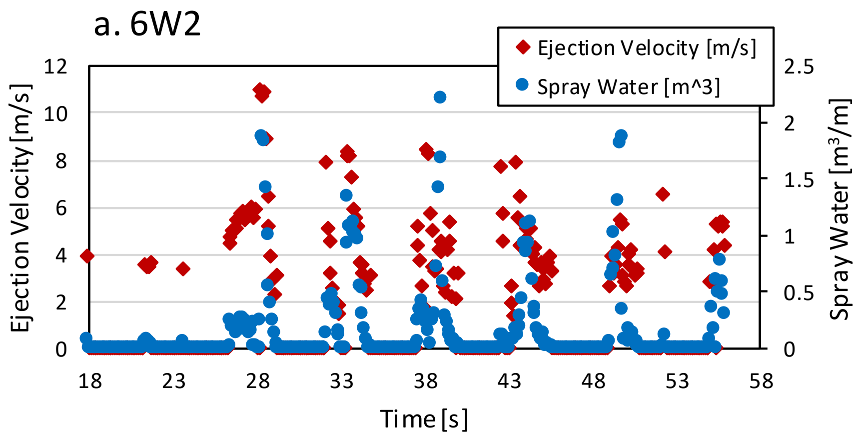


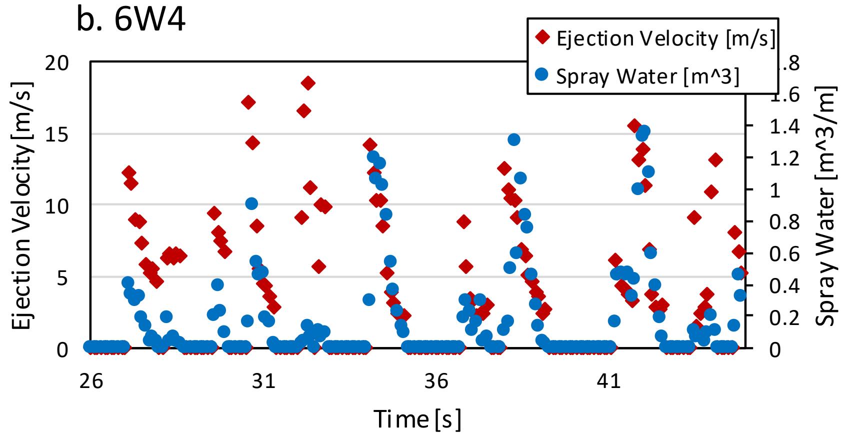


**FIGURE 5-23: NUMERICAL ESTIMATION OF EJECTION VELOCITY AND VOLUME OF SPRAY WATER IN 2D SIMULATION FOR WAVES A) 6W2, B) 6W4, AT FR 0.156.**

### *5.4.6.3 Multi-phase Spray Simulation*

Multi-phase simulations with water and air particles were also conducted in a 2D environment. The same size domain with an additional layer of air particles up to 24 m high was included, giving the domain size 260 m x 60 m. A wind velocity of 11 m/s was imposed on the air particles in the direction of wave propagation in the form of a periodic boundary condition (Crespo et al., 2015). A $dp$ resolution of $H/40$ created ~710,000 particles (water and air) and took 7 hours to simulate

56 s of physical time. A 3D version of the same simulation would require 85 million particles, more than 7 days of run time, which is beyond the limit of the available computing resources. Figure 5-24 demonstrates how wind contributes to the fragmentations of water sheets into spray droplets.

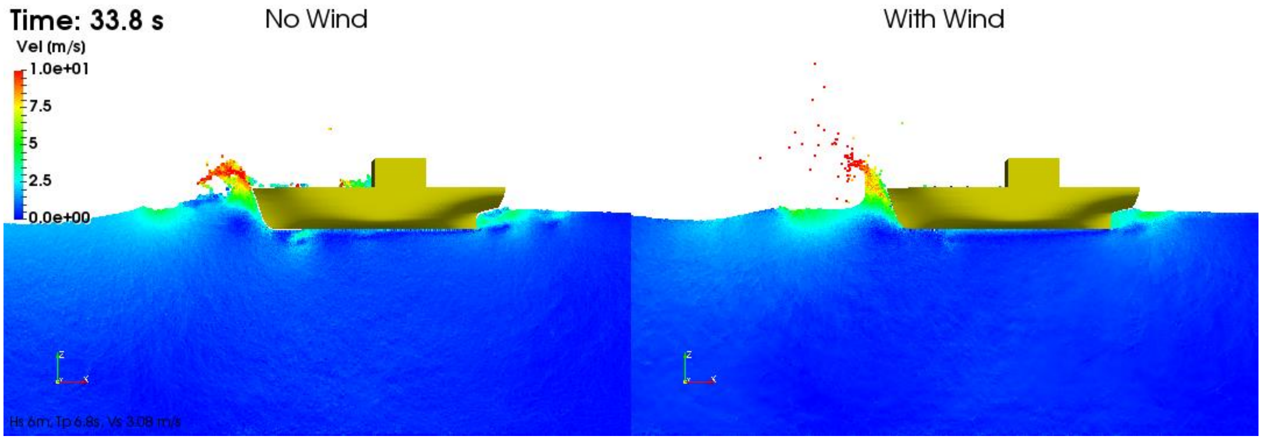


**FIGURE 5-24: CONTRIBUTION OF WIND IN FRAGMENTATION OF WATER SHEET**

### *5.4.6.4 3D Spray Simulation*

Although 2D simulations produced spray events, they are not reliable when the end goal is to estimate the amount of water. The boundary shape of the bow in 3D has varying flare angles that cannot be captured in a 2D simulation. A 3D simulation is therefore desirable. Experience from the 2D simulation guided the selection of the combination of waves and ship speed (Fr) for a 3D simulation as outlined in Table 5-6. Fr 0.144, 0.156, and 0.222 came from the reported field measurements (Borisenkov and Pchelko, 1975; Panov, 1976). A calculated Fr of 0.48 was found to be an ideal speed to achieve an encounter frequency that minimizes the pitch motion of the vessel. This was necessary to decouple spray events from the excessive deck wetness or green water event that were experienced at lower Froude numbers. Sapone (1990) used the same technique in his model experiments. In addition, the ship required less time to travel the wave basin, which in turn optimized simulation run time. All the simulations were run at head sea conditions ($180^0$ relative wave direction). For 3D simulation, the finest possible resolution of H/30 was used and that created more than 35 million particles and took 95 hours (~4 days) to simulate 56 seconds of physical time. Simulation beyond this resolution was not possible due to the memory limit of the GPU.

**TABLE 5-6: SELECTED SHIP SPEED AND WAVES FOR 3D SIMULATIONS**

| Froude number [Fr] | 3W1 | 6W2 | 6W4 |
|---|---|---|---|
| 0.0 | | X | |
| 0.144 | X | | |
| 0.156 | | X | |
| 0.222 | X | | |
| 0.480 | | X | X |

Even though field measurements reported spray, for wave 3W1 at Fr 0.144 the simulation did not produce any spray for this condition. The ship's speed was found to be too low for a relatively long, gentle wave. To determine the amount of spray water, the following steps were adopted for each case. First, time histories of spray water and their ejection velocities were plotted and a spray threshold was used to isolate spray water events from green water events. Second, the time average value of the selected spray water was calculated by integrating the spray event. Figure 5-25 shows the distribution of spray water over time for wave 3W1 at Fr 0.222. The higher bound of this distribution is in reasonable agreement with the field measurement and theoretical model. For the steeper wave 6W2, the SPH predictions are reasonable with the theoretical model, while the empirical formula gave the higher bounds as shown in Figure 5-26 and Figure 5-27. Figure 5-28 shows the development of the spray at various time steps for 6W2 at Fr 0.48.

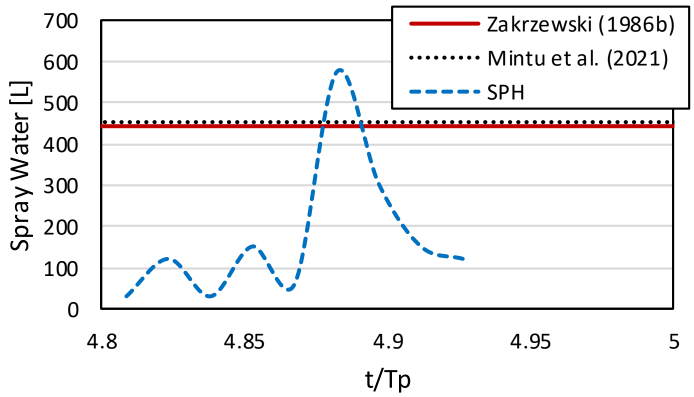


FIGURE 5-25: COMPARISON OF THE AMOUNT OF SPRAY WATER FOR 3W1 (3.09 M, 6.8 S) AT FR 0.222

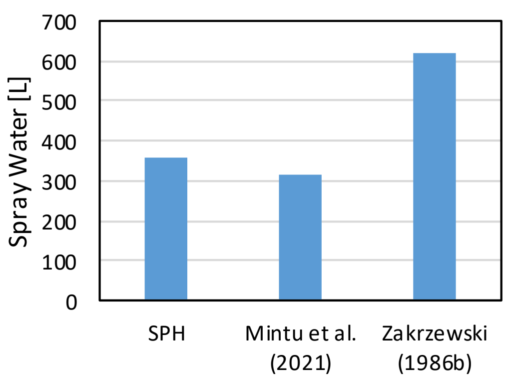


FIGURE 5-26: COMPARISON OF THE AMOUNT OF SPRAY WATER FOR 6W2 (6.0 M, 6.8 S) AT FR 0.156

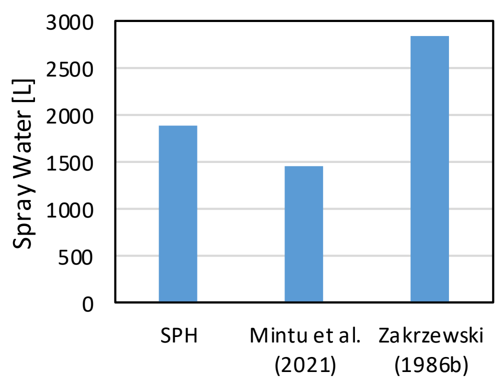


FIGURE 5-27: COMPARISON OF THE AMOUNT OF SPRAY WATER FOR 6W2 (6.0 M, 6.8 S) AT FR 0.48

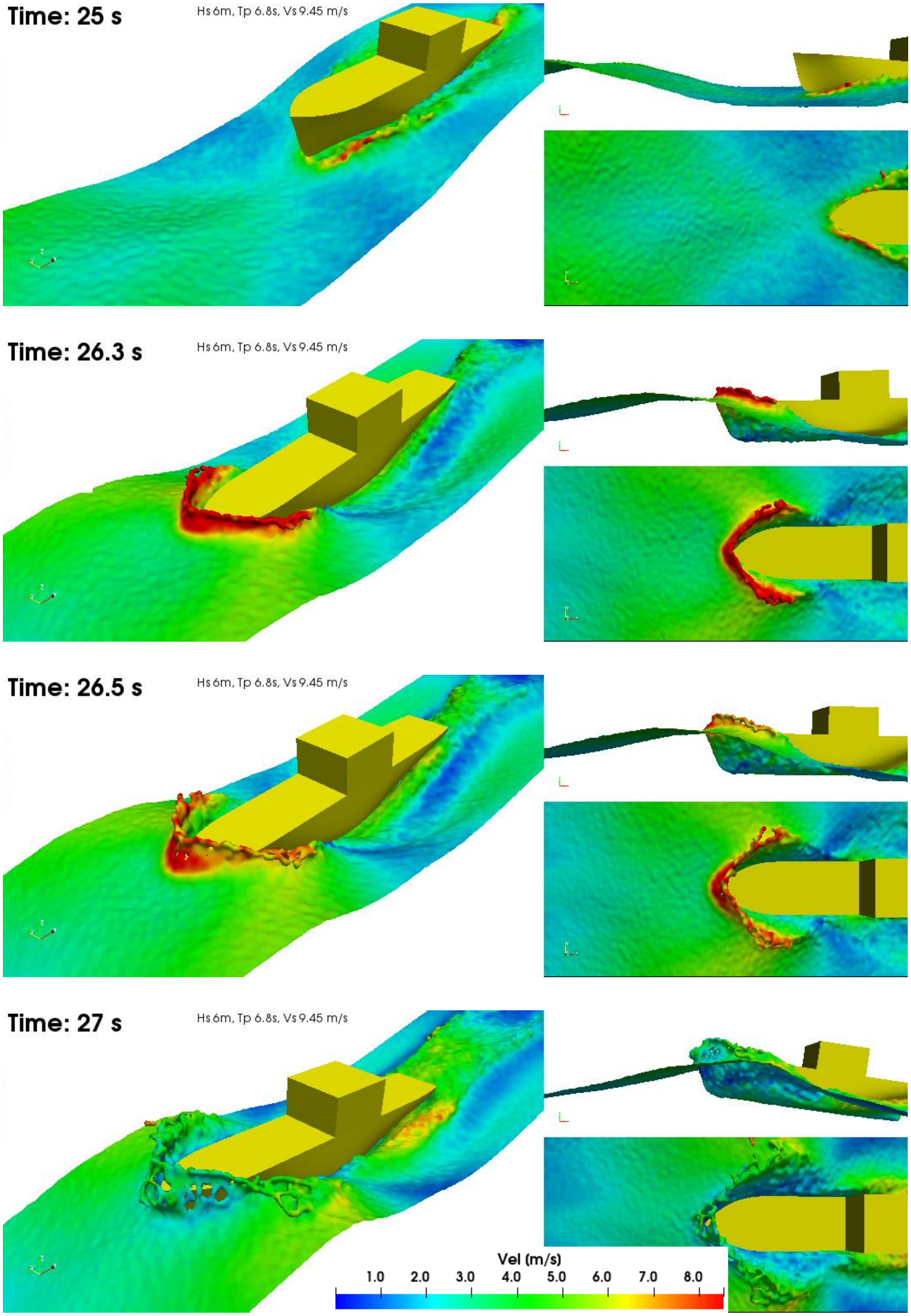


**FIGURE 5-28: DEVELOPMENT OF WAVE IMPACT SPRAY IN 6W2 AT FR 0.48**

Wave 6W4 with L/λ = 1 produced the cleanest spray among all the simulations both in 2D as well as in 3D. This scenario produced an enormous amount of spray water at the bow at the time of impact, but most of the spray deflected out of the deck over time and only a fraction of it ended up on the deck as shown in Figure 5-29. Figure 5-30 compares the amount of spray water with theoretical and empirical models. The final outcome on the amount of spray water onboard, therefore, largely depends on the incident wind speed and direction.

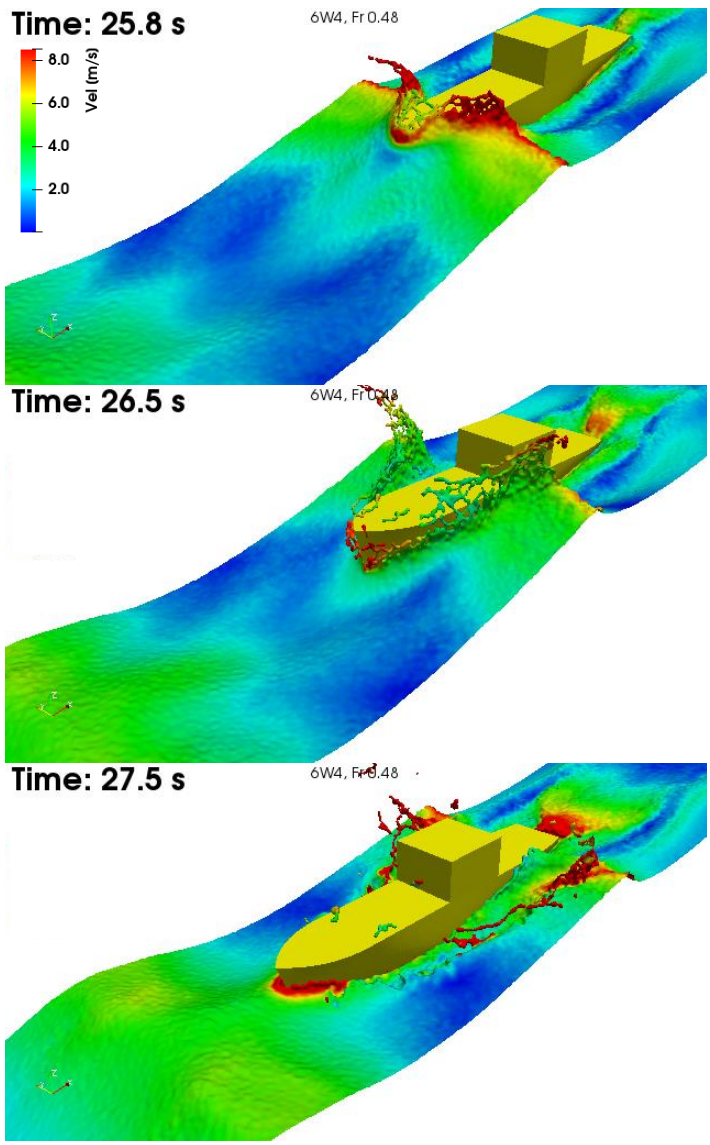


FIGURE 5-29: DEVELOPMENT OF SPRAY IN WAVE 6W4 AT FR 0.48

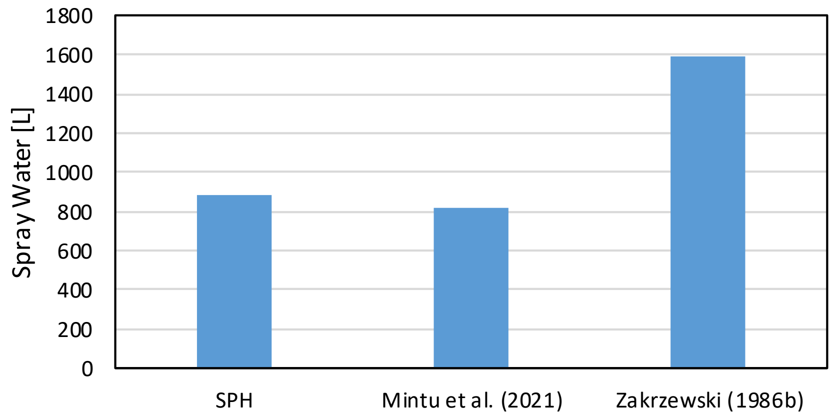


**FIGURE 5-30: COMPARISON OF THE AMOUNT OF SPRAY WATER FOR 6W4 (6.0 M, 5.06 S) AT FR 0.48**

None of the zero forward speed cases generated any spray. The ship model simply rode the incoming wave in a phase similar to 2D cases. This implies that the traditional approach of simulating forward speed using the relative velocity concept may not be ideal for wave generated spray analysis since it is missing the generated wave energy from the moving vessel (Mintu et al., 2021). Figure 5-31 shows a bow wave generated at forward speed in calm water and Figure 5-32 shows a green water event. Such events were excluded from the calculation of the amount of spray water to isolate the spray events. Figure 5-33 shows a sliced view of various phases of the water sheet development over time.

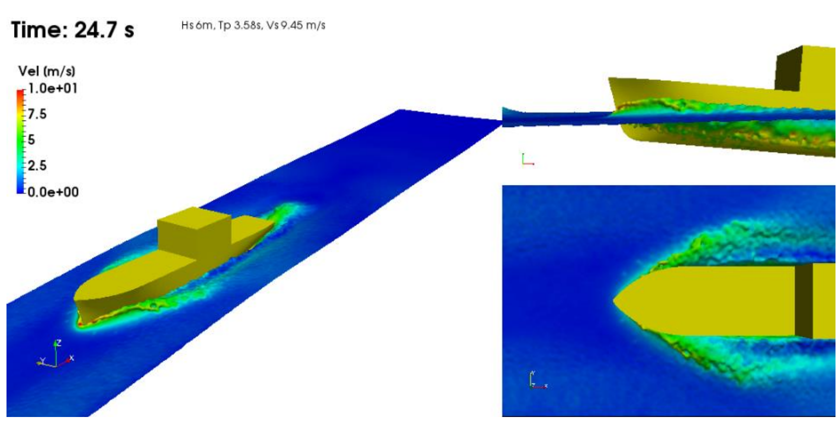


**FIGURE 5-31: BOW WAVE IN CALM WATER**

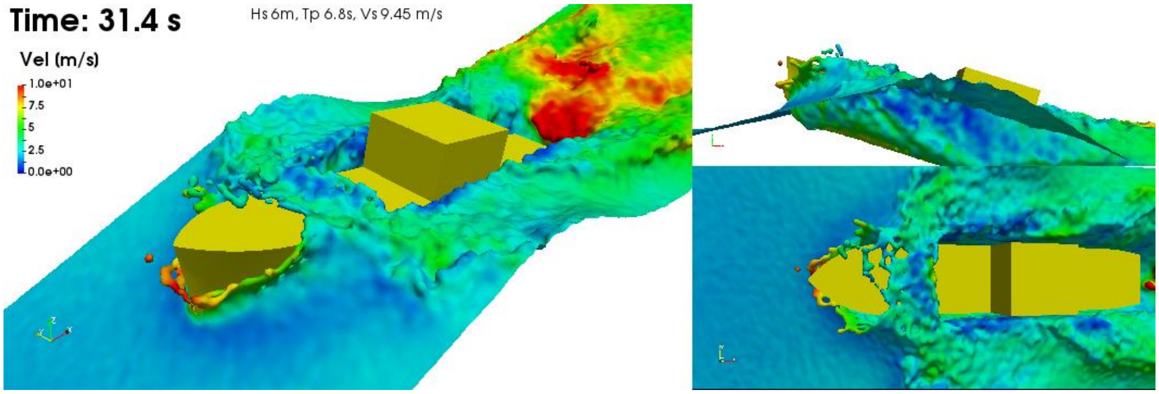


**FIGURE 5-32: GREEN WATER LOADING FOR 6W2 AT FR 0.48**

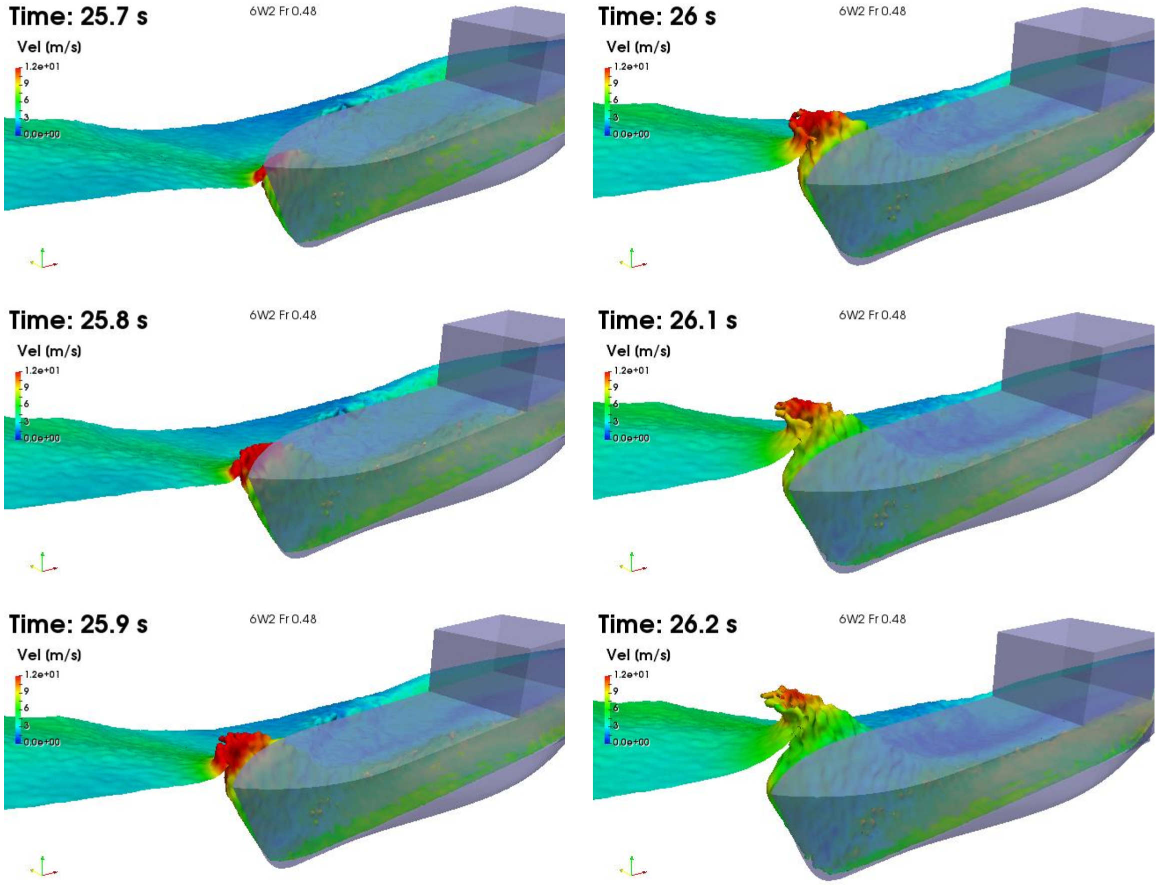


**FIGURE 5-33: DEVELOPMENT PHASES OF WATER SHEET GENERATION DUE TO SHIP-WAVE IMPACT. SLICED VIEW AT THE CENTERLINE OF THE SHIP.**

The particle resolution did not significantly affect the global spray properties. The incoming flow rate of the spray water and the ejection velocity can be seen in Figure 5-34. The particle resolution only affects the local distribution of the spray water. The disintegration of water sheets into ligaments and droplets is better captured at higher resolution as can be seen in Figure 5-35.

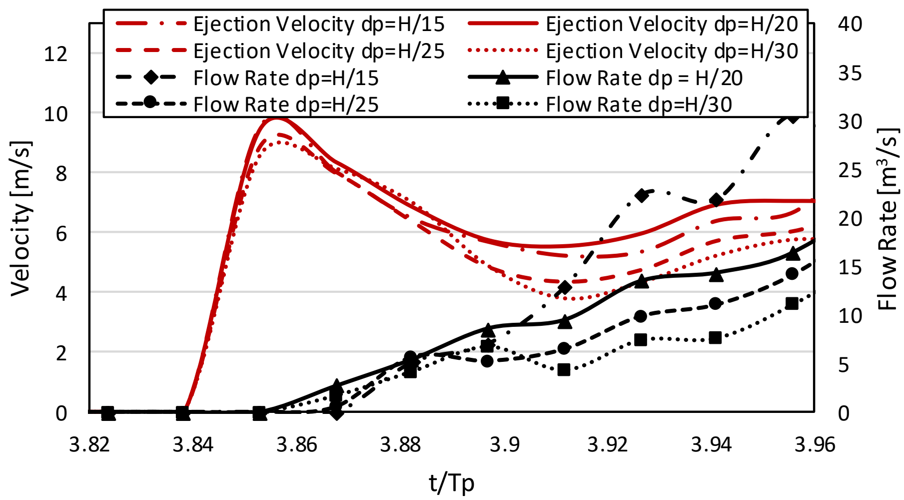


**FIGURE 5-34: EFFECT ON PARTICLE RESOLUTION ON SPRAY PROPERTIES.**

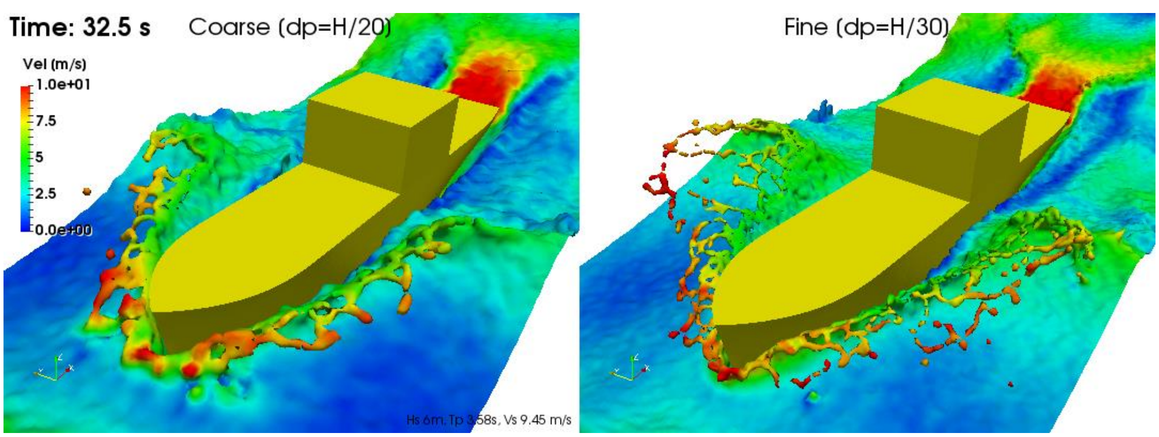


**FIGURE 5-35: FINE VS COURSE RESOLUTION OF THE GENERATED SPRAY. COARSE ON THE LEFT, AND FINE RESOLUTION ON THE RIGHT.**

## 5.5 Simulation of Droplet Distributions

Now that the spray generation is simulated, the next step is to simulate the distributions of the newly formed droplets over the vessel's deck. Droplet concentrations can be divided into three regimes based on the local liquid volume fraction: 1. Dense spray regime, 2. intermediate regime, and 3. dilute regime. The variations in the local liquid-phase volume fraction, droplet deformation, and collision play an important role in determining droplet dynamics correctly due to the mass and momentum transport within the spray influence (Ashgriz, 2011). Accurate spray concentration estimates, therefore, would provide more reliable projections of the total spray cloud (Veron et al., 2012). Theoretical models are currently limited to predicting mono-droplet trajectory, but CFD can overcome it by simulating numerous droplets in a single domain.

### 5.5.1 Boundary Conditions

A periodic open boundary condition (BC) was set at the left and right sides of the computational domain, where the wind blows into the domain from the left wall to the right wall at 11.49 m/s (see Figure 5-36). This BC allows particles that are near an open lateral boundary to interact with the fluid particles near the complementary open lateral boundary on the other side of the domain (Crespo et al., 2015). In effect, the wind particles that leave the outlet wall enter the domain again at the inlet wall. This is a limitation of the current version of the code where an inlet/outlet BC is not available for multi-phase simulations. However, for the short duration of the simulations (0.5 s), the wind flow field was assumed not to be significantly affected. The top and bottom boundaries were modeled as impermeable boundaries with the no-slip condition, where the dynamic boundary approach was used (Shadloo et al., 2016). In this approach, boundary particles are stationary SPH particles (Mokos et al., 2015). The water droplets were modeled as rigid spheres containing the same property of water to preserve the spherical shape throughout the simulation. A similar approach was used by Cleary and Serizawa (2019). The appropriate size of the domain was selected by conducting a sensitivity analysis that is discussed in the next section. Figure 5-36 shows the non-dimensional domain size for the smallest droplet diameter.

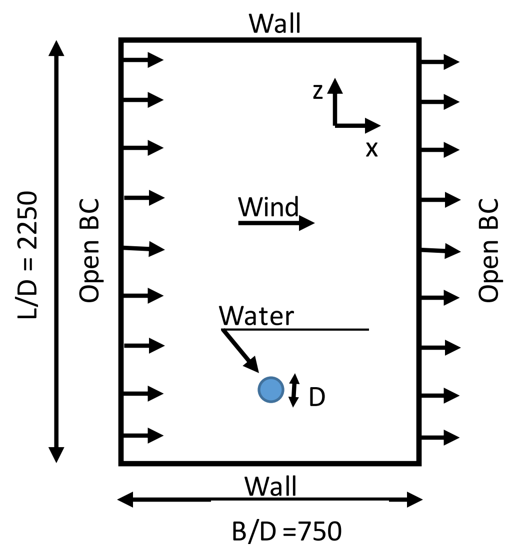


FIGURE 5-36: SIMULATION DOMAIN. DIMENSIONS ARE GIVEN WITH RESPECT TO DROPLET DIAMETER.

### 5.5.2 SPH Parameters

The time-stepping was computed by a Symplectic scheme. Double precision was applied in the particle interaction calculation, and artificial viscosity was used (Crespo et al., 2015). Simulations were conducted using an SPH-based open-source CFD code DualSPHysics (Crespo et al., 2015). An NVIDIA Tesla K80 GPU (Graphics Processing Unit) was used to run the simulations. A GPU is proven to be faster and cheaper than multi-core CPU workstations (Mintu and Molyneux, 2018). The computer containing the GPU card was an Intel ®Xeon® CPU E5-2620 v2 @ 2.10 GHz (2 processors).

### 5.5.3 Sensitivity Analysis of SPH Simulation

Even with the GPU implementation, simulation of water droplets of millimeter-scale in a few meters of trajectory implies a scale difference of three orders of magnitude. This can be very time-consuming to simulate and thus appropriate selection of domain size, particle resolution, and time step selection is necessary to achieve an efficient simulation model without unduly compromising accuracy.

#### *5.5.3.1 Domain Size*

The appropriate size of a domain is a balance between the accuracy of the results and the cost of the simulation. An unnecessarily large domain will cost too much GPU time. Due to the multi-scale nature of the problem, a 3-dimensional domain was beyond the capacity of the available computational resources, hence 2-dimensional simulations were conducted. Two different size domains were compared. The larger size domain was about 3.75 times of the smaller domain and as can be seen in Figure 5-37a, the trajectory of the spray was not significantly affected, hence the smaller domain was selected for the simulations.

#### *5.5.3.2 Particle Spacing*

The next step in optimizing the simulation time is to determine appropriate particle spacing or particle resolution (dp). Various particle spacing ranging from D/2 to D/6 was considered. The results show a trajectory for droplet diameter of 6 mm that converged as the particle resolution increased as shown in Figure 5-37b. The time required to complete the simulation ranges from a few hours to weeks. It was found that $dp = D/3$ gives the optimal results and was selected for the remaining simulations. D/3 is still a relatively coarse resolution for the size of the droplets, but it was not possible within the memory limit of the GPU to run finer resolutions for the smaller droplets. Variable particle spacing could have been a better solution, but this feature was not available in the SPH code at the time of this work. The particle spacing was kept constant for droplets of all sizes in order to be consistent.

*5.5.3.3 Time step Dependency*

Various CFL numbers were tested and the results showed no significant differences for the selected time steps. See Figure 5-37c.

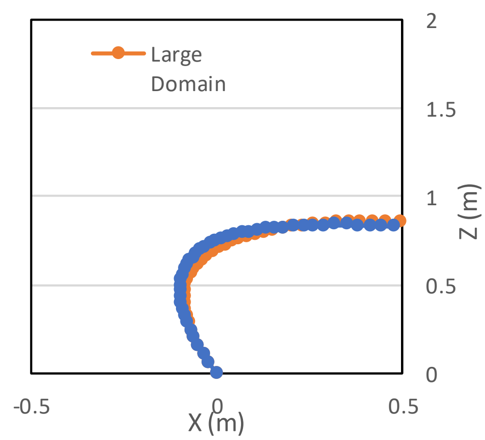


Figure 5-37a: Influence of domain size

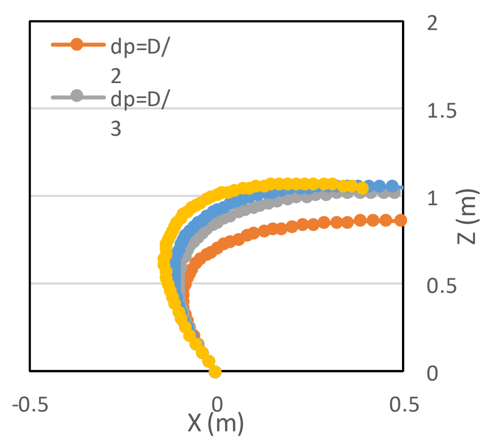


Figure 5-37b: Effect of particle spacing

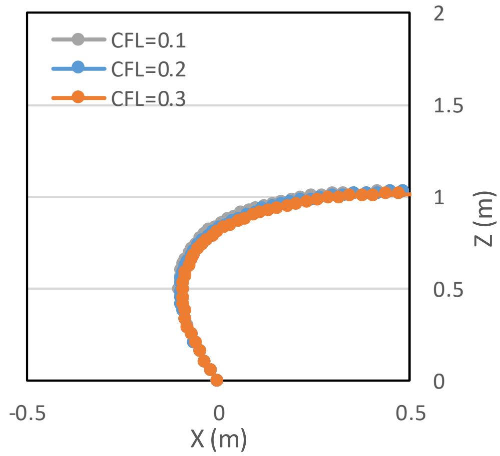


Figure 5-37c: Effect of time step size

**FIGURE 5-37: SENSITIVITY ANALYSIS OF SPH SIMULATION.**

### 5.5.4 Results and Discussion

The field observation data of Borisenkov and Pchelko (1975) was used to examine our simulated trajectory model. For a relative heading angle of 180 degrees (head sea), according to Zakrzewski (1986b), equation (78) becomes:

$$w = 35.5\ x \exp(-0.55Z)\ \ g/m^3 \tag{84}$$

The size of the droplets can range from close to zero to 7.7 mm as reported by Ryerson (1995). The present study considered droplet diameters from 2 mm to 7 mm. Droplets less than 2 mm were not considered since they do not achieve the highest elevation as reported by Dehghani et al. (2016b). Moreover, they require more than 60 million particles that are beyond the memory limit of the available GPU card. Initial velocity distributions were chosen according to the inverse size-velocity dependence and range between 0 to 40 m/s as shown in Figure 5-38. These initial velocities were assumed by Dehghani et al. (2016b) to maintain the target elevation of the spray cloud.

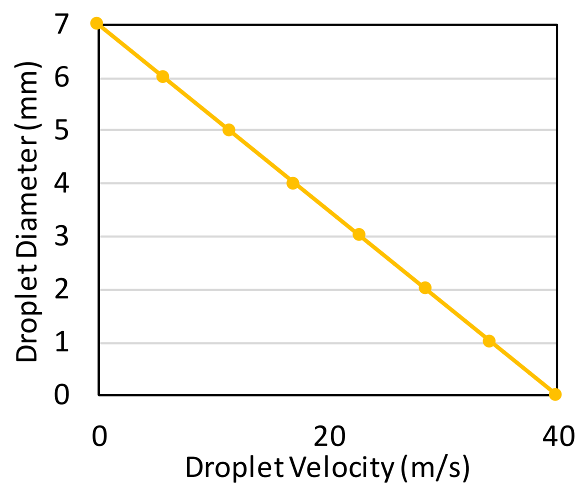


**FIGURE 5-38: SIZE-VELOCITY DISTRIBUTIONS OF THE DROPLETS**

The present study assumes that all the droplets are ejected from the tip of the bow at an ejection angle of 20 degrees; the same bow rake angle of the MFV. The simulated results of the droplet trajectories are compared with the theoretical results of Dehghani et al. (2016b). Figure 5-39 compares the development of the spray cloud over time. All 3-DOF motions for each droplet were captured. Tracking the surge and heave motion in time gives the trajectory of the droplets that are shown by the curved lines in the figure.

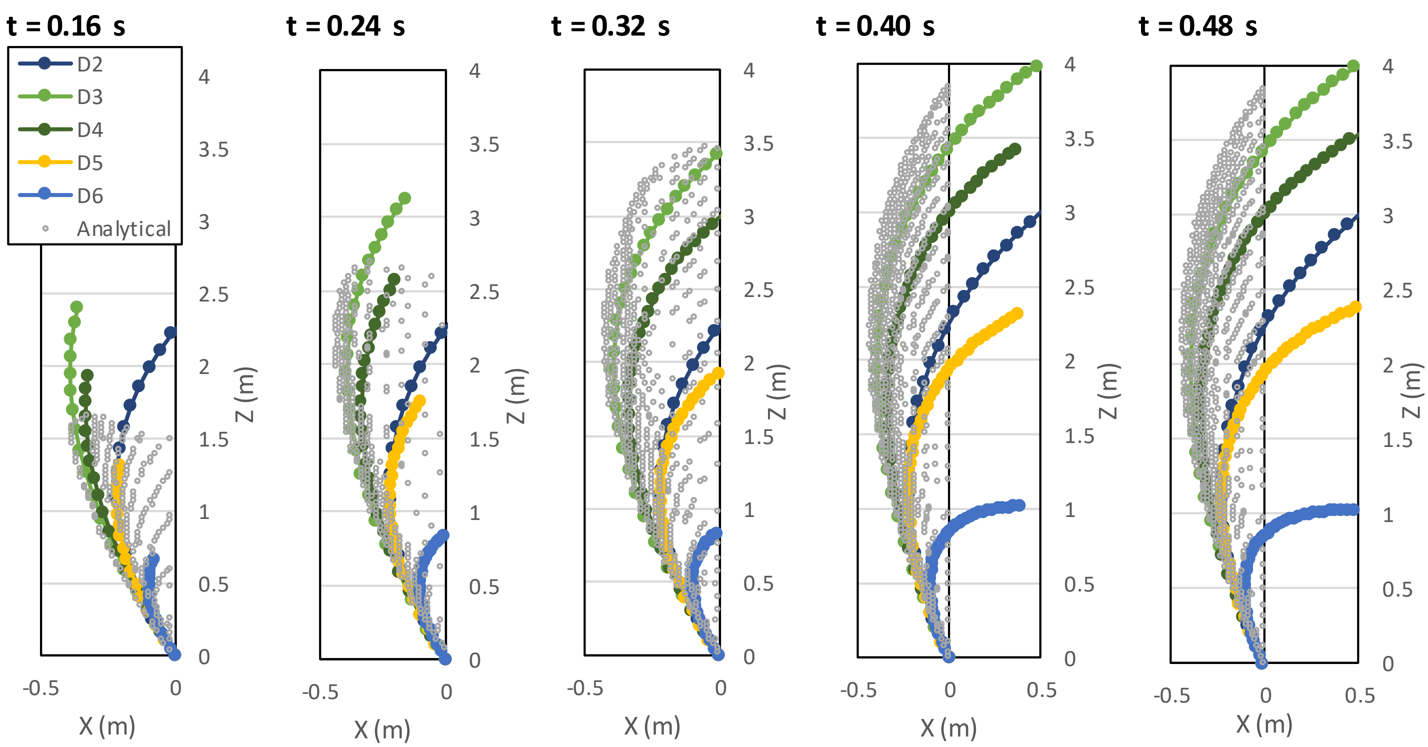


**FIGURE 5-39: COMPARISON OF THE TIME HISTORY OF THE SPRAY CLOUD FORMATION IN FRONT OF THE VESSEL. THE TRAJECTORIES OF 2, 3, 4, 5, AND 6 MM DROPLETS ARE DENOTED BY D2, D3, D4, D5, D6, RESPECTIVELY.**

The maximum surge motion (horizontal movement) of droplets in the counter direction to the wind is about 0.39 m which is achieved by the 3 mm droplet at 0.12 s. The theoretical model predicts 0.45 m. The maximum allowable elevation of 4 m is achieved by the 3 mm droplet at 0.38 s by which time it travels 0.48 m in the positive horizontal direction. The theoretical model predicts 0.4 s to reach the maximum height. The vertical spread of the simulated spray cloud is comparable with the theoretical model, but the horizontal spread is slightly different. All the droplets cross the front of the vessel (x = 0) within 0.31 s of the spray flight, whereas the theoretical prediction is 0.40 s. The development of the spray cloud in the vertical direction is random in the first 0.16 s instead of a smooth development in the theoretical model. Both smaller size droplets and larger droplets cross the front of the vessel (x = 0) quicker than the medium-size droplets as can be seen in Figure 5-40. The medium-size droplets are suspended in the air for a longer period and therefore reach the maximum height.

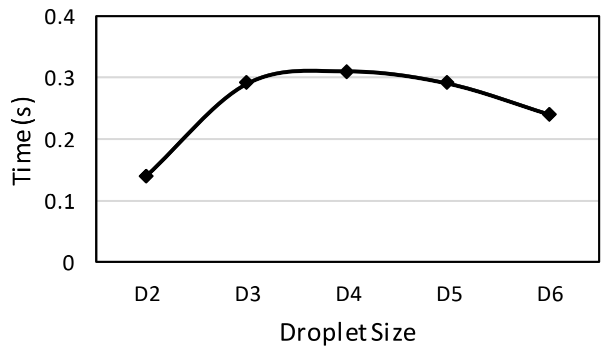


**FIGURE 5-40: FLIGHT TIME OF THE DROPLETS TO CROSS THE FRONT OF THE VESSEL**

As mentioned before, theoretical trajectory models are limited to the assumption of dilute spray. These models neglect droplet collisions and their effect on the airflow field. These simplifications lead to a model that is applied to individual droplets with the spray cloud trajectory derived by adding up the individual trajectories. In reality, droplets travel as a dense spray cloud, and therefore these models are not applicable (Ashgriz, 2011; Dehghani et al., 2018). To predict realistic spray, a fully representative model is required.

The influence of the surrounding droplets may be difficult to model in a theoretical analysis but easy to implement in CFD simulations. It can be examined how the dispersion of multi-droplets affects the trajectory of individual droplets with the validated SPH model. To demonstrate, five droplets of sizes from 3 mm to 7 mm were positioned horizontally at a distance of about 30D apart. The separation distance was calculated based on the LWC equation (Eq. 81) for an average droplet diameter (D) of 3 mm at elevation Z = 0 m. This LWC was considered dilute in the past studies (Dehghani et al., 2018, 2017, 2016b, 2016a). All other parameters (initial velocity, droplet mass, particle spacing, etc.) remained the same. Figure 5-41 compares the trajectories of 3, 4, 5, and 6 mm droplets denoted by D3, D4, D5, D6, respectively, and indicated on the top left corner of the respective figures. The initial velocity of the 7 mm droplet was zero (Dehghani et al., 2016a), so it falls back to the ocean surface and is therefore not shown here.

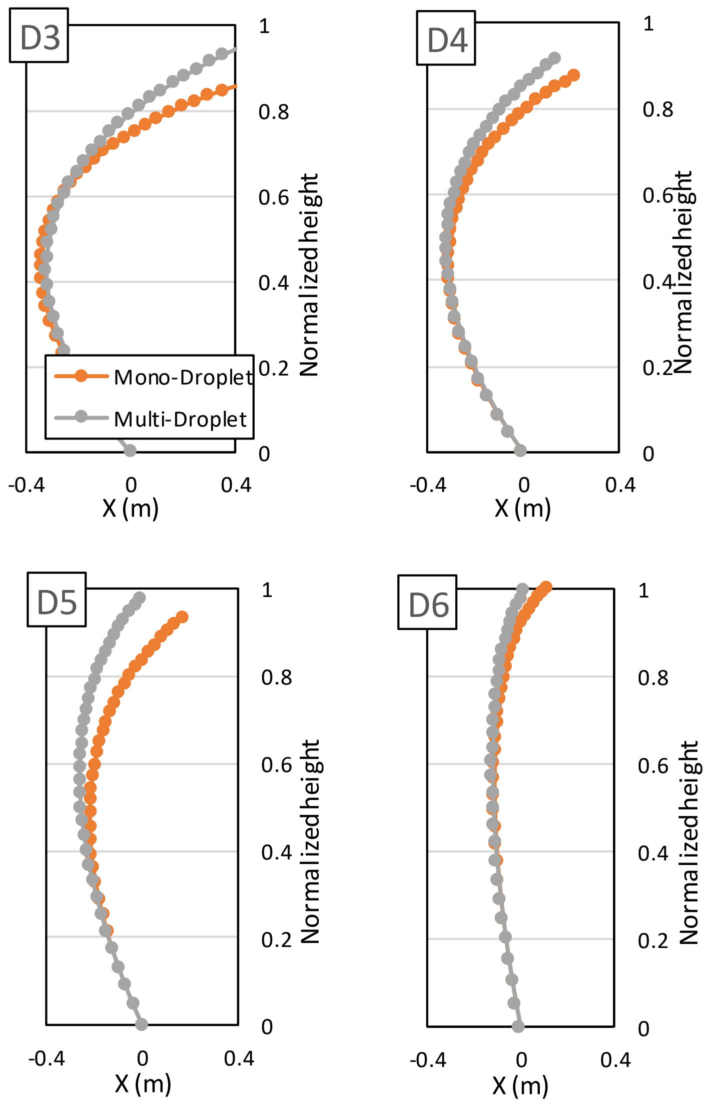


**FIGURE 5-41: EFFECT OF SPRAY CLOUD ON THE TRAJECTORY OF A SINGLE DROPLET**

The figure shows droplets achieve higher elevations in multi-droplet settings compared to that of the single droplet condition. The reason can be explored in Figure 5-42, which shows the surrounding airflow field for 3 mm droplets (presented in yellow color). The flow field is significantly affected by the flow field of the nearest droplet immediately after the ejection, which consequently affects the travel velocity of individual droplets. The influence of the nearest droplet, in this case, 4 mm droplet colored in red, started to diminish after 0.07 s as can be seen in the bottom images of Figure 5-42. After this time, the spray becomes dilute and the droplet travels with its resultant velocity without experiencing any more influence.

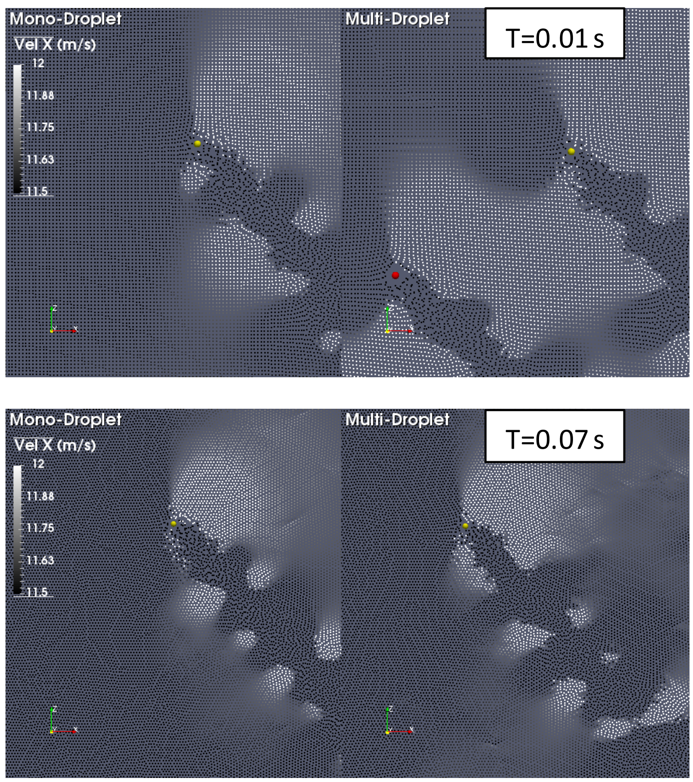


**FIGURE 5-42: COMPARISON OF AIR FLOW FIELD IN MONO AND MULTI-DROPLET CONDITION. DROPLET IN YELLOW COLOR IS 3 MM IN DIAMETER.**

Figure 5-43 compares the travel velocity of the 3 mm droplet for mono and multi-droplet conditions. The velocity in the vertical direction increases in multi-droplet settings, which assists the droplet to achieve a higher elevation.

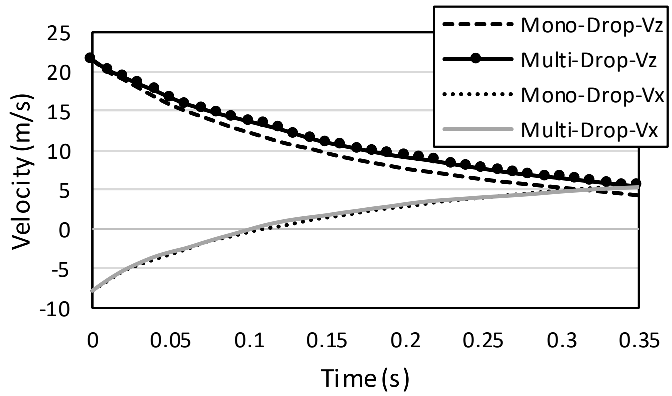


**FIGURE 5-43: COMPARISON OF TRAVEL VELOCITIES FOR 3 MM DROPLET**

A single droplet experiences more drag force during its flight time and thus requires high initial velocity to overcome the gravity and drag force. The airflow field affected by the surrounding droplets due to the momentum exchange between the droplets and air gives less drag to a particular droplet in a parallel flow direction (Ashgriz, 2011). As a result, the travel velocity and therefore maximum height of the droplets increase. Various experimental studies also confirmed this phenomenon. More details can be found in (Ashgriz, 2011). It indicates a cloud of droplets traveling as globules or filaments of water can reach higher elevation with lower ejection velocity.

Previous studies speculated that the initial velocity of the droplets ranges from 0 to 40 m/s (Dehghani et al., 2016a), in some cases 60 m/s (Dehghani et al., 2016b), and even as high as 85 m/s (Dehghani et al., 2017) to achieve the same target LWC. The lack of knowledge of the initial velocity conditions (Veron, 2015) led to these assumptions. Little is known about what controls the size and velocity of droplets formed by the wave-impact sea spray. Without the full understanding of the generation process, it would be erroneous to estimate the spray duration and trajectory (Veron, 2015). Dilute flow assumption may be valid for uniform droplet size and mono-velocity trajectory models since the droplets can maintain the same separation distance throughout the process, but for the droplet size-velocity dependent models, the droplet-to-droplet distance will change over time thus can form a dense cloud at some point. The SPH model shows that droplets that travel in a group require lower initial velocities to reach the same height.

The previous studies also assumed the droplets originate from the very tip of the bow, which also influenced the selection of initial velocities (Dehghani et al., 2018, 2017, 2016a). If a thin sheet of water (highly condensed water droplets) ejects from the bow instead of individual droplets as described in Mintu et al. (2019), it may project higher amounts of water to a higher elevation at lower initial velocity. This emphasizes the importance of a better understanding of the spray generation process since the ejection velocity of droplets depends on it (Veron, 2015). To test this hypothesis, the ejection of a thin sheet of water from the vessel's bow for the same field experiment of Borisenkov and Pchelko (1975) was also simulated using the validated SPH model. The thickness of the water sheet was assumed 8.5 cm after Dehghani et al. (2016b). The initial ejection velocity was tested for a range of velocities. As can be seen from Figure 5-44, an ejection velocity of 12 m/s achieved the desired height of 8 m in less than 1 sec until the droplets reached their terminal velocities. This multi-phase simulation with more than 5 million particles took almost 6 days to finish on a Tesla K80 GPU (see Table 5-2 for the specifications).

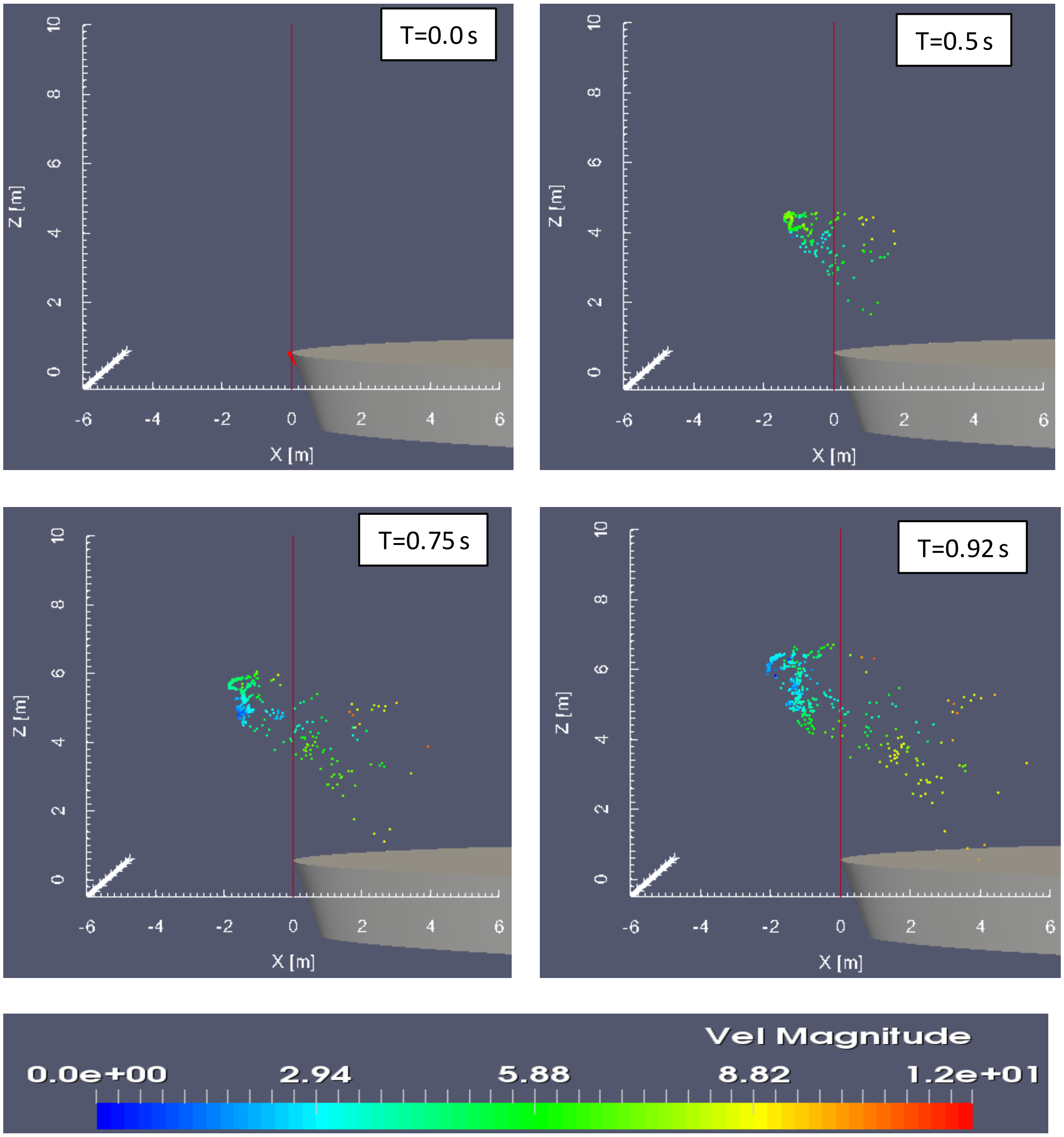


**FIGURE 5-44: SIMULATION OF WATER SHEET BREAKUP AND DROPLET DISTRIBUTION OVER A VESSEL**

# Chapter 6 :

# Conclusions

## 6.1 Summary and Conclusions

Marine-based activities will increase in Polar and sub-Arctic regions as part of overall economic development. A wide range of activities is projected, including tourism, fishing, transportation, and oil and gas exploration and production. It is forecasted that the ice-free arctic will open up new shipping routes for large vessels where they are expected to encounter higher waves (due to the ice-free water) that will make spray more severe than historically experienced. It is important that we have a rational understanding of all the risks for floating systems operating in cold regions, and ice accretion is an area where the regulatory guidance currently available can require different ice loads. It is recommended that ice accretion models be further developed for a fuller understanding of ice accretion such that the rules and regulations can be updated to improve the level of safety at sea.

## 6.2 Conclusions – Theoretical Model

Sea spray generated by ship-wave impact is a complex phenomenon. Empirically derived models are limited to the domain they were created from. Most of the early research provided a climatological estimate of spray properties, neglecting the characteristics of ships. An analysis of wave-generated sprays created by a ship involves many variables, including the geometry of the vessel, its operating conditions, sea states, and the respective motion responses of the vessel. Currently, there is no fully established method available to predict the frequency of spray generation. A theoretical model has been developed for estimating three crucial spray parameters: liquid water contents (LWC), spray event duration, and spray frequency. The present method makes it possible to estimate these parameters considering the main particulars of the vessels and their operating and environmental conditions. A novel method to estimate spray frequency has also been developed that considers seakeeping characteristics of vessels. Analytical expressions have been implemented for computing ship motions as well as rising water velocity making the proposed method a simple and quick estimator for spray frequencies. Spray threshold has been determined in such a way to make sure it considers the ship's relative motions and velocities as well as the contribution from the high impact wave energy. It also distinguishes spray generation events from deck wetness events.

The developed formulas show reasonable agreements against full-scale field observations for a small fishing boat as well as for a large coast guard vessel. The energy-based method shows the potential to be applicable to any sizes and types of vessels in any environmental conditions. More full-scale data, however, is necessary for further validation.

## 6.3 Conclusions – Numerical Model

This study develops a numerical simulation of ship-generated spray due to wave impacts using the smooth particle hydrodynamics (SPH) method both in 2D and 3D. Such simulations offer advantages over scale model experiments and full-scale field trials in the study of spray phenomena. A previously published field experiment of a Russian medium-size fishing vessel was used to compare with the simulation results. Representative regular waves, reported from the field data were reproduced in a deep water numerical wave basin. The basin was fitted with a flap-type wave maker and a numerical wave damper, where the fishing boat traveled at various speeds in head sea conditions. The ship was allowed to surge, heave, and pitch, while other motions were restricted. Creating the simulation "environment" for spray generation was not straightforward. Several techniques for wave generation, wave absorption, ship motion (imposed vs natural), and inlet/outlet boundary conditions were utilized and the best combinations are reported in this study.

The simulations demonstrated the development process of spray generation. This included the process by which the water sheet forms and disintegrates into ligaments and droplets. The amount of spray water was measured by deploying a numerical collection box above the vessel's deck and compared with the field measurements and previously published theoretical models. Special attention was given to distinguishing green water events from spray events. Overall, a good agreement was found with the available data and the theoretical model. No spray was generated for zero forward speed and lower Froude numbers in low-frequency waves. For higher Froude numbers, a significant spray was generated. The ship length to wavelength ratio is shown to play an important role. The simulations can be used to understand the spray generation process for various types of ships and offshore structures. In addition to estimating spray water, it can be used for green water loading. The simulation also allows a time analysis of the spray generation process, which has not been possible up to now.

Using an appropriate simulation particle resolution for a very fine spray cloud in order to capture the correct physics remains a challenge, and is beyond the current computational capabilities of GPU-accelerated or massively parallel CFD software packages (Domínguez et al., 2021). To produce an average droplet size of 3 mm in the simulation, it would require 10^12 (10,000 billion) particles. A variable particle resolution (Vacondio et al., 2016, 2013) together with multi-GPU (Domínguez et al., 2013) implementation could have improved the situation, but neither of these was available as open-source code at the time of this research. These limitations will undoubtedly be reduced over time. Future studies should focus on spray generation in oblique waves for different sizes and types of vessels at various headings. Irregular waves should be considered as much as computing resources permit. The detailed formation of fine droplets and spray clouds considering air compressibility is yet to be considered. Multi-phase simulation in 3D would be the realistic model of this problem and can be developed from this point as software and hardware capabilities are expanded.

The trajectory of water droplets generated by wave impact sea spray has also been simulated using a multi-phase version of DualSPHysics. The cloud motion of various size droplets ranging from 2 mm to 7 mm diameter is predicted. The simulation results are validated against an available analytical model and reasonable agreement is achieved.

It is shown that the dilute flow assumption is not valid for a realistic dense spray cloud. The study reveals that droplets can travel to higher elevations with reduced initial velocities if they travel in the form of a cloud or water sheets instead of individual droplets. The high initial velocities of droplets that were assumed in the past studies may not be required to achieve a target height. This indicates that mono-droplet trajectory models give less accurate results. The theoretical model can be improved by developing appropriate drag models for spray clouds based on the SPH simulation of interacting droplets.

The application of these trajectory models to marine icing has some limitations. Low temperature increases the viscosity of water droplets (Raiyan et al., 2018). These effects are typically neglected in the trajectory models. The two-dimensional simulation can over predict the drag force (Kulyakhtin et al., 2014), which can influence the trajectory. A three-dimensional simulation would be ideal, but difficult to achieve (may need half a billion particles) due to limited computing resources. The SPH method presented in this study also has a limitation. The periodic boundary condition may affect the multi-droplet trajectories which need to be examined by implementing an inlet/outlet boundary condition in future studies.

The study also demonstrates the need for a systematic investigation of the mechanism of wave-impact sea spray. How, when, and where droplets are generated in a wave-impact sea spray will determine how they will be dispersed in the air and transported to the marine structure to form ice.

## 6.4 Recommendations and Future Work

Current trends within regulations are moving toward goal based design rather than prescriptive rules. In order to successfully apply goal based design to ice accretion, we need to combine a method of predicting icing conditions with the amount of ice that will accumulate. This requires knowledge of the conditions likely to cause icing for the area where the ship or offshore structure will operate, the length of exposure to those conditions, the geometry of the structure, and some knowledge of where the ice will accumulate and to what depth, which can finally lead to the stability or other safety factor assessment. All of these elements are presented in separate places, but nothing in the reviewed literature brings them all together into a unified methodology.

For example, Overland et al. (1986) and ISO 19906 both give predicted ice growth rates based on wind speed and air temperature, together with some estimates of the expected duration that the structure can be exposed to the freezing conditions. There are some promising approaches to calculating ice accretion, such as the numerical models, RIGICE and ICEMOD, which have been developed over time and continue to be improved. Validation of all these methods against observations in the field is lacking. Icing models based on numerical simulations are, however, computationally intensive (Dehghani-Sanij et al., 2017). Based on the numerical and analytical models for spray generation, Overland's icing predictor (Overland et al., 1986) can be extended to include the vessel-dependent icing model. Overland defines the icing rate as:

$$\frac{dHi}{dt} \propto \frac{V_a\left(T_f - T_a\right)}{1 + \varphi\left(T_w - T_f\right)} \tag{85}$$

$$\varphi = \frac{C_w}{L_i F} \tag{86}$$

where $T_f, T_w, T_a$ are the temperature of saline ice at the freezing point, seawater, and air, respectively. $C_w$ is the specific heat of sea water, $L_i$ is the latent heat of freezing of saline water, and $F$ is the fraction of impinging sea water remaining on the vessel and available for freezing. Assuming $F$ is a function of the spray flux $F_s$ , we can rewrite the equations as follows:

$$\frac{dHi}{dt} \propto \frac{V_a\left(T_f - T_a\right)}{1 + \frac{C_w}{L_i f(F_s)}\left(T_w - T_f\right)} \tag{87}$$

The model should be applicable to all types of vessels operating in cold environments and expected to be able to forecast icing on each particular vessel depending on its characteristics.

Mathematical models have limitations to reproduce nature completely (Horjen, 2015). Validation data collected from a real-world observation is crucial to benchmark the models. Field measurements using state-of-the-art equipment should be conducted. Vessels can be equipped with LiDAR to measure droplet sizes and distributions (Varlas et al., 2021; Vivekanandan et al., 2020) and wave properties (Gao et al., 2017; Garby, 2019; Huang et al., 2018). Onboard vessel motion monitoring system can provide the motion data, and satellite GPS can provide the vessel's location, heading, speed etc., and the icing sensors (Elzaidi et al., 2021) can track the accumulation of ice. Temperature both for air and water should also be captured. The entire set of instruments can be included in the central vessel monitoring system that will not only boost the safety features of the vessels but also collects valuable data along the way for the scientific community to study and predict icing more accurately.

The stochastic nature of field measurements can be compensated by model scale experiments in controlled environments. However, the use of model experiment data to estimate full-scale estimates has some inherent uncertainties (Kulyakhtin and Tsarau, 2014a; Zakrzewski, 1986a). Appropriate scaling of spray properties and measurements in model scale experiments remains a challenge (Chung et al., 1998b; Sapone, 1990). Scaling spray properties require to scale not only the wave properties but also the viscosity of water and air (Muzik and Kirby, 1992). One way this can be achieved is by scaling the impact pressure and/or scale the wind velocity (Muzik and Kirby, 1992) to disintegrate the rising sheet at the shear stress equal to the full-scale values. Prediction of the icing process after the spray can also be conducted in a cold room. Effect of droplet dynamics, impinging on the surface, time to form ice, distribution of droplets vs location of ice formation, the effect of wind, etc. can be considered.

The prediction models can help to make an appropriate plan for seafarers. To minimize the prediction uncertainty and to make the crew aware of any unseen incident, an onboard icing monitoring system and a consequent remedial process should be in place. The evolving mass properties in ice accumulation can be monitored indirectly by a "stochastic inversion framework" developed by Lin and Earls (2019). The model needs inputs from an onboard vessel motion monitoring system and seakeeping software. By tracking the change in ship motion (roll/heave/pitch period), the model can hypothetically predict the amount of ice.

The final goal should be developing a formula-based prediction model by combining all the knowledge gathered from previous tasks. To this end, machine learning (ML) techniques capable of feature extractions can be applied. It will require a vast amount of data that can come from various sources like theoretical, experimental, and numerical models.

# References


Aalbers, A. B., & Poen, G. J. (2015). Probabilistic Modelling of Marine Icing: An Estimation Method for Spray Water. *Arctic Technology Conference*. https://doi.org/10.4043/25536-MS

ABS. (2015). *Guide for Vessels Operating in Low Temperature Environments*. American Bureau of Shipping. https://ww2.eagle.org/content/dam/eagle/rules-and-guides/current/special_service/151_vesselsoperatinginlowtemperatureenvironments/LTE_Guide_e-Feb16-New%20Logo.pdf

Ahmed, M., Ashgriz, N., & Tran, H. N. (2009). Break-up length and spreading angle of liquid sheets formed by splash plate nozzles. *Journal of Fluids Engineering, Transactions of the ASME*, *131*(1), 0113061–0113069. https://doi.org/10.1115/1.3026729

Alawneh, S., Thijssen, J. W., & Richard, M. (2016, October). *Accelerating Numerical Ice Engineering Tools Using GPGPU*. Arctic Technology Conference, St. John's, NL. https://doi.org/10.4043/27386-MS

Altomare, C., Crespo, A. J. C., Domínguez, J. M., Gómez-Gesteira, M., Suzuki, T., & Verwaest, T. (2015). Applicability of Smoothed Particle Hydrodynamics for estimation of sea wave impact on coastal structures. *Coastal Engineering*, *96*(Journal Article), 1–12. https://doi.org/10.1016/j.coastaleng.2014.11.001

Altomare, C., Domínguez, J. M., Crespo, A. J. C., González-Cao, J., Suzuki, T., Gómez-Gesteira, M., & Troch, P. (2017). Long-crested wave generation and absorption for SPH- based DualSPHysics model. *Coastal Engineering; Coastal Engineering*, *127*(Journal Article), 37–54. https://doi.org/10.1016/j.coastaleng.2017.06.004

Altomare, C., Tafuni, A., Domínguez, J. M., Crespo, A. J. C., Gironella, X., & Sospedra, J. (2020). SPH Simulations of Real Sea Waves Impacting a Large-Scale Structure. *Journal of Marine Science and Engineering*, *8*(826), 826. https://doi.org/10.3390/jmse8100826

Anderson, D. N. (2003). *A Preliminary Study of Ice- Accretion Scaling for SLD Conditions—NASA/ CR- 2003- 211824*.

Andreas, E. L. (1990). Time constants for the evolution of sea spray droplets. *Tellus B*, *42*(5), 481–497. https://doi.org/10.1034/j.1600-0889.1990.t01-3-00007.x

Ansys Inc. (2014). *Accelerating Ansys Fluent 15.0 Using Nvidia GPUs* (DA-07311-001_v01). Ansys Inc. https://www.nvidia.com/content/tesla/pdf/ansys-fluent-nvidiagpu-userguide.pdf

Arctic Operations Handbook. (2013). *Arctic Marine Operations Challenges & Recommendations, Volume 5 Marine Icing on Arctic Offshore Operations—Pilot Project*. http://www.arctic-operations-handbook.info/.

Ashgriz, N. (2011). *Handbook of Atomization and Sprays: Theory and Applications*. New York, NY: Springer.

Batchelor, G. K. (1967). *An introduction to fluid dynamics*. Cambridge : University Press.

Begovic, E., Gatin, I., Jasak, H., & Rinauro, B. (2020). CFD simulations for surf-riding occurrence assessment. *Ocean Engineering*, *218*. https://doi.org/10.1016/j.oceaneng.2020.107975

Bhattacharyya, R. (1978). *Dynamics of marine vehicles*. Wiley.

Blackmore, R. Z., & Lozowski, E. P. (1994). An heuristic freezing spray model of vessel icing. *International Journal of Offshore and Polar Engineering*, *4*(2), 119–126.

Blackmore, R. Z., & Lozowski, E. P. (1997). *A theoretical investigation of the distribution of freshwater spongy spray icing on a vertical cylinder*. *2*, 633–639.

Bodaghkhani, A., Dehghani, S.-R., Muzychka, Y. S., & Colbourne, B. (2016). Understanding spray cloud formation by wave impact on marine objects. *Cold Regions Science and Technology*. https://doi.org/10.1016/j.coldregions.2016.06.008

Bodaghkhani, A., Muzychka, Y., & Colbourne, B. (2018). An analytical model of final average droplet size prediction of wave spray cloud. *International Journal of Heat and Fluid Flow*, *74*, 110–117. https://doi.org/10.1016/j.ijheatfluidflow.2018.09.012

Borisenkov, Y. P., & Pchelko, I. G. (1975). Indicators for Forecasting Ship Icing. *U.S. Army Cold Regions Research and Engineering Laboratory*, *USACRREL Draft Translation. No. 481.*, 65.

Brown, R. D., & Agnew, T. (1985). Characteristics of Marine Icing in Canadian Waters. . . *In Proceedings of the International Workshop on Offshore Wind and Icing, 7–11 October, Halifax, Nova Scotia.*, *Journal Article*.

Brown, R. D., & Roebber, P. (1985). *The scope of the ice accretion problem in Canadian waters related to offshore energy and transportation.* (p. 295). Canadian Climate Centre Report 85–13 unpublished manuscript.

Buchner, B., van den Berg, J., Helder, J., & Bunnik, T. (2014). Non-Linear Wave Runup Along the Side of Ships Causing Green Water Problems: Experiments and First CFD Calculations. *Proceedings of the 33rd International Conference on Ocean, Offshore and Arctic Engineering*, *Volume 1A: Offshore Technology*. https://doi.org/10.1115/OMAE2014-23022

Chen, N., Ji, H., Hu, Y., Wang, J., & Cao, G. (2015). Experimental study of icing accretion on a rotating conical spinner. *Heat and Mass Transfer; Wärme- Und Stoffübertragung*, *51*(12), 1717–1729. https://doi.org/10.1007/s00231-015-1536-0

Chung, K. K., Forest, T. W., Lozowski, E. P., Gagnon, R., Faulkner, B., & Chekhar, M. (1998). *Application of new measurement and simulation methods to marine icing on offshore structures*. *Journal Article*, 551–558.

Chung, K. K., & Lozowski, E. P. (1998). A three-dimensional time-dependent icing model for a stern trawler. *J. Ship Res*, *42*(4), 266–273.

Chung, K. K., Lozowski, E. P., & Gagnon, R. (1999). *On the exponential decay of spray flux in the marine environment*. *OMAE99/OFT-4011*, 1–9.

Chung, K. K., Lozowski, E. P., Zakrzewski, W. P., & Gagnon, R. E. (1995). *A model for spraying and three-dimensional icing on a stern trawler*. *4*, 123–130.

Chung, K. K., Lozowski, E. P., Zakrzewski, W. P., Gagnon, R., & Thompson, T. (1998). Spraying experiments with a model stern trawler. *Journal of Ship Research*, *42*(4), 260–265.

Clanet, C., & Villermaux, E. (2002). Life of a smooth liquid sheet. *Journal of Fluid Mechanics*, *462*, 307–340. https://doi.org/10.1017/S0022112002008339

Cleary, P. W., & Serizawa, Y. (2019). A coupled discrete droplet and SPH model for predicting spray impingement onto surfaces and into fluid pools. *Applied Mathematical Modelling*, *69*, 301–329. https://doi.org/10.1016/j.apm.2018.12.024

Cooker, M. J., & Peregrine, D. H. (1995). Pressure-impulse theory for liquid impact problems. *Journal of Fluid Mechanics*, *297*, 193–214. https://doi.org/10.1017/S0022112095003053

Crespo, A., Dominguez, J., Barreiro, A., Gómez-Gesteira, M., & Rogers, B. (2011). GPUs, a New Tool of Acceleration in CFD: Efficiency and Reliability on Smoothed Particle Hydrodynamics Methods. *PLoS One*, *6*(6). https://doi.org/10.1371/journal.pone.0020685

Crespo, A. J. C., Domínguez, J. M., Rogers, B. D., Gómez-Gesteira, M., Longshaw, S., Canelas, R. B., Vacondio, R., Barreiro, A., & García-Feal, O. (2015). DualSPHysics: Open-source parallel CFD solver based on Smoothed Particle Hydrodynamics (SPH). *Computer Physics Communications*, *187*(Journal Article), 204–216.

CSA. (2004). *General Requirements, Design Criteria, the Environment and Loads. CSA – S471.* (CAN/CSA-S471-04). Canadian Standards Association.

Dalrymple, R. A., & Rogers, B. D. (2006). Numerical modeling of water waves with the SPH method. *Coastal Hydrodynamics and Morphodynamics*, *53*(2), 141–147. https://doi.org/10.1016/j.coastaleng.2005.10.004

Dehghani, S. R., Muzychka, Y. S., & Naterer, G. F. (2016). Droplet trajectories of wave-impact sea spray on a marine vessel. *Cold Regions Science and Technology*, *127*, 1–9. https://doi.org/10.1016/j.coldregions.2016.03.010

Dehghani, S. R., Muzychka, Y. S., & Naterer, G. F. (2017). Water breakup phenomena in wave-impact sea spray on a vessel. *Ocean Engineering*. https://doi.org/10.1016/j.oceaneng.2017.02.013

Dehghani, S. R., Naterer, G. F., & Muzychka, Y. S. (2016). Droplet size and velocity distributions of wave- impact sea spray over a marine vessel. *Cold Regions Science and Technology*, *132*, 60–67. https://doi.org/10.1016/j.coldregions.2016.09.013

Dehghani, S. R., Naterer, G. F., & Muzychka, Y. S. (2018). 3-D trajectory analysis of wave-impact sea spray over a marine vessel. *Cold Regions Science and Technology*, *146*, 72–80. https://doi.org/10.1016/j.coldregions.2017.11.016

Dehghani-Sanij, A. R., Dehghani, S. R., Naterer, G. F., & Muzychka, Y. S. (2017). Marine icing phenomena on vessels and offshore structures: Prediction and analysis. *Ocean Engineering*, *143*, 1–23. https://doi.org/10.1016/j.oceaneng.2017.07.049

Dias, F., & Ghidaglia, J.-M. (2018). Slamming: Recent Progress in the Evaluation of Impact Pressures. *Annual Review of Fluid Mechanics; Annu.Rev.Fluid Mech.*, *50*(1), 243–273. https://doi.org/10.1146/annurev-fluid-010816-060121

DNV-GL. (2015a). *Rules for Classification: Ships, Part 5 Ship types, Chapter 12 Fishing Vessels*. Det Norske Veritas.

DNV-GL. (2015b). *Rules for Classification: Ships, Part 6 Additional class notations, Chapter 6 Cold climate*. Det Norske Veritas.

Dombrowski, N., & Johns, W. R. (1963). The aerodynamic instability and disintegration of viscous liquid sheets. *Chemical Engineering Science*, *18*(3), 203–214. https://doi.org/10.1016/0009-2509(63)85005-8

Domínguez, J. M., Crespo, A. J. C., Hall, M., Altomare, C., Wu, M., Stratigaki, V., Troch, P., Cappietti, L., & Gómez-Gesteira, M. (2019). SPH simulation of floating structures with moorings. *Coastal Engineering (Amsterdam)*, *153*, 103560. https://doi.org/10.1016/j.coastaleng.2019.103560

Domínguez, J. M., Crespo, A. J. C., Valdez-Balderas, D., Rogers, B. D., & Gómez-Gesteira, M. (2013). New multi-GPU implementation for smoothed particle hydrodynamics on heterogeneous clusters. *Computer Physics Communications*, *184*(8), 1848–1860. https://doi.org/10.1016/j.cpc.2013.03.008

Domínguez, J. M., Fourtakas, G., Altomare, C., Canelas, R. B., Tafuni, A., García-Feal, O., Martínez-Estévez, I., Mokos, A., Vacondio, R., Crespo, A. J. C., Rogers, B. D., Stansby, P. K., & Gómez-Gesteira, M. (2021). DualSPHysics: From fluid dynamics to multiphysics problems. *Computational Particle Mechanics*. https://doi.org/10.1007/s40571-021-00404-2

Dommermuth, D. G., Lewis, C. D., Tran, V. H., & Valenciano, M. A. (2014, November 2). *Direct Simulations of Wind-Driven Breaking Ocean Waves with Data Assimilation*. 30th Symposium on Naval Hydrodynamics, Hobart, Tasmania, Australia. https://arxiv.org/abs/1410.0418

Dommermuth, D. G., O'Shea, T., T., Wyatt, D. C., Ratcliffe, T., Weymouth, G. D., Hendrikson, K. L., Yue, D. K., Sussman, M., Adams, P., & Valenciano, M. (2007). *An Application of Cartesian-Grid and Volume-of- Fluid Methods to Numerical Ship Hydrodynamics* (D. C. SCIENCE APPLICATIONS INTERNATIONAL CORP SAN, Ed.). https://apps.dtic.mil/dtic/tr/fulltext/u2/p023891.pdf

Du, Y., Wang, W., Wang, L., & Huang, Y. (2017). A combined first- and second-order theory for the deckwetness prediction of sandglass-type floating body in irregular head waves. *Marine Structures*, *54*, 23–37. https://doi.org/10.1016/j.marstruc.2017.03.002

Eide, L. I. (1983). *Environmental Conditions in the Barents Sea and Near Jan Mayen.* [Technical Report]. Norwegian Meteorological Institute.

Elzaidi, A., Masek, V., & Bruneau, S. (2021). Marine Icing Sensor with Phase Discrimination. *Sensors (Basel, Switzerland)*, *21*(2), 612. https://doi.org/10.3390/s21020612

Forest, T. W., Lozowski, E. P., & Gagnon, R. (2005). Estimating marine icing on offshore structures using RIGICE04. *Proceedings of the 11th International Workshop on Atmospheric Icing of Structures*, *8*.

Fourtakas, G., Vacondio, R., Dominguez, J., & Rogers, B. D. (2020). *Improved density diffusion term for long duration wave propagation*. Proceedings of the International SPHERIC Workshop, Harbin, China.

Fu, T., O'Shea, T., Judge, C., Dommermuth, D., Brucker, K., & Wyatt, D. (2013). A detailed assessment of numerical flow analysis (NFA) to predict the hydrodynamics of a deep- V planing hull. *International Shipbuilding Progress*, *60*(1–4), 143–169. https://doi.org/10.3233/ISP-130087

Fuentes, E., Coe, H., Green, D., de Leeuw, G., & Mcfiggans, G. (2010). Laboratory-generated primary marine aerosol via bubble-bursting and atomization. *Atmospheric Measurement Techniques*, *3*(1), 141–162. https://doi.org/10.5194/amt-3-141-2010

Gagnon, R., Sullivan, M., Pearson, W., Bruce, W., Cluett, D., Gibling, L., & Li, L. F. (2009). Development of a marine icing monitoring system. *Proceedings of the International Conference on Port and Ocean Engineering under Arctic Conditions, POAC*, *1*, 711–719.

Gao, J., Sun, J., Wang, Q., & Cong, M. (2017). 4-D imaging of the short scale ocean waves using a slit streak tube imaging Lidar. *Optik (Stuttgart)*, *136*, 136–143. https://doi.org/10.1016/j.ijleo.2017.02.029

Garby, B. (2019). *The Effect of Ocean Waves on Airborne Lidar Bathymetry* [Masters thesis]. University of Colorado at Boulder.

Gingold, R. A., & Monaghan, J. J. (1977). Smoothed particle hydrodynamics: Theory and application to non-spherical stars. *Monthly Notices of the Royal Astronomical Society*, *181*(3), 375–389. https://doi.org/10.1093/mnras/181.3.375

Gomez-Gesteira, M., Rogers, B. D., Crespo, A. J. C., Dalrymple, R. A., Narayanaswamy, M., & Dominguez, J. M. (2012). SPHysics – development of a free-surface fluid solver – Part 1: Theory and formulations. *Computers & Geosciences*, *48*, 289–299. https://doi.org/10.1016/j.cageo.2012.02.029

Greco, M., Colicchio, G., Lugni, C., & Faltinsen, O. M. (2013). 3D domain decomposition for violent wave- ship interactions. *International Journal for Numerical Methods in Engineering*, *95*(8), 661–684. https://doi.org/10.1002/nme.4523

Guilcher, P. M., Jus, Y., Couty, N., Brosset, L., Scolan, Y. M., & Le Touzé, D. (2014, June). *2D Simulations of Breaking Wave Impacts on a Flat Rigid Wall – Part 1: Influence of the Wave Shape.* The Twenty-fourth International Ocean and Polar Engineering Conference, Busan, Korea.

Hansen, E. S. (2012). *Numerical modelling of marine icing on offshore structures and vessels*. Norwegian University of Science and Technology.

Henkel, N., & Treiber, S. (2015). *Cost Effective Sizing of Your HPC Cluster for CAE Simulations*. 10th European LS-DYNA Conference, Germany.

Horjen, I. (1989, June 12). Numerical Modelling of the Sea Spray Icing on Vessels. *Proceedings of the 10th International Conference on Port and Ocean Engineering Under Arctic Conditions*.

Horjen, I. (2013). Numerical modeling of two-dimensional sea spray icing on vessel-mounted cylinders. *Cold Regions Science and Technology*, *93*, 20–35. https://doi.org/10.1016/j.coldregions.2013.05.003

Horjen, I. (2015). Offshore drilling rig ice accretion modeling including a surficial brine film. *Cold Regions Science and Technology*, 84-110.

Horjen, I., Løset, S., & Vefsnmo, S. (1986). *Icing Hazards on Supply Vessels and Stand-By Boats* (N-7034). Norwegian Hydrotechnical Laboratory.

Horjen, I., & Vefsnmo, S. (1985). A Kinematic and Thermodynamic Analysis of Sea Spray (in Norwegian),. *Offshore Icing — Phase II. STF60 F85014, Norwegian Hydrodynamic Laboratory (NHL), Norway.*, *Journal Article*.

Horjen, I., Vefsnmo, S., & and Bjerke, P. L. (1988). Sea Spray Icing on Rigs and Supply Vessels. *Norwegian Hydrodynamic Laboratories. ESARC Report 15.*

Huang, Z.-C., Yeh, C.-Y., Tseng, K.-H., & Hsu, W.-Y. (2018). A UAV-RTK lidar system for wave and tide measurements in coastal zones. *Journal of Atmospheric and Oceanic Technology*, *35*(8), 1557–1570. https://doi.org/10.1175/JTECH-D-17-0199.1

IMO. (2011). *Sub-Committee on Stability and Load Lines and on Fishing Vessels Safety*. International Maritime Organization.

IMO MEPC 68/6/2. (2015). *Draft International Code for Ships Operating in Polar Waters (Polar Code)*. *Laws/Statutes*.

ISO. (2010). *Petroleum and natural gas industries—Arctic offshore structures. Final Draft International Standard. ISO/FDIS 19906.*

Jensen, J., & Mansour, A. E. (2003). Estimation of the Effect of Green Water and Bow Flare Slamming on the Wave-Induced Vertical Bending Moment Using Closed-Form Expressions. In R. E. Taylor (Ed.), *Proceedings of the 3rd International Conference on Hydroelasticity in Marine Technology* (pp. 155–161). The University of Oxford.

Jensen, J., Mansour, A. E., & Olsen, A. S. (2004). Estimation of ship motions using closed-form expressions. *Ocean Engineering*, *31*(1), 61–85. https://doi.org/10.1016/S0029-8018(03)00108-2

Jespersen, D. C. (2009). *Acceleration of a CFD Code with a GPU* (NAS Technical Report NAS-09-003). NASA/Ames Research Center.

Jespersen, D. C. (2010). Acceleration of a CFD Code with a GPU. *Scientific Programming*, *18*(3), 193–201. https://doi.org/10.3233/SPR-2010-0309

Jones, K. F., & Andreas, E. L. (2009). *Sea Spray Icing of Drilling and Production Platforms* (ERDC/CRREL TR-09-3). U.S. Army Engineer Research and Development Center.

Jones, K. F., & Andreas, E. L. (2012). Sea spray concentrations and the icing of fixed offshore structures. *Quarterly Journal of the Royal Meteorological Society*, *138*(662), 131–144. https://doi.org/10.1002/qj.897

Kanehira, T., Mutsuda, H., Draycott, S., Taniguchi, N., Nakashima, T., Doi, Y., & Ingram, D. (2020). Numerical re-creation of multi-directional waves in a circular basin using a particle based method. *Ocean Engineering*, *209*, 107446. https://doi.org/10.1016/j.oceaneng.2020.107446

Katchurin, L. G., Gashin, L. I., & Smirnov, I. A. (1974). Icing Rate of Small Displacement Fishing Vessels under Various Hydro-Meteorological Conditions. *Transl. into ENGLISH from Meteorol. Gidrol. (Moscow)*, *3*, pp.-50-60.

Kawamura, K., Hashimoto, H., Matsuda, A., & Terada, D. (2016). SPH simulation of ship behaviour in severe water- shipping situations. *Ocean Engineering*, *120*(Journal Article), 220–229. https://doi.org/10.1016/j.oceaneng.2016.04.026

Koss, H. H., Gjelstrup, H., & Georgakis, C. T. (2012). Experimental study of ice accretion on circular cylinders at moderate low temperatures. *Journal of Wind Engineering and Industrial Aerodynamics; 13th International Conference on Wind Engineering*, *104â€“106*(Journal Article), 540–546. https://doi.org/10.1016/j.jweia.2012.03.024

Kubat, I., & Timco, G. (2005). NRC Marine Icing Database. *Proceedings 11th International Workshop on Atmospheric Icing of Structures (IWAIS), XI, Montréal*(Journal Article).

Kulyakhtin, A., Kulyakhtin, S., & Løset, S. (2016). The role of the ice heat conduction in the ice growth caused by periodic sea spray. *Cold Regions Science and Technology*, *127*(Journal Article), 93–108. https://doi.org/10.1016/j.coldregions.2016.04.001

Kulyakhtin, A., Shipilova, O., & Muskulus, M. (2014). Numerical simulation of droplet impingement and flow around a cylinder using RANS and LES models. *Journal of Fluids and Structures*, *Journal Article*. https://doi.org/10.1016/j.jfluidstructs.2014.03.007

Kulyakhtin, A., & Tsarau, A. (2014). A time-dependent model of marine icing with application of computational fluid dynamics. *Cold Regions Science and Technology*, *104–105*, 33–44. https://doi.org/10.1016/j.coldregions.2014.05.001

Lebiedzlnski, K., & Thomas, W. L. (1993). Prediction of bow spray frequency for a naval combatant. *12th International Conference on Port and Ocean Engineering under Arctic Conditions*, 824–834.

Lewis, E. V. (1988). *Principles of naval architecture* (2nd ed.). Society of Naval Architects and Marine Engineers.

Li, Y., Li, D., Bie, S., Wang, Z., Zhang, H., Tang, X., & Zhu, Z. (2018). Numerical simulation for fluid droplet impact on discrete particles with coupled SPH-DEM method. *International Journal of Numerical Methods for Heat & Fluid Flow*, *28*(11), 2581–2605. Earth, Atmospheric & Aquatic Science Collection; Materials Science & Engineering Collection; ProQuest Central; ProQuest One Academic. https://doi.org/10.1108/HFF-11-2017-0464

Lin, Y. C., & Earls, C. J. (2019). Multi-parameter stochastic inversion for first and second moment mass properties of a model-scale ship with topside ice accumulation. *Applied Ocean Research*, *82*, 143–157. https://doi.org/10.1016/j.apor.2018.10.002

Liu, X., Zhong, Z., & Xu, K. (2016). A hybrid solution method for CFD applications on GPU-accelerated hybrid HPC platforms. *Future Generation Computer Systems; Future Generation Computer Systems*, *56*(Journal Article), 759–765. https://doi.org/10.1016/j.future.2015.08.002

Lloyd, A. R. J. M., Salsich, J. O., & Zseleczky, J. J. (1986). *Effect of Bow Shape on Deck Wetness in Head Seas* (EW-17-84). United States Naval Academy.

Lozowski, E. P. (2017). Sea Spray Icing of Ships and Offshore Structures. In *Encyclopedia of Life Support Systems* (p. 31). United Nations Educational Scientific and Cultural Organization (UNESCO).

Lozowski, E. P., Forest, T. W., Chung, V., & Szilder, K. (2002). *Study of Marine Icing: Final Report*. https://doi.org/10.4224/8896262

Lozowski, E. P., Szilder, K., & Makkonen, L. (2000). Computer Simulation of Marine Ice Accretion. *Philosophical Transactions: Mathematical, Physical and Engineering Sciences*, *358*(1776), 2811–2845.

LR. (2015). Provisional Rules for Winterisation of Ships. *Lloyd's Register*, *Journal Article*.

Makkonen, L., Brown, R. D., & Mitten, P. T. (1991). Comments on "Prediction of Vessel Icing for Near-Freezing Sea Temperatures." *Weather and Forecasting*, *6*(4), 565–567. https://doi.org/10.1175/1520-0434(1991)006<0565:COOVIF>2.0.CO;2

Mintu, S. A., Molyneux, D., & Colbourne, B. (2019). Multi-Phase Simulation of Droplet Trajectories of Wave-Impact Sea Spray Over a Vessel. *Proceedings of the ASME 2019 38th International Conference on Ocean, Offshore and Arctic Engineering*, *Volume 2: CFD and FSI*, V002T08A012. https://doi.org/10.1115/OMAE2019-95799

Mintu, S., & Molyneux, D. (2018). Application of GPGPU to Accelerate CFD Simulation. *Proceedings of the ASME 2018 37th International Conference on Ocean, Offshore and Arctic Engineering*, *2*. https://doi.org/10.1115/OMAE2018-77649

Mintu, S., Molyneux, D., & Colbourne, B. (2021). A Theoretical Model for Ship–Wave Impact Generated Sea Spray. *Journal of Offshore Mechanics and Arctic Engineering*, *143*(4). https://doi.org/10.1115/1.4049122

Mokos, A., Rogers, B. D., & Stansby, P. K. (2016). A multi-phase particle shifting algorithm for SPH simulations of violent hydrodynamics with a large number of particles. *Journal of*

*Hydraulic Research*, *Journal Article*, 1–20. https://doi.org/10.1080/00221686.2016.1212944

Mokos, A., Rogers, B. D., Stansby, P. K., & Domínguez, J. M. (2015). Multi-phase SPH modelling of violent hydrodynamics on GPUs. *Computer Physics Communications*, *196*, 304–316. https://doi.org/10.1016/j.cpc.2015.06.020

Monaghan, J. J., Cas, R. A. F., Kos, A. M., & Hallworth, M. (1999). Gravity currents descending a ramp in a stratified tank. *Journal of Fluid Mechanics*, *379*(Journal Article), 39–70. https://doi.org/10.1017/S0022112098003280

Muzik, I., & Kirby, A. (1992). Spray overtopping rates for Tarsiut Island: Model and field study results. *Canadian Journal of Civil Engineering*, *19*(3), 469–477. https://doi.org/10.1139/l92-057

Nielsen, M., & Østerby, O. (2013). A two-continua approach to Eulerian simulation of water spray. *ACM Transactions on Graphics*, *32*(4), 1–10. https://doi.org/10.1145/2461912.2461918

Normore, J. (2010). *Efficient computational fluid dynamics methods for GPGPUs* [Masters thesis]. Memorial University of Newfoundland.

NORSOK. (2007). *NORSOK Standard. N-003, Actions and Action Effects (Edition 2). Journal Article*.

Okamura, M. (1993). Impulsive pressure due to wave impact on an inclined plane wall. *Fluid Dynamics Research*, *12*(4), 215–228. https://doi.org/10.1016/0169-5983(93)90024-5

Osborne, N. (2009). *GPU Fluid Simulation*. School of Computer and Information Science.

Overland, J. (1990). Prediction of Vessel Icing for Near-Freezing Sea Temperatures. *Weather And Forecasting*, *5*(1), 62–77.

Overland, J., Pease, C., Preisendorfer, R., & Comiskey, A. (1986). Prediction of Vessel Icing. *J. Clim. Appl. Meteorol. 25 (12), 1793–1806.*, *Journal Article*.

Owusu, K. P., Kuhn, D. C. S., & Bibeau, E. L. (2013). Capacitive probe for ice detection and accretion rate measurement: Proof of concept. *Renewable Energy*, *50*(Journal Article), 196–205. https://doi.org/10.1016/j.renene.2012.06.003

Panov, V. V. (1976). *Icing of ships (in Russian)*. Arkticheskii i Antarkti- cheskii Nauchno-Issledovatelskii Institut, Gidrometeoizdat, *Trudy 334*, page 263, Leningrad.

Pease, C. H., & Comiskey, A. L. (1985). *Vessel icing in Alaskan waters—1979 to 1984 data set*. Seattle, Wash. : Pacific Marine Environmental Laboratory, U.S. Dept. of Commerce, National Oceanic and Atmospheric Administration, Environmental Research Laboratories.

Pereira, G. G., Cleary, P. W., & Serizawa, Y. (2018). Prediction of fluid flow through and jet formation from a high pressure nozzle using Smoothed Particle Hydrodynamics. *Chemical Engineering Science*, *178*, 12–26. https://doi.org/10.1016/j.ces.2017.12.033

Qu, Q., Zhang, F., Liu, P., & Agarwal, R. (2016). Numerical Simulation of Water Spray Caused by a Rolling Airplane Tire. *Journal of Aircraft*, *53*(1), 182–188.

Raiyan, A., Mclaughlin, T. S., Annavarapu, R. K., & Sojoudi, H. (2018). Effect of superamphiphobic macrotextures on dynamics of viscous liquid droplets. *Scientific Reports*, *8*(1), 15344–15344. https://doi.org/10.1038/s41598-018-33656-9

Rapp, R. J., & Melville, W. K. (1990). Laboratory Measurements of Deep-Water Breaking Waves. *Philosophical Transactions of the Royal Society A: Mathematical, Physical and Engineering Sciences*, *331*(1622), 735–800. https://doi.org/10.1098/rsta.1990.0098

Ren, N., & Marshall, A. W. (2014). Characterizing the initial spray from large Weber number impinging jets. *International Journal of Multiphase Flow*, *58*(Journal Article), 205–213. https://doi.org/10.1016/j.ijmultiphaseflow.2012.08.004

RMRS. (2014). *Rules for the Classification, Construction and Equipment of Mobile Offshore Drilling Units and Fixed Offshore Platforms. ND No. 2-020201- 013-E.*

RMRS. (2016). *Rules for the Classification and Construction of Sea-Going Ships. ND No. 2-020101-087-E.*

Roebber, P., & Mitten, P. (1987). *Modelling and measurement of icing in Canadian waters*. Canadian Climate Centre, Atmospheric Environment Service.

Roselli, R. A. R., Vernengo, G., Brizzolara, S., & Guercio, R. (2019). SPH simulation of periodic wave breaking in the surf zone—A detailed fluid dynamic validation. *Ocean Engineering*, *176*, 20–30. https://doi.org/10.1016/j.oceaneng.2019.02.013

Ryerson, C. C. (1995). Superstructure spray and ice accretion on a large U.S. Coast Guard cutter. *Atmospheric Research*, *36*(3), 321–337. https://doi.org/10.1016/0169-8095(94)00045-F

Ryerson, C. C. (2013). *Icing management for Coast Guard assets* (ERDC/CRREL TR-13-7). U.S. Army Engineer Research and Development Center. http://acwc.sdp.sirsi.net/client/search/asset/1027480

Sampson, R. D., Chung, K. K., & Lozowski, E. P. (1996). A Simple Experiment to Measure the Splash Mass Produced by a Free-Falling Buoyant Sphere Impacting a Deep Quiescent Liquid. *Journal of Colloid and Interface Science*, *181*(2), 673–675. https://doi.org/10.1006/jcis.1996.0428

Samuelsen, E. M., Edvardsen, K., & Graversen, R. G. (2017). Modelled and observed sea-spray icing in Arctic-Norwegian waters. *Cold Regions Science and Technology*, *134*, 54–81. https://doi.org/10.1016/j.coldregions.2016.11.002

Sapone, D. T. (1990). *A Sensitivity Study of Bow Variants on the Distribution of Sea Spray in Regular Head Seas* [Masters thesis]. Massachusetts Institute of Technology.

Sasa, K., Takeuchi, K., Chen, C., Faltinsen, O. M., Prpić-Oršić, J., Valčić, M., Mrakovčić, T., & Herai, N. (2019). Evaluation of speed loss in bulk carriers with actual data from rough sea voyages. *Ocean Engineering*, *187*, 106162. https://doi.org/10.1016/j.oceaneng.2019.106162

Sazhin, S. (2014). *Droplets and Sprays*. Springer London.

Shadloo, M. S., Oger, G., & Le Touzé, D. (2016). Smoothed particle hydrodynamics method for fluid flows, towards industrial applications: Motivations, current state, and challenges. *Computers and Fluids*, *136*(Journal Article), 11–34. https://doi.org/10.1016/j.compfluid.2016.05.029

Shipilova, O., Kulyakhtin, A., Tsarau, A., Libby, B., Moslet, P. O., & Loset, S. (2012, December 3). Mechanism and Dynamics of Marine Ice Accretion on Vessel Archetypes. *Offshore Technology Conference*. https://doi.org/10.4043/23762-MS

Silva, D. F. C., Esperança, P. T. T., & Coutinho, A. L. G. A. (2017). Green water loads on FPSOs exposed to beam and quartering seas, Part II: CFD simulations. *Ocean Engineering*, *140*, 434–452. https://doi.org/10.1016/j.oceaneng.2016.11.008

Sumwalt, R., Weener, E., & Dinh-Zarr, T. B. (2018). *Capsizing and Sinking of Fishing Vessel Destination* (NTSB/MAB-18/14). National Transportation Safety Board Marine Accident Brief.

Szilder, K., & Lozowski, E. P. (1995). A New Method Of Modelling Ice Accretion On Objects Of Complex Geometry. *International Journal of Offshore and Polar Engineering*, *5*(1), 37–42.

Szilder, K., Lozowski, E. P., Forest, T., Reuter, G., & Gagnon, R. (2000). *Modelling of Wet Ice Accretions that Result from Spray*. 15th International Symposium on Ice.

Tabata, T. (1969). Studies of Ice Accumulation on Ships, Part 3. *Low Temp. Sci. (Teion Kagaku), Series A(27)*, 340–349.

Tagliafierro, B., Mancini, S., Ropero-Giralda, P., Domínguez, J. M., Crespo, A. J. C., & Viccione, G. (2021). Performance Assessment of a Planing Hull Using the Smoothed Particle Hydrodynamics Method. *Journal of Marine Science and Engineering*, *9*(3). https://doi.org/10.3390/jmse9030244

Tezdogan, T., Incecik, A., & Turan, O. (2016). Full-scale unsteady RANS simulations of vertical ship motions in shallow water. *Ocean Engineering*, *123*, 131–145. https://doi.org/10.1016/j.oceaneng.2016.06.047

Thomas, W. L. (1991). *Bering Sea Topside Icing Probabilities for Two Naval Combatants* (DTRC/SHD-1212-06). David Taylor Research Center. https://apps.dtic.mil/dtic/tr/fulltext/u2/a246601.pdf

Troitskaya, Y., Kandaurov, A., Ermakova, O., Kozlov, D., Sergeev, D., & Zilitinkevich, S. (2017). Bag-breakup fragmentation as the dominant mechanism of sea-spray production in high winds. *Scientific Reports*, *7*(1). https://doi.org/10.1038/s41598-017-01673-9

Vacondio, R., Rogers, B. D., Stansby, P. K., & Mignosa, P. (2016). Variable resolution for SPH in three dimensions: Towards optimal splitting and coalescing for dynamic additivity. *Computer Methods in Applied Mechanics and Engineering*, *300*, 442–460. https://doi.org/10.1016/j.cma.2015.11.021

Vacondio, R., Rogers, B. D., Stansby, P. K., Mignosa, P., & Feldman, J. (2013). Variable resolution for SPH: A dynamic particle coalescing and splitting scheme. *Computer Methods in Applied Mechanics and Engineering*, *256*, 132–148. https://doi.org/10.1016/j.cma.2012.12.014

Varlas, G., Marinou, E., Gialitaki, A., Siomos, N., Tsarpalis, K., Kalivitis, N., Solomos, S., Tsekeri, A., Spyrou, C., Tsichla, M., Kampouri, A., Vervatis, V., Giannakaki, E., Amiridis, V., Mihalopoulos, N., Papadopoulos, A., & Katsafados, P. (2021). Assessing Sea-State Effects on Sea-Salt Aerosol Modeling in the Lower Atmosphere Using Lidar and In-Situ Measurements. *Remote Sensing (Basel, Switzerland)*, *13*(4), 614. https://doi.org/10.3390/rs13040614

Veron, F. (2015). Ocean Spray. *Annual Review of Fluid Mechanics; Annu.Rev.Fluid Mech.*, *47*(1), 507–538. https://doi.org/10.1146/annurev-fluid-010814-014651

Veron, F., Hopkins, C., Harrison, E. L., & Mueller, J. A. (2012). Sea spray spume droplet production in high wind speeds. *Geophysical Research Letters*, *39*(16), n/a-n/a. https://doi.org/10.1029/2012GL052603

Vivekanandan, J., Ghate, V. P., Jensen, J. B., Ellis, S. M., & Schwartz, M. C. (2020). A Technique for Estimating Liquid Droplet Diameter and Liquid Water Content in Stratocumulus Clouds Using Radar and Lidar Measurements. *Journal of Atmospheric and Oceanic Technology*, *37*(11), 1–60. https://doi.org/10.1175/JTECH-D-19-0092.1

Wang, Z., Yang, J., & Stern, F. (2016). *High-fidelity simulations of bubble, droplet and spray formation in breaking waves*. *792*(Journal Article), 307–327. https://doi.org/10.1017/jfm.2016.87

Wang, Z.-B., Chen, R., Wang, H., Liao, Q., Zhu, X., & Li, S.-Z. (2016). An overview of smoothed particle hydrodynamics for simulating multiphase flow. *Applied Mathematical Modelling*, *Journal Article*. https://doi.org/10.1016/j.apm.2016.06.030

Watanabe, Y., & Ingram, D. M. (2015). Transverse instabilities of ascending planar jets formed by wave impacts on vertical walls. *Proceedings of the Royal Society A: Mathematical, Physical and Engineering Sciences*, *471*(2182). https://doi.org/10.1098/rspa.2015.0397

Watanabe, Y., & Ingram, D. M. (2016). Size distributions of sprays produced by violent wave impacts on vertical sea walls. *Proceedings of the Royal Society A: Mathematical, Physical and Engineering Sciences*, *472*(2194). https://doi.org/10.1098/rspa.2016.0423

Xiang, Y., Yu, B., Yuan, Q., & Sun, D. (2017). GPU Acceleration of CFD Algorithm: HSMAC and SIMPLE. *Procedia Computer Science; Procedia Computer Science*, *108*(Journal Article), 1982–1989. https://doi.org/10.1016/j.procs.2017.05.124

Yang, L., Fu, Q., Qu, Y., Gu, B., & Zhang, M. (2012). Breakup of a power-law liquid sheet formed by an impinging jet injector. *International Journal of Multiphase Flow*, *39*, 37–44. https://doi.org/10.1016/j.ijmultiphaseflow.2011.11.003

Yang, Q., & Qiu, W. (2012). Numerical simulation of water impact for 2D and 3D bodies. *Ocean Engineering*, *43*(Journal Article), 82–89. https://doi.org/10.1016/j.oceaneng.2012.01.008

Zakrzewski, W. P. (1986a). *Icing of Fishing Vessels. Part I: Splashing a Ship with Spray* (pp. 179–194). NOAA Technical Memorandum ERL PMEL-66.

https://www.scopus.com/inward/record.uri?eid=2-s2.0-0022943447&partnerID=40&md5=15f69109dadc88b9c343792f3066765a

Zakrzewski, W. P. (1986b). Splashing a ship with collision-generated spray. *Cold Regions Science and Technology*, *14*(1), 65–83. https://doi.org/10.1016/0165-232X(87)90045-0

Zakrzewski, W. P. (1989a). *Soviet Marine Icing Data*. Canadian Climate Centre, Atmospheric Environment Service.

Zakrzewski, W. P. (1989b). The use of ship icing models for forecasting icing rates on sea-going ships. *Proceedings of the 10th International Conference on Port and Ocean Engineering Under Arctic Conditions*, 1454–1467.

Zakrzewski, W. P., Lozowski, E. P., & Muggeridge, D. (1988). Estimating the extent of the spraying zone on a sea-going ship. *Ocean Engineering*, *15*(5), 413–429. https://doi.org/10.1016/0029-8018(88)90008-X

Zha, R., Peng, H., & Qiu, W. (2021). An improved higher-order moving particle semi-implicit method for simulations of two-dimensional hydroelastic slamming. *Physics of Fluids (1994)*, *33*(3), 37104. https://doi.org/10.1063/5.0033491

Zhao, H., Xu, J.-L., Wu, J.-H., Li, W.-F., & Liu, H.-F. (2015). Breakup morphology of annular liquid sheet with an inner round air stream. *Chemical Engineering Science*, *137*, 412–422. https://doi.org/10.1016/j.ces.2015.06.062

Zhao, K., Liu, P., Qu, Q., Ma, P., & Hu, T. (2018). Flow physics and chine control of the water spray generated by an aircraft rigid tire rolling on contaminated runways. *Aerospace Science and Technology*, *72*, 49–62. https://doi.org/10.1016/j.ast.2017.10.036

Zhuang, Y., Lozowski, E. P., Wilson, J. D., & Bird, G. (1993). Sea spray dispersion over the ocean surface: A numerical simulation. *Journal of Geophysical Research: Oceans*, *98*(C9), 16547–16553. https://doi.org/10.1029/93JC01406

# Appendices

# Appendix A: Lines Plan of MFV Narva

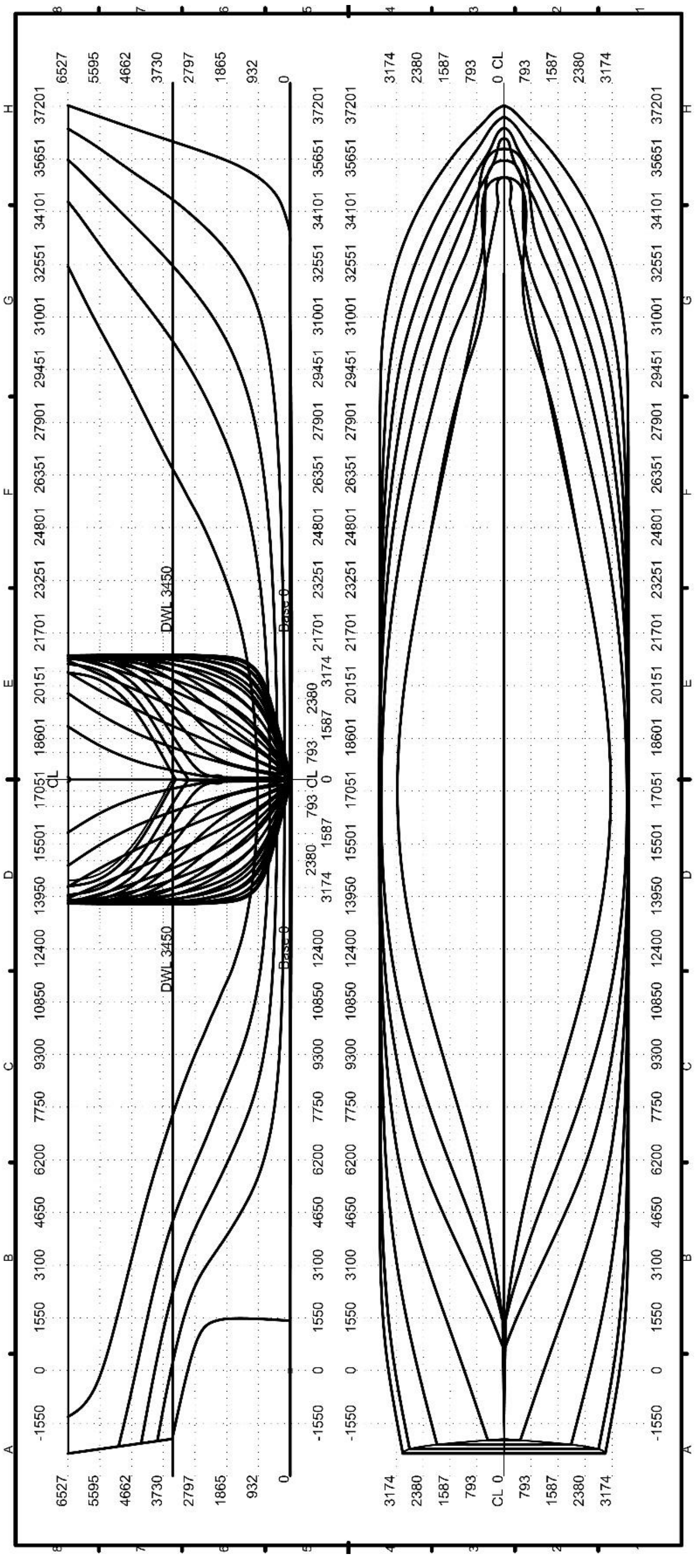

**FIGURE 0-1: LINES PLAN OF RE-CREATED MFV NARVA**

# Appendix B: Python Code for Spray Properties

Appendix C: DualSPHysics Code